Pushing the Precision in B Physics

Dissertation

zur Erlangung des akademischen Grades eines Doktors
der Naturwissenschaften

vorgelegt von

M.Sc. Kevin Olschewsky

eingereicht bei der Naturwissenschaftlich-Technischen Fakultät
der Universität Siegen

Siegen
Juni 2022

Betreuer und erster Gutachter

Prof. Dr. Thomas Mannel

Universität Siegen

Zweiter Gutachter

Prof. Dr. Alexander Lenz

Universität Siegen

Weitere Mitglieder der Promotionskommission

Prof. Dr. Florian Bernlochner

Rheinische Friedrichs-Wilhelms-Universität Bonn

und

Prof. Dr. Otfried Gühne

Universität Siegen

Tag der mündlichen Prüfung

22. September 2022

Abstract

Semi– and non–leptonic decays of B mesons offer a powerful probe for the flavour sector in the Standard Model (SM). With ever increasing amounts of experimental data from particle colliders, the need for more precise, but also more utilizable and reliable theoretical predictions is growing. In this work, we study the inclusive semileptonic decays $B \to X_c \ell \bar{\nu}$ and $B \to X_u \ell \bar{\nu}$ and extract the CKM elements V_{cb} and V_{ub} from them, respectively. In addition, we investigate the extent of CP violation in the non–leptonic decay $B \to \pi\pi\pi$. The description of these three decays is complicated due to the appearance of short– and long–distance effects in the strong interactions. In order to disentangle the pieces that can be determined from a perturbative expansion and the genuinely non–perturbative ones, we make use of an Operator Product Expansion. We collect all state–of–the–art corrections to the expressions and summarize them into open–source software packages.

For the decay $B \to X_c \ell \bar{\nu}$, we exploit the Reparameterization Invariance (RPI) of the Heavy Quark Effective Theory to reduce the number of non–perturbative matrix elements. Subsequently we use the recently measured moments of the lepton invariant mass to extract a new value for V_{cb} up to $\mathcal{O}(1/m_b^4)$ in the Heavy Quark Expansion.

In the decay $B \to X_u \ell \bar{\nu}$ it is necessary to subtract the unwanted background of the decay into a charmonium final state. This restriction causes the appearance of non–local shape functions, which have to be modelled. We include all available information about the leading and subleading shape functions and determine a cluster of models to find a reasonable estimate for the model uncertainty. Furthermore we include all perturbative corrections up to α_s^2 to finally calculate partial rates with various kinematical cuts and extract V_{ub} from them.

Unlike the aforementioned semileptonic decays, the non–leptonic decay $B \to \pi\pi\pi$ shows pronounced features in the CP landscape that are difficult to explain with theoretical methods. In recent amplitude analyses, only resonance contributions were included to dynamically generate the strong phase. We suggest a new parameterization of charm–loop effects, which can cause intricate structures in the CP landscape, while at the same time being easy to implement in current analyses. We discuss the implications of this approach and how the underlying physics can be made more visible by changing to a suitable set of physical operators in the analysis.

Zusammenfassung

Semi– und nicht–leptonische Zerfälle von B–Mesonen stellen eine wirkungsvolle Möglichkeit dar, den Flavour-Sektor des Standardmodells (SM) zu erforschen. Mit der zunehmenden Menge an experimentellen Daten wächst der Bedarf an präziseren, aber auch besser nutzbaren theoretischen Vorhersagen. In dieser Arbeit untersuchen wir die inklusiven semileptonischen Zerfälle $B \to X_c \ell \bar{\nu}$ und $B \to X_u \ell \bar{\nu}$ und extrahieren daraus die CKM-Elemente V_{cb} und V_{ub}. Darüber hinaus untersuchen wir die CP-Verletzung im nicht-leptonischen Zerfall $B \to \pi\pi\pi$. Die Beschreibung dieser drei Zerfälle ist aufgrund des Auftretens von starken Wechselwirkungen, die sich über physikalische Effekte kurzer wie langer Skalen erstrecken, sehr anspruchsvoll. Um die Anteile, die sich mit einer Störungsreihe berechnen lassen, von den anderen zu trennen, verwenden wir eine Operator Produkt Entwicklung. Hierfür nutzen wir alle nach dem Forschungsstand bekannten Korrekturen und fassen sie in Open–Source Softwarepaketen zusammen.

Für den Zerfall $B \to X_c \ell \bar{\nu}$ nutzen wir die Reparametrisierungsinvarianz (RPI) der effektiven Theorie für schwere Quarks, um die Anzahl der nicht–perturbativen Matrixelemente zu reduzieren. Anschließend verwenden wir die kürzlich gemessenen Momente der invarianten Leptonenmasse, um einen neuen Wert für V_{cb} zu bestimmen.

Bei dem Zerfall $B \to X_u \ell \bar{\nu}$ ist es experimentell notwendig den Charm Hintergrund zu reduzieren. Diese Einschränkung führt zum Auftreten von modellierten, nicht–lokalen Shape Funktionen. Wir beziehen alle verfügbaren Informationen über die Shape Funktionen ein und bestimmen anschlißend eine Gruppe von Modellen für eine sinnvolle Abschätzung der Modellunsicherheit. Weiterhin berücksichtigen wir alle Störungskorrekturen bis α_s^2, um schließlich partielle Raten mit verschiedenen Phasenraumschnitten zu berechnen und V_{ub} daraus zu extrahieren.

Im Gegensatz zu den vorher erwähnten semileptonischen Zerfällen, zeigt der nicht–leptonische Zerfall $B \to \pi\pi\pi$ ausgeprägte Strukturen in der CP–Landschaft, die mit theoretischen Methoden schwer zu erklären sind. In Amplitudenanalysen wurden bisher nur Resonanzbeiträge zur dynamischen Erzeugung der starken Phase genutzt. Wir schlagen eine neue, einfach zu implementierende Parametrisierung von Charm–Loop Effekten vor, die starke Strukturen in der CP-Landschaft hervorrufen kann. Wir diskutieren die Auswirkungen dieses Ansatzes und wie die zugrundeliegende Physik durch die Wahl geeigneter physikalischer Operatoren deutlicher dargestellt werden kann.

Contents

Introduction

The investigation of natural phenomena with empirical methods constitutes the core of natural sciences since the 17^{th} century. In physics it has led to the emergence of numerous successful theories, which cast the results of observations into a mathematical description. One of the questions that was always sought–after, is what the constituents of matter are and how they interact. This research has led to the development of the Standard Model of Particle Physics (SM) [1, 2, 3], which is currently the most precise and experimentally tested scientific theory. It describes the interactions of all known particles and forces at the fundamental level with the exception of gravity.

Apart from its obvious success, there are still several phenomena that cannot be explained in the SM. Most notable is the abundance of any explanation for the experimentally well verified dark matter and dark energy [4, 5] as well as the so called baryon asymmetry [6]. The former refers to the existence of an additional form of matter that is potentially of a completely different nature than the matter in the SM. Baryon asymmetry is the observed imbalance of baryonic and anti–baryonic matter in the universe. According to the Sakharov conditions [7] the underlying theory must allow for baryon number violations, out–of–equilibrium reactions and especially C and CP violation to produce matter and antimatter at different rates. In particular the latter condition is tied to low–energy reactions and the flavour sector of the SM, that we investigate in this thesis.

Generally speaking, effects beyond the SM, sometimes called "New Physics", can be searched for in two ways – directly and indirectly. Direct searches are performed in experiments at large particle colliders, where new forms of matter hopefully show up at highest energies. However, up till today, there were no significant hints at phenomena that deviate substantially from the SM. Indirect searches, on the other hand, look for tiny deflections from the SM caused by new physics. Needless to say, the precision

necessary to render such effects visible must be outstanding – both experimentally and theoretically. In particular, it is inevitable for the indirect approach that both sides work together hand in hand, i.e. theoretical predictions at the highest possible precision need to be provided to the experimental collaborations in a suitable and usable form.

The precision necessary for the aforementioned endeavour is reflected in particular in the determination of the fundamental parameters of the SM. In this respect the flavour sector is quite challenging, because it contains a number of parameters that relate quarks of different flavour. The part of the SM that describes the dynamics of quarks and gluons is Quantum Chromodynamics (QCD). Due to its non–abelian nature, the gluons, which are the gauge bosons of the strong force, may interact with each other causing the theory to be asymptotically free [8]. At high energies quarks thus interact weakly, while at low energies the coupling becomes strong leading to the confinement of quarks and gluons in composite hadrons. With the strong coupling becoming large at low energies, theoretical predictions cannot be obtained as perturbative expansions anymore. This non–perturbative behaviour has led to the development of various techniques to render calculations possible. Most notably we use so–called Effective Field Theories (EFTs) in this thesis, which are Quantum Field Theories, designed to describe particle interactions at the appropriate energy scale.

A prime example that combines the above aspects, i.e. a relation to fundamental parameters, a connection to the phenomenon of CP violation (and thereby baryon asymmetry) and low–energy scales, is the B meson. It provides the simplest bound state of a heavy and light quark/anti–quark pair and has, due to its relatively large mass, a variety of intriguing decay channels at its disposal. Of particular interest are flavour–changing semi– and non–leptonic decays. They are related to the universal Cabibbo–Kobayashi–Maskawa–matrix (CKM) elements [9, 10], which pose the major factor of precision in several CP violating decays in the SM. Notably the B meson factories like Belle (II), BaBar and LHCb have provided extraordinarily amounts of precise data for B decays in the last decade. Hence, the extraction of fundamental parameters from that data with ever–increasing theoretical predictions, is a vital aspect of investigations in particle physics.

In the present work, we want to contribute a significant step towards meeting this challenge. On the one hand, we focus on the determination of the CKM factors V_{cb} and V_{ub} from the inclusive semileptonic decays $B \to X_c \ell \bar{\nu}$ and $B \to X_u \ell \bar{\nu}$, respectively. On the other hand we investigate the exclusive decay $B \to \pi\pi\pi$ that shows remarkably strong features in its CP landscape, which are difficult to explain with the techniques

usually applied to non–leptonic decays.

Apart from the obvious connection to the B meson and its relation to fundamental parameters, those three studies are related in how they offer a bridge to the experimental analysis. Often particularly precise (and hence complicated) theory predictions are not made accessible to the experimental collaborations in a utilizable manner. In turn, the analyses are conducted with models that are simpler; especially simpler to implement. Therefore we deploy, together with this thesis, two open–source software packages for both inclusive processes, which contain all state–of–the–art corrections in them [11, 12]. In addition, for the exclusive decay, we develop an extension for the current analyses, that can immediately be incorporated into existing models [13].

We structure this thesis as follows. We start with a short introduction into the SM, where we focus on the flavour sector and CP violation in particular. It follows a short presentation of the general techniques used in Effective Field Theories. In particular, we give short introductions in the Weak Effective and Heavy Quark Effective Theory, as they are the basis for many of the following calculations. In the next chapter we lay the theoretical foundation for the study of inclusive semileptonic decays of B mesons. We distinguish between final states containing charm– and up quarks and show how this affects the structure of the Operator Product Expansion. In this, we discuss the different perturbative and non–perturbative pieces of the calculations and how they can be disentangled. Furthermore we introduce the concept of mass schemes and discuss in particular how the kinetic scheme can be used to improve the precision for physical observables.

The second part of the thesis is in general separated in three parts. The first concentrates on the non–leptonic three body decay $B \to \pi\pi\pi$ [13]. We suggest a new parameterization of charm–loop effects and demonstrate how it can easily be implemented in current amplitude analyses. In addition we use this ansatz to generate elaborate structures in the CP landscape, which show a significant resemblance with recent experimental findings [14, 15, 16].

The next chapter is dedicated to the determination of $|V_{cb}|$ with q^2 moments from newly obtained data by Belle [17] and especially Belle II [18]. We use the Reparameterization Invariance of the Heavy Quark Effective Theory to lessen the number of non–perturbative matrix elements and attempt a determination of $|V_{cb}|$, including all terms up to $1/m_b^4$. To that end we perform a distinguished fit to the experimental data and discuss in detail all inputs and uncertainties. Finally we present a new value for $|V_{cb}|$ obtained with this method [19].

In the last chapter we draw our attention to the determination of partial decay rates in the semileptonic process $B \to X_u \ell \nu$. We make use of a factorization theorem [20, 21], which uses the Soft Collinear Effective Theory to disentangle contributions at different energy scales. The kinematical region of interest inherits a different power counting than the full phase space, which in turn introduces non–local matrix elements; the so–called shape functions. We gather all available information on these shape functions and subsequently derive a model ansatz. In addition we discuss the several sources of power corrections, generate models for the subleading shape functions, which are the dominant corrections to the leading power and collect all inputs in a software package [12], which we then use to determine partial decay rates for various kinematical cuts. We give a detailed overview over the different sources of theoretical uncertainties and, as an outlook, we use these rates as an input to extract $|V_{ub}|$.

Chapter 1

Foundations

The standard model of particle physics (SM) is one the most successful scientific theory up to date. It produces remarkably accurate results and has been tested in a plethora of different experiments. A full review of all its properties and peculiarities goes beyond the scope of this thesis; for comprehensive overviews see for example [22, 23, 24]. In the course of this chapter a number of concepts and methods will be introduced that are important throughout this work. Special emphasis is put on the foundations of flavour physics and CP violation.

1.1 The Standard Model

The standard model is a renormalizable Quantum Field Theory. It is invariant under local gauge transformations of the symmetry group

$$SU(3)_C \otimes SU(2)_L \otimes U(1)_Y \,, \tag{1.1}$$

with $SU(3)_C$ being the gauge group of the strong interactions with colour charge, $SU(2)_L$ the group of electroweak interactions with charge T_3 and $U(1)_Y$ the group of electromagnetic interactions with hypercharge Y. Since every group $SU(N)$ has N^2-1 generators, there are eight gauge bosons in $SU(3)_C$, the gluons $g^1_\mu, \ldots, g^8_\mu$, a triplett of gauge bosons in $SU(2)_L$, $W^1_\mu, W^2_\mu, W^3_\mu$ and a single boson in $U(1)_Y$, the field B_μ. By

acquiring a vacuum expectation value (VEV)

$$\langle H \rangle = \frac{1}{\sqrt{2}} \begin{pmatrix} 0 \\ v \end{pmatrix} , \tag{1.2}$$

the Higgs field H and its potential

$$V(H) = \mu^2 H^\dagger H + \frac{1}{2}\lambda |H H^\dagger|^2 \tag{1.3}$$

spontaneously break the electroweak symmetry of the gauge group to

$$SU(2)_L \otimes U(1)_Y \to U(1)_Q \, , \tag{1.4}$$

with the electric charge Q related to the hypercharge and the third component of the weak isospin via $Y = 2(Q + T_3)$.

After the symmetry breaking there are three massive gauge bosons in the electroweak sector: two charged $W^\pm_\mu$ and one uncharged Z^0_μ together with one uncharged massless photon A_μ in the electromagnetic sector. The SM also contains six types (flavours) of quarks: up (u), down (d), strange (s), charm (c), bottom (b) and top (t) and an additional six types of leptons: electron (e), muon (μ), tauon (τ) with three corresponding neutrinos (ν_e, ν_μ, ν_τ). Each particle of the SM falls into a specific representation of the gauge group; see table 1.1. Also note that right–handed neutrinos are commonly not included in the SM, but can be added in an extension [25].

The most general Lagrangian that can be constructed under the aforementioned assumptions and the symmetry group eq.(1.1) is [1]

$$\begin{aligned} \mathcal{L}_{\text{SM}} =& \bar{\psi} i \not{D} \psi - \frac{1}{4} \left(G^b_{\mu\nu} G^{\mu\nu}_b + W^a_{\mu\nu} W^{\mu\nu}_a + B_{\mu\nu} B^{\mu\nu} \right) \\ &+ (D^\mu H)^* (D_\mu H) - V(H) - (\bar{\psi}_L \hat{Y} H \psi_R + \text{h.c.}) \, , \end{aligned} \tag{1.5}$$

where ψ are all fermion fields and $G^b_{\mu\nu}$, $W^a_{\mu\nu}$ and $B_{\mu\nu}$ are the field strength tensors of the three different gauge groups respectively. They are defined by

$$B_{\mu\nu} = \partial_\mu B_\nu - \partial_\nu B_\mu \, , \tag{1.6}$$

$$W^a_{\mu\nu} = \partial_\mu W^a_\nu - \partial_\nu W^a_\mu - i g_2 \varepsilon^{abc} W^b_\mu W^c_\nu \, , \tag{1.7}$$

$$G^b_{\mu\nu} = \partial_\mu G^b_\nu - \partial_\nu G^b_\mu - i g_s f^{bac} G^a_\mu G^c_\nu \, , \tag{1.8}$$

[1] We omit ghost terms and gauge fixing terms here, as they will not play a role in this thesis.

Field	Generations	Representation
B_μ	-	$(\mathbf{1}, \mathbf{1}, 0)$
W_μ^a	-	$(\mathbf{1}, \mathbf{3}, 0)$
g_μ^a	-	$(\mathbf{8}, \mathbf{1}, 0)$
Q_L^i	$\begin{pmatrix} u_L \\ d_L \end{pmatrix}, \begin{pmatrix} c_L \\ s_L \end{pmatrix}, \begin{pmatrix} t_L \\ b_L \end{pmatrix}$	$(\mathbf{3}, \mathbf{2}, 1/3)$
E_L^i	$\begin{pmatrix} \nu_{e,L} \\ e_L \end{pmatrix}, \begin{pmatrix} \nu_{\mu,L} \\ \mu_L \end{pmatrix}, \begin{pmatrix} \nu_{\tau,L} \\ \tau_L \end{pmatrix}$	$(\mathbf{1}, \mathbf{2}, -1)$
u_R^i	(u_R, c_R, t_R)	$(\mathbf{3}, \mathbf{1}, 4/3)$
d_R^i	(d_R, s_R, b_R)	$(\mathbf{3}, \mathbf{1}, -2/3)$
e_R^i	(e_R, μ_R, τ_R)	$(\mathbf{1}, \mathbf{1}, -2)$
H	-	$(\mathbf{1}, \mathbf{2}, 1)$

Table 1.1: Representation of the SM fields under $SU(3)_C, SU(2)_L, U(1)_Y$. The upper section contains the gauge boson fields, the middle section the matter content and the lower row the Higgs field. The second column represents the different generations of the fields if existent. It is worthwhile to note that the SM distinguishes between left and right handed fields by means of the electroweak sector.

with the structure constant ε^{abc} of $SU(2)$ and f^{bac} of $SU(3)$. Furthermore the covariant derivative D_μ reads

$$D_\mu = \partial_\mu - ig_1 Y B_\mu - ig_2 \frac{\sigma^a}{2} W_\mu^a - ig_s \frac{\lambda^b}{2} G_\mu^b \,, \tag{1.9}$$

in which σ^a are the Pauli matrices and λ^a the Gell–Mann matrices – both are the generators of their respective symmetry group in the fundamental representation. In addition the three quantities g_1, g_2 and g_s are the couplings of $U(1)_Y$, $SU(2)_L$ and $SU(3)_C$ respectively. They are related to the electric charge via

$$e = \frac{g_1 g_2}{\sqrt{g_1^2 + g_2^2}} \,, \tag{1.10}$$

and in addition it is also useful to define the strong and electromagnetic coupling constant by

$$\alpha_e \coloneqq \frac{e^2}{4\pi} \qquad \alpha_s \coloneqq \frac{g_s^2}{4\pi} \,. \tag{1.11}$$

1.2 Flavour sector and the CKM matrix

The Lagrangian in eq.(1.5) is expressed in the interaction basis in which gauge bosons do not mix quarks of different flavours. Quarks are, however, defined as mass eigenstates and thus we switch to a basis in which the fermion masses are diagonal; the so called mass basis. Disregarding the lepton sector, we decompose the components of the $SU(2)_L$ quark doublet $Q_L^i = (u_L^i, d_L^i)^{\mathrm{T}}$ in the Yukawa sector of the Lagrangian [2]

$$\mathcal{L}_{Yk} \supset (M_d)_{ij}\, \bar{d}_L^i d_R^j + (M_u)_{ij}\, \bar{u}_L^i u_R^j + \text{h.c.}, \qquad M_q \coloneqq \frac{v}{\sqrt{2}} Y_q. \tag{1.12}$$

The mass matrices M_q defined in the above expression can always be diagonalized by means of a biunitary transformation on the quark fields

$$q_L^i = (V_{qL})^{ij}\, q_L^j, \qquad q_R^i = (V_{qR})^{ij}\, q_R^j\,, \tag{1.13}$$

such that the mass matrix can be written as

$$M_q^{\text{diag}} = V_{qL} M_q V_{qR}^{\dagger}\,. \tag{1.14}$$

The diagonalization of the mass matrix in turn changes the interactions of the $W_\mu^\pm$ with the quark fields. They get the slightly more complicated form

$$\mathcal{L}_{Yk} \supset \frac{g_2}{2\sqrt{2}} \bar{u}_L^i (V_{uL} V_{dL}^{\dagger})_{ij} \gamma^\mu (1-\gamma_5) d_L^j W_\mu^+ + \text{h.c.}\,, \tag{1.15}$$

which defines the so called Cabibbo–Kobayashi–Maskawa (CKM) matrix via

$$V_{\text{CKM}} \coloneqq (V_{uL} V_{dL}^{\dagger}) = \begin{pmatrix} V_{ud} & V_{us} & V_{ub} \\ V_{cd} & V_{cs} & V_{cb} \\ V_{td} & V_{ts} & V_{tb} \end{pmatrix}. \tag{1.16}$$

This unitary, complex–valued matrix is non–diagonal and therefore mixes quark eigenstates of different flavour. It provides the only source of flavour–changing currents in the SM, as the neutral currents are unaffected by the mixing at tree level. In addition it can be shown that the CKM matrix has only four free parameters: three real angles and one complex phase. This fact can be made manifest by choosing an explicit parameterization. The standard parameterization used by the Particle Data Group

[2] For this chapter it is assumed that $q = u, d$.

(PDG) reads for example [26]

$$V_{\text{CKM}} = \begin{pmatrix} c_{12}c_{13} & s_{12}c_{13} & s_{13}e^{-i\delta} \\ -s_{12}c_{23} - c_{12}s_{23}s_{13}e^{i\delta} & c_{12}c_{23} - s_{12}s_{23}s_{13}e^{i\delta} & s_{23}c_{13} \\ s_{12}s_{23} - c_{12}c_{23}s_{13}e^{i\delta} & -c_{12}s_{23} - s_{12}c_{23}s_{13}e^{i\delta} & c_{23}c_{13} \end{pmatrix}, \tag{1.17}$$

where the $c_{ij} \coloneqq \cos(\theta_{ij})$ and $s_{ij} \coloneqq \sin(\theta_{ij})$ are the real parameters and δ is the complex phase. In order to unveil the relative sizes of the different flavour transitions, the so called Wolfenstein parameterization is convenient [27]. It parameterizes the free parameters in (λ, A, ρ, η) and then expands in the small parameter $\lambda = |V_{us}|$. Up to $\mathcal{O}(\lambda^3)$ it reads [27]

$$V_{\text{CKM}} = \begin{pmatrix} 1 - \frac{1}{2}\lambda^2 & \lambda & A\lambda^3(\rho - i\eta) \\ -\lambda & 1 - \frac{1}{2}\lambda^2 & A\lambda^2 \\ A\lambda^3(1 - \rho - i\eta) & -A\lambda^2 & 1 \end{pmatrix} + \mathcal{O}(\lambda^4)\,, \tag{1.18}$$

where all parameters have been experimentally determined and read approximately [28]

$$\lambda \simeq 0.23, \qquad A \simeq 0.8, \qquad \rho \simeq 0.1, \qquad \eta \simeq 0.3\,. \tag{1.19}$$

Notice that the diagonal elements of the CKM–matrix are almost unity, which shows that the SM clearly favours the transition within one family over a flavour changing process. The fact that the CKM–matrix is unitary by construction implies that several elements can be related amongst each other; specifically there are six relations of the form

$$\sum_i V_{ij} V_{ik}^* = \delta_{jk}\,, \tag{1.20}$$

and in particular we find

$$V_{ud}V_{ub}^* + V_{cd}V_{cb}^* + V_{td}V_{tb}^* = 0\,. \tag{1.21}$$

Especially for this thesis, eq.(1.21) is important as it contains two CKM–elements that will be investigated in much detail later on, namely V_{cb} in chapter 5 and V_{ub} in chapter 6.

The graphical depiction in the complex plane of eq.(1.21) is known as the unitarity triangle; see figure 1.1. It is usually rescaled by $V_{cd}V_{cb}^*$ and depicted in the $(\bar{\rho}, \bar{\eta})$-plane,

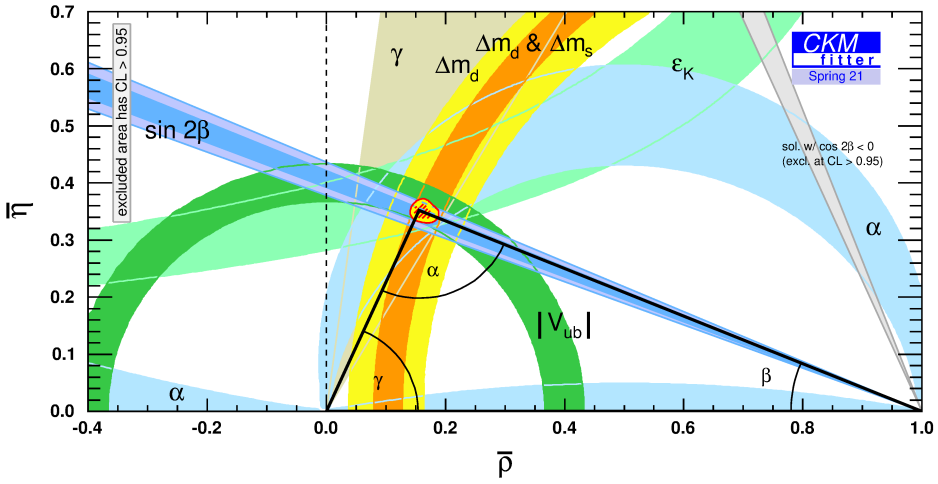

Figure 1.1: The unitarity triangle in the $\bar{\rho}$-$\bar{\eta}$ plane with several experimental constraints on the CKM–elements. The red hashed region corresponds to 68 % confidence level of the global combination obtained by the CKMfitter group [28].

where

$$\bar{\rho} = \rho\left(1 - \frac{\lambda^2}{2}\right), \qquad \bar{\eta} = \eta\left(1 - \frac{\lambda^2}{2}\right). \tag{1.22}$$

Furthermore in terms of the CKM–elements the lengths of the triangles sides read

$$R_u := \left|\frac{V_{ud}V_{ub}^*}{V_{cd}V_{cb}^*}\right|, \qquad R_t := \left|\frac{V_{td}V_{tb}^*}{V_{cd}V_{cb}^*}\right| \tag{1.23}$$

and the angles are

$$\alpha := \arg\left[-\frac{V_{td}V_{tb}^*}{V_{ud}V_{ub}^*}\right], \qquad \beta := \arg\left[-\frac{V_{cd}V_{cb}^*}{V_{td}V_{tb}^*}\right], \qquad \gamma := \arg\left[-\frac{V_{ud}V_{ub}^*}{V_{cd}V_{cb}^*}\right]. \tag{1.24}$$

1.3 CP violation

The existence of flavour in the SM and especially the complex phase in the CKM–matrix are closely related to the occurrence of CP violation in nature. The CP–symmetry corresponds to the subsequent application of the charge conjugation (C) and the parity transformation (P) to a given process and relates particles with their antiparticles. Violation of this symmetry hence resembles the fact that a given decay

process must not have the same rate as the decay of the corresponding antiparticle

$$\Gamma(A \to B) \neq \Gamma(\bar{A} \to \bar{B})\,. \tag{1.25}$$

This can only arise however in interference between two different decay amplitudes $\mathcal{A}_i$, which must carry different weak and strong phases, γ_i and δ_i, respectively.

As discussed before, the SM with three generations provides a source for the weak phase in the couplings of the $W^{\pm}$ bosons. It changes sign under CP transformations and is therefore called CP–odd. The strong phases arise due to possible rescattering effects of intermediate on–shell states during the decay process. They are CP–even, since strong interactions conserve CP.

Parameterizing a decay amplitude $\mathcal{A}$ with its phases explicitly reads

$$\mathcal{A}(B \to f) = \mathrm{e}^{i\gamma_1}|A_1|\mathrm{e}^{i\delta_1} + \mathrm{e}^{i\gamma_2}|A_2|\mathrm{e}^{i\delta_2}\,, \tag{1.26}$$

which is always possible due to the unitarity relations in eq.(1.21). Direct CP violation is probed via the parameter a_{CP}, which is defined by the amplitude and its CP conjugate

$$a_{\mathrm{CP}} \coloneqq \frac{|\mathcal{A}(B \to f)|^2 - |\mathcal{A}(\bar{B} \to \bar{f})|^2}{|\mathcal{A}(B \to f)|^2 + |\mathcal{A}(\bar{B} \to \bar{f})|^2} = \frac{2|A_1||A_2|\sin\Delta\delta\sin\Delta\gamma}{|A_1|^2 + |A_2|^2 + 2|A_1||A_2|\cos\Delta\delta\cos\Delta\gamma}\,, \tag{1.27}$$

where the second equality explicitly utilizes the parameterization in eq.(1.26) and $\Delta\delta$ and $\Delta\gamma$ are the differences in the strong and weak phases, respectively. This expression shows that direct CP violation requires at least two amplitudes and a non–trivial difference in the CP–even and odd phase. Moreover the size of the CP violation depends crucially on the sizes of the respective decay amplitudes. If for example $|A_1| \gg |A_2|$ we expect the violation to be very small (which in turn might also impede the measurement) even if the phase differences were large.

Chapter 2

Effective Field Theories

In order to exactly determine where the SM deviates from experimental measurements it becomes ever more necessary to have precise theoretical predictions. Unfortunately the particular structure of the gauge group $SU(3)_C$ causes the strong coupling α_s to become very large at low energies – an energy regime particularly interesting for phenomenological investigations in the flavour sector of the SM. This causes QCD, which is the underlying theory describing the dynamics of quarks and gluons, to contain non–perturbative pieces that cannot be determined with the usual methods of perturbative expansions.

There is however a way to resolve this remedy, namely Effective Field Theories (EFTs). Due to a separation of different scales it becomes possible to construct a QFT that is valid only for specific energy regions. By expanding in a large scale at which QCD is still perturbative, the perturbatively calculable pieces can be separated from the genuinly non–perturbative ones in physical observables.

In physics in general it is often the case that the degrees of freedom at much higher energies (or distances) do not matter for a system at a much lower scale. For instance the trajectory of a planet orbiting a star is almost completely unobstructed by the effects of general relativity. In this example Newtonian mechanics is the effective theory of general relativity in the limit of non–relativistic velocities. The same idea can also be applied when separating scales in particle interactions. When investigating scales close to the bottom mass $\mu \approx 4.5\,\mathrm{GeV}$ it is not necessary to know about the dynamics of the W-boson with $m_W \approx 80\,\mathrm{GeV}$ and so it makes sense to construct a theory in which it is not present.

An EFT is a full quantum field theory and therefore comes with regularization and

renormalization schemes necessary to obtain finite matrix elements. The key aspect of EFTs is a systematic expansion in some small parameter, which allows for well–defined predictions up to a certain order – a feature that especially QCD lacks at low energies. Due to this form of the expansion it is in general possible to calculate physical quantities to an arbitrarily high order and make errors as small as desired. In practice one is of course limited because higher order diagrams become difficult to compute or the number of non–perturbative matrix elements that need to be determined by experiment grow factorially at some point.

A great amount of EFTs was developed for all kinds of purposes and since they provide the basis for many of the calculations carried out in the course of this thesis we will introduce the ones used in the following chapters. To that end we start by a general introduction in the renormalization procedure of EFTs and thereby defining the nomenclature for the perturbative quantities used later on. Subsequently short introductions are given for the weak effective theory (specifically for b quark decays) and the Heavy Quark Effective Theory (HQET).

2.1 Basics and renormalization

In the following we consider a generic problem with two distinct energy scales Λ and μ, which fulfill $\Lambda \gg \mu$ and demonstrate how some degrees of freedom can be integrated out from the theory. The specific EFTs we will discuss later all resemble this form. The physics phenomena are described by the Lagrangian $\mathcal{L}(\varphi)$ in terms of some degrees of freedom φ. We assume that at the scale Λ some of the degrees of freedom can be neglected. In order to see how the physics of these scales can be separated, it is instructive to use the path integral formalism [29, 30]

$$Z = \int \mathcal{D}\varphi \exp\left[i \int \mathrm{d}^D x \, \mathcal{L}(\varphi)\right], \tag{2.1}$$

where D is the number of spacetime dimensions and $\mathcal{D}\varphi$ is a measure, which symbolizes the integration over all field configurations. Relabeling the field φ by exploiting the difference of the energy scales

$$\varphi = \begin{cases} \varphi_H & p > \Lambda \\ \varphi_L & p < \Lambda \end{cases} \tag{2.2}$$

and integrating out the heavy degree of freedom yields

$$Z = \int \mathcal{D}\varphi_L \int \mathcal{D}\varphi_H \exp\left[i \int \mathrm{d}^D x\, \mathcal{L}(\varphi_H, \varphi_L)\right] = \int \mathcal{D}\varphi_L \exp\left[i \int \mathrm{d}^D x\, \mathcal{L}_{\text{eff}}\right] . \quad (2.3)$$

Here the effective action was defined as

$$\int \mathrm{d}^D x\, \mathcal{L}_{\text{eff}}(\varphi_L) \coloneqq -i \ln \int \mathcal{D}\varphi_H \exp\left[i \int \mathrm{d}^D x\, \mathcal{L}(\varphi_L, \varphi_H)\right] . \quad (2.4)$$

It can be formally expanded in a power series

$$\int \mathrm{d}^D x\, \mathcal{L}_{\text{eff}}(\varphi_L) = \int \mathrm{d}^D x \sum_{n=0}^{\infty} \sum_i \frac{C_i^{(n)}}{\Lambda^n} \mathcal{O}_i^{(n)}(\varphi_L), \quad (2.5)$$

where $\mathcal{O}_i^{(n)}$ are a set of local operators built out of the fields of the low–energy theory and the $C_i^{(n)}$ are the so called Wilson coefficients. The operators $\mathcal{O}_i^{(n)}$ have dimension $D = 4 + n$ and respect all symmetries of the full theory (i.e. Lorentz invariance, gauge invariance, global symmetries like CPT, e.t.c.). Their number is in general infinite, however for each dimension D there exists only a finite set and more importantly contributions to a given observable are suppressed by $(\mu/\Lambda)^{D-4}$ compared to operators in the full theory. In physical observables, these operators appear as matrix elements and contain the long-distance behaviour of the specific process. For some processes it is possible to calculate them theoretically with lattice QCD or hadronic sum rules, however often times their value is determined by experimental measurements and serves as an additional input in the EFT. The Wilson coefficients $C_i^{(n)}$ are dimensionless, since their scale dependence has to come from the large scale Λ which was factored out in eq.(2.5). They contain all information about the short-distance physics.

We are interested in the investigation of processes at an arbitrary scale $\mu < \Lambda$. Thus we want to study the effective Lagrangian

$$\mathcal{L}_{\text{eff}} = \sum_{n=0}^{\infty} \sum_i \frac{C_i^{(n)}(\mu)}{\Lambda^n} \mathcal{O}_i^{(n)}(\mu), \quad (2.6)$$

where the scale dependence of the Wilson coefficients and operators has been made explicit. Changing μ basically moves contributions from the matrix elements of the operators to the Wilson coefficients and vice versa. Of course actual, physical observ-

ables O_{phys} cannot depend on the arbitrary scale μ and hence

$$\mu\frac{\mathrm{d}}{\mathrm{d}\mu}O_{\text{phys}} = \sum_i \left[\left(\mu\frac{\mathrm{d}C_i(\mu)}{\mathrm{d}\mu}\right)\mathcal{O}_i(\mu) + C_i(\mu)\left(\mu\frac{\mathrm{d}\mathcal{O}_i(\mu)}{\mathrm{d}\mu}\right)\right] \stackrel{!}{=} 0, \tag{2.7}$$

where we dropped the index n as the relation holds for each order separately. Note that the operators $\mathcal{O}_i$ mix under renormalization, however not in between orders as long as dimensional regularization is used to single out singularities. This makes dimensional regularization by far the most convenient regularization scheme in practice. The operators form a complete basis such that mixing can be written as a linear combination of operators with the same mass dimension

$$\mu\frac{\mathrm{d}\mathcal{O}_i(\mu)}{\mathrm{d}\mu} = \sum_j \gamma_{ij}(\mu)\mathcal{O}_j(\mu), \tag{2.8}$$

with the so called anomalous dimension matrix γ_{ij}. It can be obtained from the coefficient of the single $1/\varepsilon$ pole terms in the matrix of renormalization factors. Inserting this into eq.(2.6) gives

$$\sum_{i,j}\left[\mu\frac{\mathrm{d}C_i(\mu)}{\mathrm{d}\mu}\delta_{ij} - C_i(\mu)\gamma_{ij}(\mu)\right]\mathcal{O}_j(\mu) = 0 \tag{2.9}$$

and due to the linear independence of the basis operators this gives for each j

$$\sum_i\left[\mu\frac{\mathrm{d}C_i(\mu)}{\mathrm{d}\mu}\delta_{ij} - C_i(\mu)\gamma_{ij}(\mu)\right] = 0\,. \tag{2.10}$$

We can also write this in matrix notation as

$$\mu\frac{\mathrm{d}\vec{C}(\mu)}{\mathrm{d}\mu} = \boldsymbol{\gamma}^{\mathrm{T}}(\mu)\vec{C}(\mu)\,. \tag{2.11}$$

This differential equation defines the RG evolution of the Wilson coefficients. It is noteworthy that for example in SCET also $1/\varepsilon^2$ divergences appear and therefore an additional contribution $\sim \gamma_{\text{cusp}}(\mu)\ln \Lambda/\mu$ with the so called cusp anomalous dimension γ_{cusp} appears on the right–hand side of this equation. In order to solve eq.(2.11) we observe that all scale dependence in the coefficients must be governed by the masses and coupling constants of the theory. Basically all change in the scale μ is compensated by appropriate changes in these renormalizable quantities to finally render physical observables scale–independent. Throughout this thesis we merely consider the case

of massless QCD and therefore the only scale dependence comes from the coupling constant $\alpha_s(\mu)$. Its scale dependence is defined by the so called β function via

$$\beta(\alpha_s(\mu)) \coloneqq \mu \frac{\mathrm{d}\alpha_s(\mu)}{\mathrm{d}\mu} \tag{2.12}$$

and similarly the anomalous dimension depends only on the the strong coupling too

$$\boldsymbol{\gamma}(\mu) \equiv \boldsymbol{\gamma}(\alpha_s(\mu))\,. \tag{2.13}$$

Rewriting the derivative, eq.(2.11) becomes

$$\frac{\mathrm{d}\vec{C}(\alpha_s)}{\mathrm{d}\alpha_s} = \frac{\boldsymbol{\gamma}^{\mathrm{T}}(\alpha_s)}{\beta(\alpha_s)}\,\vec{C}(\alpha_s)\,, \tag{2.14}$$

which is just a first–order differential equation with the solution

$$\vec{C}(\alpha_s(\mu)) = \exp\left[\int_{\alpha_s(\Lambda)}^{\alpha_s(\mu)} \mathrm{d}\alpha_s\, \frac{\boldsymbol{\gamma}^{\mathrm{T}}(\alpha_s)}{\beta(\alpha_s)}\right] \vec{C}(\alpha_s(\Lambda)), \quad \alpha_s(\mu) < \alpha_s(\Lambda)\,. \tag{2.15}$$

We implicitly assume that the strong couplings are decreasing (which is the case for QCD). With known boundary conditions at the high scale $\vec{C}(\alpha_s(\Lambda))$ we can match the coefficients at some lower scale μ order by order to the full theory. The exponential has the effect of running the coefficients down to the scale we are interested in. During this process there appear potentially large logarithms $\sim \ln {}^{\Lambda}\!/_{\mu}$ which might spoil the perturbative expansion when elevating higher orders such that they are larger than the lower ones. Fortunately this problem is automatically taken care of by the solution eq.(2.15) via resummation. All potentially large logarithms will be contained in the Wilson coefficients after the process albeit in such a way that the coupling constants all come with an appropriate power of the respective logarithm.

In almost all practical calculations the β function and anomalous dimension (and also potentially other perturbative quantities like the formerly mentioned cusp anomalous dimension) are expanded as a series in α_s like

$$\beta(\alpha_s) = \alpha_s \sum_n \beta^{(n)} \left(\frac{\alpha_s}{4\pi}\right)^{n+1}, \qquad \gamma_{ij}(\alpha_s) = \sum_n \gamma_{ij}^{(n)} \left(\frac{\alpha_s}{4\pi}\right)^{n+1}. \tag{2.16}$$

Currently the β function is known up to five loops and most anomalous dimensions up to four – see appendix A.2 for their explicit form. This grants us with very precise

tools for the running of scales so they usually do not pose the bottleneck for precision calculations. Much more constraining are the non–perturbative inputs, that are contained in the matrix elements of the operators defined above.

2.2 Weak Effective Theory

The first EFT we want to introduce is the weak effective theory – specifically for decays with $\Delta B = 1$. The underlying idea is that for most processes involving flavour changes, the W boson, which serves as the mediator of the electroweak force, must not be taken into account as an actual degree of freedom for the purpose of practical calculations. The energy scale of interest (for flavour physics it is usually of order $m_b \approx 5\,\text{GeV}$) is very distinct from the scale of the W at $m_W \approx 80\,\text{GeV}$ and so it is reasonable to employ the procedure outlined in the previous section to derive an effective Lagrangian. More details about the derivation can be found in [31, 32].

The part of the generating functional that is relevant for the discussion of W bosons is given by

$$Z_W \sim \int \mathcal{D}W^+ \, \mathcal{D}W^- \exp\left(i \int \mathrm{d}^4x \, \mathcal{L}_W\right), \tag{2.17}$$

where $\mathcal{L}_W$ is the Lagrangian containing kinetic terms of the W and its interactions given by the Yukawa sector of the SM in eq.(1.15). Note that this is analogous to the general form of the generating functional in eq.(2.1) and thus following the separation of scales we can integrate out the W field from the theory. Without going into the details of the calculation we finally find the effective Hamiltonian by expanding in inverse powers of the W mass. Because m_W is so much larger than the scale in the process of interest, it usually suffices to consider only the leading order in this expansion

$$\mathcal{H}_{\text{eff}} = \frac{G_F}{\sqrt{2}} V_{ud}^* V_{u'd'} (\bar{u}d)_{\text{V}-\text{A}} (\bar{d}'u')_{\text{V}-\text{A}} \,. \tag{2.18}$$

The subscript $\text{V} - \text{A}$ refers to the Lorentz structure $\gamma^\mu(1 - \gamma_5)$ and we defined the Fermi constant as $G_F := g_2^2/2\sqrt{2}m_W^2$. By means of this procedure the W boson is fully removed from the low–energy theory as a degree of freedom. Its only remnant is cast in the Fermi constant, but all short–range exchanges in which it serves as a mediator correspond to point interactions now. The dominant contribution to these processes comes from four–fermion operators of dimension six.

Up to this point effects from the strong interaction have not been taken into account.

They must however be included when other low energy EFTs, that explicitly deal with strong interactions are matched to the weak effective theory. The other EFTs introduced throughout this thesis will implicitly be matched to the weak effective theory because it suffices to consider the high energy effects represented in its Wilson coefficients. Focusing on the relevant processes for this thesis with $\Delta B = 1$, there are three types of operators we have to include in the effective Hamiltonian. On the one hand we observe that a gluon linking two colour singlet weak currents can 'mix' the colour indices of the current–current operators. On the other hand QCD and electroweak penguin operators can be generated by attaching a gluon to the initial state via a loop. By means of these operators the effective Hamiltonian for $\Delta B = 1$ is extended to

$$\mathcal{H}_{\text{eff}} = \frac{G_F}{\sqrt{2}} \left[\sum_{i=1,2} \sum_{q=u,c} \lambda_q C_i \mathcal{O}_i^q - \sum_{i=3}^{10} \lambda_t C_i \mathcal{O}_i \right] , \tag{2.19}$$

where we abbreviated the CKM matrix elements with $\lambda_q \coloneqq V_{qb} V_{qd}^*$. The C_i are the respective Wilson coefficients to a given operator. The full basis of the operators $\mathcal{O}_i$ reads

$$\begin{aligned}
\mathcal{O}_1^q &= (\bar{b}_i q_j)_{\text{V-A}} (\bar{q}_j d_i)_{\text{V-A}} , & \mathcal{O}_2^q &= (\bar{b}_i q_i)_{\text{V-A}} (\bar{q}_j d_j)_{\text{V-A}} , \\
\mathcal{O}_3 &= (\bar{b}_i d_i)_{\text{V-A}} \sum_q (\bar{q}_i q_i)_{\text{V-A}} , & \mathcal{O}_4 &= (\bar{b}_i d_j)_{\text{V-A}} \sum_q (\bar{q}_j q_i)_{\text{V-A}} , \\
\mathcal{O}_5 &= (\bar{b}_i d_i)_{\text{V-A}} \sum_q (\bar{q}_i q_i)_{\text{V+A}} , & \mathcal{O}_6 &= (\bar{b}_i d_j)_{\text{V-A}} \sum_q (\bar{q}_j q_i)_{\text{V+A}} , \\
\mathcal{O}_7 &= \frac{3}{2} (\bar{b}_i d_i)_{\text{V-A}} \sum_q e_q (\bar{q}_i q_i)_{\text{V+A}} , & \mathcal{O}_8 &= \frac{3}{2} (\bar{b}_i d_j)_{\text{V-A}} \sum_q e_q (\bar{q}_j q_i)_{\text{V+A}} , \\
\mathcal{O}_9 &= \frac{3}{2} (\bar{b}_i d_i)_{\text{V-A}} \sum_q e_q (\bar{q}_i q_i)_{\text{V-A}} , & \mathcal{O}_{10} &= \frac{3}{2} (\bar{b}_i d_j)_{\text{V-A}} \sum_q e_q (\bar{q}_j q_i)_{\text{V-A}} .
\end{aligned} \tag{2.20}$$

A couple of comments are in order about these operators. If no QCD effects are taken into account, all Wilson coefficients except for C_2 would vanish and only $\mathcal{O}_2$ remained such that eq.(2.18) is recovered. The inclusion of QCD effects creates another current–current operator $\mathcal{O}_1$ at tree–level which has a different colour structure by means of the relation

$$T_{ik}^a T_{jl}^a = -\frac{1}{2N_c} \delta_{ik} \delta_{jl} + \frac{1}{2} \delta_{il} \delta_{jk} . \tag{2.21}$$

In addition there are four QCD penguin operators $\mathcal{O}_3$ - $\mathcal{O}_6$. Their gluon coupling is

flavour conserving and so they cannot be generated from the tree–level operators. The sum over q runs over the quarks $q = u, d, s, c, b$ for processes with $\Delta B = 1$. They are decomposed in the vector structures $\mathrm{V} - \mathrm{A}$ and $\mathrm{V} + \mathrm{A}$ and bear two different colour structures due to the exchange of a gluon. Compared to the tree–level operators their Wilson coefficients are about a magnitude smaller. The same types of diagrams can be generated by the exchange of a photon or Z–boson, which creates the electroweak penguin operators $\mathcal{O}_7$ - $\mathcal{O}_{10}$. Their coefficients are usually even more suppressed than the QCD penguins due to their dependence on the QED coupling constant e_q.

Finally when dealing with decays of b quarks into c or u quarks, there are no penguin operators because no vertices into those final states exist. Hence, at least up to NLO, only current–current operators are present for such decays.

2.3 Heavy Quark Effective Theory

We now want to turn our attention to systems that contain a heavy quark and light degrees of freedom. We can imagine this system as an almost static heavy quark with mass m_Q surrounded by a "cloud" of gluons and light quarks with which it interacts in a complicated way. The typical scale of these interactions is of the order of $\Lambda_{\mathrm{QCD}} \approx 0.3\,\mathrm{GeV}$, where QCD starts becoming non-perturbative.

In the same way as in the Weak Effective Theory, we want to integrate out the heavy degree of freedom. Thus, we want to consider a state which contains a single heavy quark. Since the flavour quantum number is conserved in QCD, the heavy quark is still present as a degree of freedom – even at low scales. It remains as a static source of colour in the effective theory.

The starting point for the construction of the EFT is the observation that a heavy quark bound inside a hadron is nearly on–shell and moves with about the velocity of the hadron defined by $p_H = m_H v$, such that the heavy quark momentum can be written as

$$p_Q^\mu = m_Q v^\mu + k^\mu \,, \tag{2.22}$$

where $k^\mu \ll m_Q$ denotes the residual momentum. We can explicitly extract the heavy phase from the quark field $Q(x)$ in full QCD and decompose it in terms of the spinors $h_v(x)$ and $H_v(x)$

$$Q(x) = \mathrm{e}^{-i m_Q v\cdot x} \left[H_v(x) + h_v(x)\right] \,, \tag{2.23}$$

where the spinors may be written as

$$h_v(x) = \mathrm{e}^{im_Q v\cdot x}\frac{1+\not{v}}{2}Q(x)\,, \qquad H_v(x) = \mathrm{e}^{im_Q v\cdot x}\frac{1-\not{v}}{2}Q(x)\,. \tag{2.24}$$

Note that the terms $P_\pm = 1/2(1 \pm \not{v})$ act as projectors on a two–dimensional subspace of the full QCD field. In the rest frame of the B meson, i.e. for $v^\mu = (1,0,0,0)$, the spinor h_v corresponds to the upper two components of $Q(x)$ and H_v to the lower ones. The QCD Lagrangian can then be written in terms of the new fields

$$\begin{aligned}\mathcal{L}_{\mathrm{QCD}} &= \bar{Q}\,(i\not{D} - m_Q)\,Q \\ &= \bar{h}_v\, iv\cdot D\, h_v - \bar{H}_v\,(iv\cdot D + 2m_Q)\,H_v + \bar{h}_v\, i\not{D}_\perp\, H_v + \bar{H}_v\, i\not{D}_\perp\, h_v\,,\end{aligned} \tag{2.25}$$

where we decomposed the covariant derivative in a *time* and *spatial* part via

$$D^\mu = (v\cdot D)v^\mu + D^\mu_\perp\,, \qquad D^\mu_\perp = (g^{\mu\nu} - v^\mu v^\nu)D_\nu\,. \tag{2.26}$$

From this form of the Lagrangian it becomes apparent that h_v describes the massless degrees of freedom, whereas H_v fluctuates with twice the heavy quark mass m_Q and hence resembles the heavy degree of freedom. We can integrate it out explicitely as scetched in chapter 2.1, because the integral over these fields is Gaussian; for a detailed derivation see [33, 34]. This leads to the effective action

$$S_{\mathrm{eff}} = \int \mathrm{d}^4x\,\mathcal{L}_{\mathrm{eff}} - i\ln\Delta\,, \tag{2.27}$$

with the effective Lagrangian of heavy quark effective theory

$$\mathcal{L}_{\mathrm{eff}} = \bar{h}_v\, iv\cdot D\, h_v + \bar{h}_v\, i\not{D}_\perp \frac{1}{iv\cdot D + 2m_Q} i\not{D}_\perp\, h_v\,. \tag{2.28}$$

The appearance of the term $\ln\Delta = 1/2\,\mathrm{tr}\ln[2m_Q + iv\cdot D - i\varepsilon]$ is a quantum effect and it can be shown that by choosing the axial gauge $v\cdot A = 0$ it is just an irrelevant constant, which does not alter the equations of motion [35]. The Gaussian integration in the path integral corresponds to the replacement for the lower component field

$$H_v = \left(\frac{1}{2m_Q + iv\cdot D}\right) i\not{D}_\perp h_v\,. \tag{2.29}$$

Since derivatives acting on h_v correspond to powers of the residual momentum k^μ in momentum space, which is much smaller than the heavy quark mass m_Q by construc-

tion, we can expand $\mathcal{L}_{\text{eff}}$ in powers of ${}^{iD}\!/_{m_Q}$ as

$$\mathcal{L}_{\text{eff}} = \bar{h}_v \, iv \cdot D \, h_v + \frac{1}{2m_Q} \sum_{n=0}^{\infty} \bar{h}_v \, i\not{D}_\perp \left(-\frac{iv \cdot D}{2m_Q} \right)^n i\not{D}_\perp \, h_v \,. \tag{2.30}$$

The same can be obtained for the QCD field (2.23) by utilizing eq.(2.29)

$$Q(x) = \mathrm{e}^{-im_Q v \cdot x} \frac{1}{2m_Q} \sum_{n=0}^{\infty} \left(-\frac{iv \cdot D}{2m_Q} \right)^n i\not{D}_\perp \, h_v \,. \tag{2.31}$$

These two results enable us to express any matrix element involving heavy-quark states as an expansion in ${}^{1}\!/_{m_Q}$.

In the heavy quark limit $m_Q \to \infty$ only the first term in the Lagrangian from eq.(2.30) remains and new symmetries emerge that are not present in full QCD. In particular, the expression is independent of the heavy quark mass and thus $SU(2)$ rotations in flavour space leave it invariant. Note that this symmetry only relates quarks moving with the same velocity. The second symmetry is the heavy quark spin symmetry. Since there appear no Dirac matrices in the leading term of eq.(2.30) it is invariant under transformations of the $SU(2)$ spin group. This becomes transparent in the rest frame, where the generators S^i of $SU(2)$ can be chosen as

$$S^i = \frac{1}{2} \begin{pmatrix} \sigma^i & 0 \\ 0 & \sigma^i \end{pmatrix}, \quad \left[S^i, S^j \right] = i\varepsilon^{ijk} S^k \,.$$

When performing an infinitesimal transformation on the field $h_v \to (1 + i\vec{\varepsilon} \cdot \vec{S}) h_v$, the Lagrangian is left invariant in the heavy quark limit

$$\delta \mathcal{L}_{\text{eff}} = \bar{h}_v \left[iv \cdot D, i\vec{\varepsilon} \cdot \vec{S} \right] h_v = 0 \,,$$

and hence all the heavy hadron states moving with the same velocity v fall into spin–symmetric doublets.

Chapter 3

Inclusive decays of B mesons

Inclusive B meson decays are very important channels for the study of all CKM–elements involving the decay of a b quark. In this chapter we specifically investigate semileptonic processes, i.e. decays of a B meson into any hadronic final state as well as a lepton–neutrino pair $B \to X\ell\bar{\nu}_\ell$. First, we summarize the basic setup for the precision calculations attempted further in this thesis. To that end we introduce the inclusive rate for the processes $b \to c$ and $b \to u$, respectively. Thereby, we show how perturbative and non–perturbative physics can be separated and define the non–perturbative parts for either process. We finally motivate the necessity of a suitable short–distance mass scheme for the decaying quarks.

3.1 The inclusive rate

We are ultimately interested in the (differential) inclusive decay rate, as it can be measured directly in experiment or serve as the basis for measurable observables. Inclusive decay rates are defined as a sum over all possible final states, i.e. the differential rate schematically reads

$$\mathrm{d}\Gamma(B \to X\ell\bar{\nu}_\ell) = \sum_f \mathrm{d}\Gamma(B \to f\ell\bar{\nu}_\ell)\,. \tag{3.1}$$

Without the specification of the kinematic variables this differential width can be used for any process and often the actual choice of kinematics is determined by the experimental setup and the cuts that can be imposed on the phase space. In general the

differential width takes the form

$$\mathrm{d}\Gamma = \sum_X \frac{1}{m_B}(2\pi)^4\delta^{(4)}(p_B - p_X)|\mathcal{M}(B \to X)|^2 \mathrm{d}\Phi_{\mathrm{PS}}\,, \tag{3.2}$$

where $\mathcal{M}$ denotes the matrix element of the decay and $\mathrm{d}\Phi_{\mathrm{PS}}$ is the phase space element. We are interested in semileptonic decays, which are mediated by an effective Hamiltonian that contains currents for the leptonic L^μ and hadronic J^μ states; similar to the one introduced in chapter 2.2

$$\mathcal{H}_{\mathrm{eff}} = \frac{4G_F}{\sqrt{2}} V_{\mathrm{CKM}} \left(\bar{q}b\right)_{\mathrm{V-A}} \left(\bar{\ell}\nu\right)_{\mathrm{V-A}} + \mathrm{h.c.} \coloneqq \frac{4G_F}{\sqrt{2}} V_{\mathrm{CKM}} J^\mu L_\mu + \mathrm{h.c.}\,, \tag{3.3}$$

where $\bar{q}$ denotes either up–type quark $q = u, c$. Note that for these final state quarks, there are no contributions of penguin operators in semileptonic decays. The final state for this process is $|f\rangle = |X\ell\bar{\nu}_\ell\rangle$ and since the currents only act on either the leptonic or hadronic states we can factorize the matrix element

$$\begin{aligned} |\mathcal{M}(B \to X\ell\bar{\nu}_\ell)|^2 &= 8G_F^2|V_{\mathrm{CKM}}|^2 \left|\langle X\ell\bar{\nu}_\ell|J_\mu L^\mu|B\rangle\right|^2 \\ &= 8G_F^2|V_{\mathrm{CKM}}|^2 \langle B|J_\alpha^\dagger|X\rangle\langle X|J_\beta|B\rangle\langle 0|L^{\dagger,\alpha}|\ell\bar{\nu}_\ell\rangle\langle\ell\bar{\nu}_\ell|L^\beta|0\rangle\,. \end{aligned} \tag{3.4}$$

Upon defining the so called hadronic and leptonic tensors by

$$W_{\mu\nu} \coloneqq \sum_X \langle B|J_\mu^\dagger|X\rangle\langle X|J_\nu|B\rangle(2\pi)^3\delta^{(4)}(p_B - p_X) \tag{3.5}$$

$$L_{\mu\nu} \coloneqq \sum_{\mathrm{spins}} \langle 0|L_\mu^\dagger|\ell\bar{\nu}_\ell\rangle\langle\ell\bar{\nu}_\ell|L_\nu|0\rangle\,, \tag{3.6}$$

we can rewrite the differential decay rate in a more suitable form that makes the separation of leptonic and hadronic contributions manifest

$$\mathrm{d}\Gamma = \frac{8\pi G_F^2|V_{\mathrm{CKM}}|^2}{m_B} W_{\mu\nu}L^{\mu\nu}\mathrm{d}\Phi_{\mathrm{PS}}\,. \tag{3.7}$$

Note that we had defined the leptonic tensor with a sum over the lepton spins, since experimentally these are never measured, but rather averaged and so we can explicitly calculate it with the usual trace evaluations

$$L^{\mu\nu} = 2(k^\mu k'^\nu + k^\nu k'^\mu - g^{\mu\nu}k\cdot k' - i\varepsilon^{\alpha\nu\beta\mu}k_\alpha k'_\beta)\,, \tag{3.8}$$

where k and k' are the momenta of the lepton and neutrino respectively. Since we do not consider decays in the heavy τ lepton, all masses in this expression have been

neglected. The hadronic tensor contains the non–perturbative parts of the calculation. It takes different forms for either the decay into a charm or up quark, and thus we will consider each final state separately in the next chapters.

3.2 Inclusive $b \to c$ decays

Similar to the procedure outlined in chapter 2.3, we want to exploit the fact that the mass of the decaying b quark is much heavier than its final state. In doing so, it becomes possible to systematically introduce corrections to the tree–level results of the respective decay rate in an expansion of the inverse heavy quark mass. This procedure separates the effects of perturbative and non–perturbative parts in the hadronic tensor in a local OPE. We furthermore exploit the invariance under reparameterization to reduce the number matrix elements at a given order in the inverse heavy mass.

3.2.1 The Heavy Quark Expansion

The triple differential rate from eq.(3.7) for an inclusive $b \to c$ decay in terms of the lepton invariant mass q^2 and their energies E_ν and E_ℓ reads explicitly

$$\frac{\mathrm{d}^3\Gamma}{\mathrm{d}q^2\mathrm{d}E_\nu\mathrm{d}E_\ell} = \frac{G_F^2 V_{cb}^2}{2\pi^3}\left(q^2 W_1 + (2E_\ell E_\nu - q^2/2)W_2 + q^2(E_\ell - E_\nu)W_3\right) , \tag{3.9}$$

where phase space is restricted by $4E_\ell E_\nu - q^2 \geq 0$ and we explicitely used the leptonic tensor from eq.(3.8). Note that without cuts on the lepton energy, the integration over the lepton energies can be carried out analytically, yielding the differential q^2 rate, which is used in chapter 5.

We want to cast the hadronic tensor $W^{\mu\nu}$ into a form that separates the perturbative parts from the non–perturbative ones in a systematic way. To that end, we employ an OPE in inverse powers of the b quark mass in this chapter. Upon noticing that the b quark in the bound state has a small momentum relative to that of the B meson, we can utilize the methods discussed in chapter 2.3 and expand in terms of the residual momentum. First we relate the hadronic tensor to a correlator of hadronic currents via the optical theorem [24, 36]. For one–particle decays it basically states that the forward transition amplitude is equal to the imaginary part of the production of intermediate states. Hence we may write the hadronic tensor as

$$W^{\mu\nu} = -\frac{1}{\pi}\mathrm{Im}\, T^{\mu\nu} , \tag{3.10}$$

where we defined the correlator of the hadronic currents

$$T^{\mu\nu} = \int \mathrm{d}^4x\, \mathrm{e}^{-iq\cdot x}\langle B|\mathrm{T}\{J^{\dagger,\mu}(x)J^{\nu}(0)\}|B\rangle\,. \tag{3.11}$$

For the purpose of calculations it is advantageous to perform a Lorentz decomposition of the hadronic tensor

$$W_{\mu\nu} = -g_{\mu\nu}W_1 + v_\mu v_\nu W_2 - i\varepsilon_{\mu\nu\alpha\beta}v^\alpha q^\beta W_3 + q_\mu q_\nu W_4 + (q_\mu v_\nu + v_\mu q_\nu)W_5\,. \tag{3.12}$$

A similar expansion can also be done for the correlator such that the structure functions are again related by the optical theorem $W_j = -1/\pi \mathrm{Im}\, T_j$. To exploit the effects of the heavy quark mass we extract its fluctuations of the b quark field

$$b_v(x) = \mathrm{e}^{im_b v\cdot x} b(x)\,. \tag{3.13}$$

Note that this is still the full QCD field and we merely redefined its phase. With the different scales now manifestly separated, we may finally perform the OPE and write the correlator schematically as

$$T_{\mu\nu} = \sum_{n=0}^{m} C_{n,\mu\nu}^{\mu_1\ldots\mu_n}(m_b, v)\langle B|\mathcal{O}^{n+3}_{\mu_1\ldots\mu_n}|B\rangle\,. \tag{3.14}$$

The Wilson coefficients C_n contain the perturbative pieces of the hadronic correlator so they each include an expansion in α_s. The matrix elements of the operators $\mathcal{O}^{n+3}$ resemble all non–perturbative pieces coming from the binding of the quark in the hadron. To find their exact form it has proven useful to expand the correlator with the help of a background field [37, 38]. We define it as

$$S_{\mathrm{BGF}} \coloneqq \frac{1}{\not{Q} + i\not{D} - m_c}\,, \qquad Q_\mu = m_b v_\mu - q_\mu\,. \tag{3.15}$$

The expression up to order $1/m_b^k$ can be obtained by expanding the background field in terms of the residual momentum $i\not{D}$

$$S_{\mathrm{BGF}} = \frac{1}{\not{Q} - m_c}\sum_{n=0}^{k}\left((i\not{D})\frac{-1}{\not{Q} - m_c}\right)^n\,. \tag{3.16}$$

This eventually yields the respective T_i as an expansion in inverse powers of the prop-

agator

$$\Delta_0 = (m_b v - q)^2 - m_c^2 \,, \tag{3.17}$$

whose imaginary part is given by corresponding delta distributions and their derivatives as

$$-\frac{1}{\pi}\mathrm{Im}\left(\frac{1}{\Delta_0}\right)^{n+1} = \frac{(-1)^n}{n!}\,\delta^{(n)}\left((m_b v - q)^2 - m_c^2\right) \,. \tag{3.18}$$

The expansion eq.(3.16) shows furthermore, that the non–perturbative matrix elements have the general form

$$\langle B|\mathcal{O}^{n+3}_{\mu_1\ldots\mu_n}|B\rangle = \langle B|\bar{b}_v(iD_{\mu_1})\cdots(iD_{\mu_n})b_v|B\rangle \,. \tag{3.19}$$

The remaining task is to relate these matrix elements to a basic set of non–perturbative HQE parameters. It is important to note that they are not tied to the actual process that is considered here, and so, once determined with experimental data, can be used for several decays involving a heavy quark.

All fields and operators are still in full QCD (they were only rephased) and therefore operators at a given dimension might contain corrections in higher orders of $1/m_b$. In fact using the equations of motions of HQET, we may derive a set of relations to show the explicit correspondence to higher orders in the inverse b quark mass

$$\begin{aligned}
\not{v} b_v &= b_v - \frac{1}{m_b} i\not{D} b_v \,, \\
P_+ b_v &= -\frac{1}{2m_b} i\not{D} b_v + b_v \,, \\
P_- b_v &= \frac{1}{2m_b} i\not{D} b_v \,, \\
(iv\cdot D) b_v &= -\frac{1}{2m_b} i\not{D} i\not{D} b_v \,.
\end{aligned} \tag{3.20}$$

Here we defined the projection operators $P_\pm \coloneqq 1/2(1 \pm \not{v})$ onto two–component subspaces analogous to the ones that appeared in eq.(2.24). The calculational procedure that was carried out in [37, 38] works in a recursive fashion. It starts at the highest desired dimension for the respective operator, where one can use eqs.(3.20) in the static limit, i.e. no further $1/m_b$ corrections to the matrix element at that order will appear. Subsequently a minimal set of matrix elements at the given order is defined, to which the operators of lower dimension can be related by the equations of motion. In the

following we give the definitions and physical interpretation of the matrix elements for increasing powers of $1/m_b$.

The lowest order terms in the OPE are dimension three operators of the form $\bar{b}_v b_v$. At leading order in the $1/m_b$ expansion the corresponding matrix element contains only the normalization of the states

$$2m_B = \langle B|\bar{b}_v \not{v} b_v|B\rangle \,. \tag{3.21}$$

The terms at the next higher order would be proportional to $1/m_b$. They vanish however due to the equations of motion. Note that this statement is generally true by means of Luke's theorem [39]. Consequently the next HQE parameters enter at order $1/m_b^2$ and come from the dimension five operators. They are defined as

$$\begin{aligned} 2m_B\mu_\pi^2 &= -\langle B|\bar{b}_v (iD)^2 b_v|B\rangle \\ 2m_B\mu_G^2 &= \langle B|\bar{b}_v (iD_\mu)(iD_\nu)(-i\sigma^{\mu\nu}) b_v|B\rangle \,. \end{aligned} \tag{3.22}$$

Physically μ_π^2 is proportional to the square of the residual momentum k and therefore referred to as the kinetic term, and μ_G^2 describes the coupling of the heavy quark spin to the chromomagnetic field inside the heavy hadron. At dimension six, i.e. order $1/m_b^3$ there are two additional parameters defined as

$$\begin{aligned} 2m_B\rho_{\rm D}^3 &= \frac{1}{2}\langle B|\bar{b}_v \left[(iD_\mu),[(iv\cdot D),(iD^\mu)]\right] b_v|B\rangle \\ 2m_B\rho_{\rm LS}^3 &= \frac{1}{2}\langle B|\bar{b}_v \{(iD_\mu),[(iv\cdot D),(iD_\nu)]\}(-i\sigma^{\mu\nu}) b_v|B\rangle \,. \end{aligned} \tag{3.23}$$

The Darwin term $\rho_{\rm D}^3$ is related to the divergence of the chromoelectric field $\nabla\cdot\mathbf{E}$ and the spin–orbit term $\rho_{\rm LS}^3$ to its curl $\mathbf{s}\cdot\nabla\times\mathbf{E}$. The dimension seven operators introduce an additional nine parameters in general, which we discuss in the context of reparameterization invariance in chapter 3.2.2.

We emphasize that there are other conventions for defining the HQE–parameters. For example in [38, 40] they are given in terms of a spatial covariant derivative as defined in eq.(2.26), which makes a difference in higher orders of $1/m_b$. Explicit conversions are given in [41] (App. A). Furthermore it is possible to define the parameters with actual HQET fields, instead of the rephased full QCD fields. There are no $1/m_b$ corrections to the matrix elements then, however one must make up for that by adding additional contributions to get the full results. This is for example shown in [42]. No matter how the matrix elements are defined, their operator basis always has the same dimension

and thus there is no general advantage for choosing one definition over another.

In addition note that the number of parameters at $\mathcal{O}(1/m_b^4)$ is already quite large, which is becoming factorially worse with higher orders in the OPE. This makes it relatively difficult to determine them with meaningful errors from experimental data. Therefore it is desirable to find observables that depend on a reduced set of parameters, yet fully resemble all contributions from dimension seven operators.

Finally we want to remark on perturbative corrections to the differential rate $\mathrm{d}\Gamma$ in the HQE. For illustrations we may write it schematically as

$$\mathrm{d}\Gamma = \mathrm{d}\Gamma_0 + \mathrm{d}\Gamma_{\mu_\pi} \frac{\mu_\pi^2}{m_b^2} + \mathrm{d}\Gamma_{\mu_G} \frac{\mu_G^2}{m_b^2} + \mathcal{O}\left(\frac{1}{m_b^3}\right), \tag{3.24}$$

where the $\mathrm{d}\Gamma_i$ obey a perturbative expansion in the strong coupling

$$\mathrm{d}\Gamma_i = \mathrm{d}\Gamma_i^{(0)} + \mathrm{d}\Gamma_i^{(1)} \frac{\alpha_s}{\pi} + \mathrm{d}\Gamma_i^{(2)} \frac{\alpha_s^2}{\pi^2} + \dots \tag{3.25}$$

The calculation of the perturbative corrections to $\mathrm{d}\Gamma_0$ is generally straightforward but gets quite complicated at higher orders, since more and more loop diagrams need to be taken into account. For the higher powers, determinations are even more involved. To compute those Wilson coefficients it is necessary to calculate the respective loop diagrams while simultaneously taking into account the expansion in the charm propagator. In this, additional gluon matrix elements need to be considered, which render the calculation more complicated. We will return to this issue in chapter 5.1.2.

3.2.2 Reparameterization invariance

In chapter 2.3 we demonstrated how an expansion in inverse heavy quark masses can be set up. We exploited the fact that the residual momentum of the heavy quark is small and that its velocity is linked to that of the composite hadron. Even though a natural choice for this velocity is defined by $v = p_H/m_H$, i.e. the momentum and mass of the heavy meson, this choice is by no means unique.

The fact that the final result should be independent of the choice of v is known as Reparameterization Invariance (RPI) [43, 44]. It is related to the Lorentz invariance of QCD [45] and was investigated in depth for inclusive decays, for example in [46, 47, 48].

In the course of this section we want to introduce the basic idea of RPI and subsequently use it to lessen the number of parameters necessary for the description of

inclusive decays. In particular we will investigate this for the HQE parameters at order $1/m_b^4$. In turn we will write down the full set of matrix elements which we utilize for the determination of V_{cb} in chapter 5.

The reparameterization transformation δ_{RP} resembles the infinitesimal variation of the velocity v, such that

$$v_\mu \mapsto v_\mu + \delta v_\mu \,, \qquad v \cdot \delta v = 0 \,. \tag{3.26}$$

This immediately yields the transformation properties of the different building blocks in the HQE

$$\begin{aligned} \delta_{\mathrm{RP}}\, v_\mu &= \delta v_\mu \,, \\ \delta_{\mathrm{RP}}\, iD_\mu &= -m_b \delta v_\mu \,, \\ \delta_{\mathrm{RP}}\, b_v(x) &= i m_b (x \cdot \delta v) b_v(x) \,, \end{aligned} \tag{3.27}$$

where the last relation follows from the rephasing of the b quark field eq.(3.13). We want to apply the transformation to the hadronic correlator of eq.(3.14), because its left–hand side must be independent of v and is therefore RPI. The same is true for the OPE itself, but only if the full sum, i.e. all operators, are considered. Applying the transformation yields

$$\begin{aligned} 0 \stackrel{!}{=} \delta_{\mathrm{RP}} T_{\mu\nu} = &\sum_{n=0}^{m} \left[\delta_{\mathrm{RP}} C^{\mu_1 \ldots \mu_n}_{n,\mu\nu}\right] \langle B | \mathcal{O}^{n+3}_{\mu_1 \ldots \mu_n} | B \rangle \\ &+ \sum_{n=0}^{m} C^{\mu_1 \ldots \mu_n}_{n,\mu\nu} \left[\delta_{\mathrm{RP}} \langle B | \mathcal{O}^{n+3}_{\mu_1 \ldots \mu_n} | B \rangle\right] \,. \end{aligned} \tag{3.28}$$

In order to explicitly determine the RP transformation acting on the matrix element, we use their general form consisting of covariant derivatives as given in eq.(3.19). The fields in this expression do not transform as they are evaluated at zero, so using the transformation property of the covariant derivative from eq.(3.27) gives

$$\begin{aligned} \delta_{\mathrm{RP}} \langle B | \mathcal{O}^{n+3}_{\mu_1 \ldots \mu_n} | B \rangle = &- m_b \delta v_{\mu_1} \langle B | \bar{b}_v (iD_{\mu_2}) \cdots (iD_{\mu_n}) b_v | B \rangle - \ldots \\ &- m_b \delta v_{\mu_n} \langle B | \bar{b}_v (iD_{\mu_1}) \cdots (iD_{\mu_{n-1}}) b_v | B \rangle \,. \end{aligned} \tag{3.29}$$

Since eq.(3.28) must hold order by order, we can read off a relation between different

orders in $1/m_b$

$$\delta_{\mathrm{RP}} C_{n,\mu\nu}^{\mu_1\ldots\mu_n} = m_b\, \delta v_\alpha \left(C_{n+1,\mu\nu}^{\alpha\mu_1\ldots\mu_n} + \cdots + C_{n+1,\mu\nu}^{\mu_1\ldots\mu_n\alpha} \right) . \tag{3.30}$$

This poses a remarkable result as it allows to relate different orders of the HQE with each other. Thus by applying eq.(3.30) to an observable that is RPI, it is possible to reduce the number of parameters that need to be determined experimentally. In turn this paves the way for a fully data–driven extraction of quantities up to $\mathcal{O}(1/m_b^4)$.

When using the RPI relations, the reduced set of parameters reads [41, 48]

$$\langle B|\bar{b}_v b_v|B\rangle = 2m_B\mu_3\,, \tag{3.31a}$$

$$\langle B|\bar{b}_v (iD_\alpha)(iD_\beta)(-i\sigma^{\alpha\beta}) b_v|B\rangle = 2m_B\mu_G^2\,, \tag{3.31b}$$

$$\frac{1}{2}\langle B|\bar{b}_v \left[(iD_\mu)\,, \left[\left(ivD + \frac{1}{2m_b}(iD)^2 \right)\,, (iD^\mu) \right] \right] b_v|B\rangle = 2m_B\rho_D^3\,, \tag{3.31c}$$

$$\langle B|\bar{b}_v \left[(iD_\mu)\,, (iD_\nu) \right] \left[(iD^\mu)\,, (iD^\nu) \right] b_v|B\rangle = 2m_B r_G^4\,, \tag{3.31d}$$

$$\langle B|\bar{b}_v \left[(ivD)\,, (iD_\mu) \right] \left[(ivD)\,, (iD^\mu) \right] b_v|B\rangle = 2m_B r_E^4\,, \tag{3.31e}$$

$$\langle B|\bar{b}_v \left[(iD_\mu)\,, (iD_\alpha) \right] \left[(iD^\mu)\,, (iD_\beta) \right] (-i\sigma^{\alpha\beta}) b_v|B\rangle = 2m_B s_B^4\,, \tag{3.31f}$$

$$\langle B|\bar{b}_v \left[(ivD)\,, (iD_\alpha) \right] \left[(ivD)\,, (iD_\beta) \right] (-i\sigma^{\alpha\beta}) b_v|B\rangle = 2m_B s_E^4\,, \tag{3.31g}$$

$$\langle B|\bar{b}_v \left[iD_\mu\,, \left[iD^\mu\,, \left[iD_\alpha\,, iD_\beta \right] \right] \right] (-i\sigma^{\alpha\beta}) b_v|B\rangle = 2m_B s_{qB}^4\,. \tag{3.31h}$$

We denote a couple of specific points about these relations. First of all we realize that, as predicted, employing the RPI relations reduces the number of independent matrix elements up to $\mathcal{O}(1/m_b^4)$ from a total of thirteen parameters down to only eight. The strongest reduction comes from the dimension seven operators, where now only five matrix elements are present. The matrix element μ_3, that appears at tree level here, is related to the matrix elements at order $1/m_b^2$ by the equations of motion via the relation

$$\mu_3 = 1 + \frac{\mu_\pi^2 - \mu_{\mathrm{G}}^2}{2m_b^2}\,. \tag{3.32}$$

Therefore this representation is related to the one including μ_π^2, but there are some caveats to it, that we discuss in detail in chapter 5.2.2. In addition, some of the matrix elements from the full evaluation are combined in a single parameter here,

because RPI strictly relates their coefficients such that they can be written as a linear combination. For instance ρ_D^3 is defined with its RPI completion, i.e. we have added a higher order contribution to make the expression RPI. Also the spin–orbit coupling $\rho_{\rm LS}$ from eq.(3.23) is now missing because it does not appear in RPI observables [38, 49].

3.3 Inclusive $b \to u$ decays

In the previous chapter we saw how to construct a short–distance expansion in form of an OPE for semileptonic $b \to c$ decays. The same procedure can also be applied when discussing $b \to u$. However, due to the large charm background experimental cuts on the phase space must be imposed, enhancing the importance of the endpoint regions that show a pathological behaviour when interpreted point by point. Several attempts were made in treating these endpoint regions to leading [50, 51, 52] and subleading order [53, 54, 55, 56] by resumming the singular terms into a non–local object – the shapefunction – which embodies all non–perturbative structures in this region of phase space. In this chapter we review a method that utilizes the Soft Collinear Effective Theory (SCET) which allows us to systematically include perturbative corrections and (sub)leading contributions from the shapefunctions in calculations of the partial rate. First we define suitable kinematical variables and give a master formula for the partial rate including different cuts. Subsequently we motivate the definition of the shapefunction and discuss its properties. Finally we show how a factorized form of the hadronic tensor can be used to systematically introduce perturbative corrections at different energy scales.

3.3.1 Kinematics and the differential decay rate

In the region of phase space that we are interested in, the energy of the hadronic final state is much larger than its invariant mass and thus some components of the hadronic jet momentum p^μ are larger than others. In this situation one usually expands the correlator in light–cone coordinates [52, 57]. We consider the B meson to be at rest such that $v^\mu = (1,0,0,0)$ and the lepton momentum $\vec{q}$ points in the negative z–direction. In addition we define the light–like vectors $n^\mu = (1,0,0,1)$ and $\bar{n}^\mu = (1,0,0,-1)$, which satisfy $n \cdot \bar{n} = 2$ and $n \cdot v = \bar{n} \cdot v = 1$. This allows us to write every four–vector in this

basis as

$$p^\mu = (n\cdot p)\frac{\bar{n}^\mu}{2} + (\bar{n}\cdot p)\frac{n^\mu}{2} + p_\perp^\mu \coloneqq p_+^\mu + p_-^\mu + p_\perp^\mu \,. \tag{3.33}$$

The different components of the vector defined above $(p_+, p_-, p_\perp)$ scale differently in the phase space region under consideration. Because of our assumptions the minus component scales like the (large) energy $p_- \sim E$. The scaling of the plus component $p_+ \sim m^2/E$ and the perpendicular one $p_\perp \sim m$ follow from the consideration of the invariant mass $p^2 = p_+p_- + p_\perp^2 = m^2 \ll E^2$. Thus upon introducing a dimensionless scaling variable $\lambda \coloneqq m/E$, we see that the components of the four–momentum scale like

$$(p_+, p_-, p_\perp) \sim E\left(\frac{m^2}{E^2}, 1, \frac{m}{E}\right) = E(\lambda^2, 1, \lambda)\,. \tag{3.34}$$

In this region of phase space, we therefore have three different scales that we will systematically disentangle in chapter 3.3.3 to separate perturbative and non–perturbative physics. Note that for the process at hand, where the B meson is at rest, we can explicitly identify the scaling of the minus component as $p_- \sim m_b$ and of the plus component as $p_+ \sim \Lambda_{\rm QCD}$, such that the perpendicular component then scales like $p_\perp \sim \sqrt{m_b\Lambda_{\rm QCD}}$.

It is advantageous for the kinematic structure of the triple differential rate below, to decompose the hadronic tensor $W^{\mu\nu}$ in these light–cone coordinates

$$\begin{aligned} W^{\mu\nu} \;=\; & (n^\mu v^\nu + n^\nu v^\mu - g^{\mu\nu} - i\epsilon^{\mu\nu\alpha\beta} n_\alpha v_\beta)\,\tilde{W}_1 - g^{\mu\nu}\,\tilde{W}_2 \\ & + v^\mu v^\nu\,\tilde{W}_3 + (n^\mu v^\nu + n^\nu v^\mu)\,\tilde{W}_4 + n^\mu n^\nu\,\tilde{W}_5\,. \end{aligned} \tag{3.35}$$

Note that it has a different structure than the one in eq.(3.12), but the components W_i and $\tilde{W}_i$ are directly related.

Apart from the coordinate basis mentioned above there is another set of hadronic variables that has proven very useful for the processes at hand [21, 58]

$$P_\ell = m_B - 2E_\ell, \qquad P_- = E_H + |\vec{P}_H|, \qquad P_+ = E_H - |\vec{P}_H|\,. \tag{3.36}$$

In this $P_\pm$ are the light–cone components of the hadronic final state momentum, E_ℓ is the lepton energy and E_H and $\vec{P}_H$ are the energy and three–momentum of the hadronic jet. The hadronic and light–cone variables are related by $P_+ = n\cdot P_H$ and $P_- = \bar{n}\cdot P_H$.

The phase space in these variables has a simple form

$$\frac{m_\pi^2}{P_-} \leq P_+ \leq P_\ell \leq P_- \leq m_B \,, \tag{3.37}$$

with m_π being the lightest possible final state and m_B being the heaviest. Furthermore the hadronic and leptonic invariant masses m_X^2 and q^2 can be written

$$m_X^2 = P_+ P_- \,, \qquad q^2 = (m_B - P_+)(m_B - P_-) \,, \tag{3.38}$$

which makes it easier to apply the necessary kinematical cuts to the phase space. Usually we will constrain the invariant mass such that the charm background is subtracted, i.e. $P_+P_- < m_D^2$. However it can also be advantageous to apply cuts that are more applicable from the experimental point of view, for example in q^2 or E_ℓ.

The triple differential rate can be written with these variables as [20, 21]

$$\begin{aligned}\frac{\mathrm{d}^3\Gamma_u}{\mathrm{d}P_+\,\mathrm{d}P_-\,\mathrm{d}P_\ell} =& \frac{G_F^2|V_{ub}|^2}{16\pi^3}\,(m_B - P_+)\Big[(P_- - P_\ell)(m_B - P_- + P_\ell - P_+)\,f_1 \\ &+ (m_B - P_-)(P_- - P_+)\,f_2 + (P_- - P_\ell)(P_\ell - P_+)\,f_3\Big] \,,\end{aligned} \tag{3.39}$$

where we defined the structure functions f_i, that are related to the components of the hadronic tensor from eq.(3.35)

$$f_1 = \tilde{W}_1 \,, \qquad f_2 = \frac{\tilde{W}_2}{2} \,, \qquad f_3 = \left(\frac{y}{4}\,\tilde{W}_3 + \tilde{W}_4 + \frac{1}{y}\,\tilde{W}_5\right) \,, \tag{3.40}$$

and for convenience we also defined the kinematic variable y

$$y \coloneqq \frac{P_- - P_+}{m_B - P_+} \,. \tag{3.41}$$

The structure functions contain all physical information about the decay – we discuss their particular features in chapters 3.3.3 and 6.2.2. Note that writing the decay rate this way has the added benefit, that any dependence on the quark mass only enters through the structure functions.

The integration in the variables P_ℓ and P_- can be carried out analytically and thus we find a formula for the P_+ spectrum, which is particularly suited for applying any cuts on the phase space. Only the final integration in P_+ must be performed numerically then, to obtain the partial inclusive rate. We give the final formula for the rate in appendix A.4.

3.3.2 Leading shape function in the light cone expansion

Before we turn our attention to the perturbative corrections of the structure functions from eq.(3.40), we show how the non–perturbative quantities enter in the region of phase space described above. As mentioned, we can in general apply the same procedure that we had for the OPE of $b \to c$. However, for the case at hand, we are interested in a region of phase space in which there are three different scales shown in eq.(3.34) and therefore we cannot simply expand in the residual momentum anymore. Thus, in order to find the particular form of the non–perturbative matrix elements, we write the background field eq.(3.15) in the light cone coordinates introduced above and take the limit $m_u \to 0$. First we write the propagator of the up quark in a background field as

$$\frac{1}{\not{Q} + i\not{D}} = \frac{1}{2}\left\{(\not{Q} + i\not{D}), \frac{1}{(\not{Q} + i\not{D})^2}\right\} . \tag{3.42}$$

In light–cone coordinates the squared term can be written as

$$\frac{1}{(\not{Q} + i\not{D})^2} = \frac{1}{(\bar{n}\cdot Q)(n\cdot Q) + (\bar{n}\cdot Q)(in\cdot D) + (n\cdot Q)(i\bar{n}\cdot D) + (i\not{D})^2} . \tag{3.43}$$

Since the covariant derivative corresponds to the residual momentum, it scales like $\sim \lambda^2$ and thus the first two component are $\sim \lambda^2$, while the latter two are $\sim \lambda^4$, so we can expand

$$\frac{1}{(\not{Q} + i\not{D})^2} = \frac{1}{(\bar{n}\cdot Q)}\frac{1}{(n\cdot Q) + (in\cdot D)} + \mathcal{O}\left(\frac{1}{\bar{n}\cdot Q^2}\right) . \tag{3.44}$$

Note that the higher order terms generate the subleading shape functions, which we will explicitly add to our structure functions in chapter 6.2.2. To leading order the expansion of the background field from eq.(3.42) may now be written as

$$\frac{1}{\not{Q} + i\not{D}} = \frac{1}{2}\not{\bar{n}}\frac{1}{(n\cdot Q) + (in\cdot D)} + \mathcal{O}\left(\frac{1}{\bar{n}\cdot Q}\right) . \tag{3.45}$$

With this procedure it is possible to generate the higher order contributions in the light–cone expansion to the $b \to u$ rate similar to how we did in chapter 3.2.1 for $b \to c$. Note that since $\bar{n}\cdot Q \sim E \sim m_b$, by the power counting introduced in the previous chapter, this effectively is an expansion in the inverse heavy quark mass again. However, when taking the forward matrix element to obtain the corresponding

element of the correlator, we see that at leading order

$$\begin{aligned}\langle B|\bar{b}_v\Gamma\frac{1}{\not{Q}+i\not{D}}b_v|B\rangle =&\frac{1}{2}\langle B|\bar{b}_v\Gamma\frac{1}{(n\cdot Q)+(in\cdot D)}b_v|B\rangle\\ =&\frac{1}{2}\int \mathrm{d}\omega\,\frac{1}{(n\cdot Q)+\omega}\,\langle B|\bar{b}_v\Gamma\delta(\omega-(in\cdot D))b_v|B\rangle\,,\end{aligned}\tag{3.46}$$

where Γ denotes all possible Dirac structures from the currents and the expansion. We see that, in contrast to the *local* matrix elements in chapter 3.2.1, the structure that appears in the light–cone expansion is *non–local*. We define the shape function $S(\omega)$ of the process in terms of this matrix element

$$\langle B|\bar{b}_v\Gamma\delta(\omega-(in\cdot D))b_v|B\rangle = \mathrm{tr}\left(\Gamma\frac{1+\not{v}}{2}\right)S(\omega)\,,\tag{3.47}$$

where we used the HQET trace formalism [59] to resolve the Dirac structures. The shape function contains all non–perturbative dynamics that encode the Fermi motion of the heavy quark inside the B meson. It cannot be calculated from first principles, but by comparison with the local OPE, we can relate its moments to the local matrix elements [54, 60]. Since those are in general accessible experimentally, we can extract some information on $S(\omega)$. In chapter 6.1 we use this information to construct several models for the shape function. In addition, note that the shape function has support for $\omega \in]-\infty, \bar{\Lambda}]$ as was shown in [20, 61]. We will often make use of a shifted version of $S(\omega)$ however, where we define $\hat{\omega} \coloneqq \bar{\Lambda}-\omega$, such that the support is for $\hat{\omega} \geq 0$, which simplifies some of the convolutions.

3.3.3 Perturbative corrections

Apart from the power–corrections in the light–cone expansion of the former chapter, there are perturbative corrections to the rate, that we want to incorporate into the structure functions of eq.(3.40). The most straightforward way to do so, is to factorize the contributions from the three different scales present. The appropriate effective theory to integrate out any fluctuations associated with the hard scale p_-, defined in eq.(3.34) and to disentangle the three different scales, is $\mathrm{SCET_I}$. It has been discussed in detail in literature [62, 63, 64] and was reviewed for example in [61, 65, 66].

At leading order, the factorized form of the structure functions was derived in [20,

21] and reads

$$f_i^{(0)}(P_+, y) = H_{ui}(y, \mu_i) \int_0^{P_+} \mathrm{d}\hat{\omega}\, y m_b J(y m_b (P_+ - \hat{\omega}), \mu_i) \hat{S}(\hat{\omega}, \mu_i)\,, \tag{3.48}$$

where the hard functions H_{ui} include contributions at the hard scale $\mu_h \sim m_b$, the jet functions J include physics at an intermediate scale $\mu_i \sim \sqrt{\Lambda_{\mathrm{QCD}} m_b}$ and the shape function $\hat{S}$, that was introduced in the previous chapter, describes non–perturbative physics at the soft scale $\mu_0 \sim \mathcal{O}(\Lambda_{\mathrm{QCD}})$. Achieving a factorization of the different contributions poses a great advantage, because we may now use results for each of these functions at their natural scale, where they contain no large logarithms. Subsequently we use the RGEs, introduced in chapter 2.1, to evolve them to a common scale, at which we want to evaluate them. Note that the hatted notation for ω and $S(\omega)$ is used to shift the integration variable defined by $\hat{\omega} \equiv \bar{\Lambda} - \omega$, where $\bar{\Lambda} = m_B - m_b$ in the Heavy Quark limit and thus the shape function has support for $\hat{\omega} \geq 0$.

The hard functions H_{ui} are obtained by matching the weak effective Hamiltonian onto the current operators in SCET. The higher order corrections have been found at NLO [20, 63] and NNLO [67, 68, 69]. The jet functions J can be determined by evaluating one– and two–loop corrections to the SCET current correlator, giving the NLO [20] and NNLO [70] contributions. Finally there are also perturbative corrections to the soft function S, that determine its radiative tail (more details in chap 6.1). They were determined up to NNLO too [71, 72]. All of the contributions mentioned above, can be found in appendix A.1 up to $\mathcal{O}(\alpha_s^2)$ for completeness.

Having determined the perturbative corrections to the above quantities, we need to evolve them to a common scale at which we want to evaluate them. It is natural to choose the intermediate scale μ_i for this purpose, as the jet functions are without large logarithms there and it lies parametrically in the middle of the scales [1]. To that end, we need to evolve the hard function down from the hard scale μ_h and the shape function up from μ_0.

For the hard function, we may use the methods discussed in chapter 2.1, i.e. the

[1] Actually one would choose an auxiliary scale $\bar{\mu}$ and evolve all three quantities to it. After evaluating the RGEs this arbitrary scale would then drop out again (see [58]). For the purpose of illustrating, which perturbative quantities enter due to the running, it suffices to immediately choose μ_i as the default scale.

relevant exponent for the running of the scale follows from the RGE

$$\frac{\mathrm{d}}{\mathrm{d}\ln\mu} H_{ui}(y,\mu) = 2\gamma_J(y,\mu) H_{ui}(y,\mu)\,, \tag{3.49}$$

where γ_J is the anomalous dimension of the semileptonic current in SCET. It contains an additional term that depends logarithmically on the scale, due to $1/\varepsilon^2$ poles in the renormalization factor mentioned earlier

$$\gamma_J(y,\mu) = \Gamma_{\text{cusp}}(\alpha_s) \ln\frac{m_b y}{\mu} + \gamma'(\alpha_s)\,. \tag{3.50}$$

Here Γ_{cusp} is the universal cusp anomalous dimension in SCET [73] and γ' contains the non–cusp parts. The solution to eq.(3.49), for example derived in [20, 74], reads

$$H_{ui}(y,\mu_i) = \exp\left[2\mathcal{S}(\mu_h,\mu_i) - 2a_{\gamma'}(\mu_h,\mu_i) - 2a_\Gamma(\mu_h,\mu_i)\ln\frac{m_b y}{\mu_h}\right] H_{ui}(y,\mu_h)\,, \tag{3.51}$$

where the Sudakov exponent $\mathcal{S}$ and the anomalous exponent a_Γ are given by

$$\mathcal{S}(\nu,\mu) = -\int\limits_{\alpha_s(\nu)}^{\alpha_s(\mu)} \mathrm{d}\alpha\, \frac{\Gamma_{\text{cusp}}(\alpha)}{\beta(\alpha)} \int\limits_{\alpha_s(\nu)}^{\alpha} \frac{\mathrm{d}\alpha'}{\beta(\alpha')}\,, \qquad a_\Gamma(\nu,\mu) = -\int\limits_{\alpha_s(\nu)}^{\alpha_s(\mu)} \mathrm{d}\alpha\, \frac{\Gamma_{\text{cusp}}(\alpha)}{\beta(\alpha)} \tag{3.52}$$

and similarly for $a_{\gamma'}$, but with Γ_{cusp} replaced by the anomalous dimension of the hard function. In appendix A.2 there terms are expanded in terms of α_s up to NNLO.

The running of the shape function $\hat{S}$ is more complicated. When determining its scale evolution, we have to take into account an infinite number of operators instead of the finite basis, we employed in eq.(2.8). Thus the RGE for the shape function is written with an integral over all configurations of $\hat{\omega}'$, instead of a finite sum [20, 74, 75]

$$\frac{\mathrm{d}}{\mathrm{d}\ln\mu}\hat{S}(\hat{\omega},\mu) = \int\limits_0^\infty \mathrm{d}\hat{\omega}'\, \hat{\gamma}_S(\hat{\omega},\hat{\omega}',\mu)\hat{S}(\hat{\omega}',\mu)\,. \tag{3.53}$$

In this the anomalous dimension γ_S is not simply a matrix anymore, but a distribution, which has the general form [74]

$$\hat{\gamma}_S(\hat{\omega}',\hat{\omega},\mu) = -2\Gamma_{\text{cusp}}(\alpha_s)\left[\frac{1}{\hat{\omega}-\hat{\omega}'}\right]_* + 2\left(\gamma'(\alpha_s) - \gamma_J(\alpha_s)\right)\delta(\hat{\omega}-\hat{\omega}')\,. \tag{3.54}$$

Here we used the so–called star distribution, that will be defined in eq.(3.58) further

down below. Without going into the exact details of the derivation, we state the solution of the RGE for the shape function, that was derived in [20, 74, 75, 76]

$$\begin{aligned}\hat{S}(\hat{\omega},\mu_i) =& \exp\left[2\mathcal{S}(\mu_0,\mu_i) + 2a_{\gamma'}(\mu_0,\mu_i) - 2a_{\gamma_J}(\mu_0,\mu_i)\right] \\ &\times \frac{e^{-\gamma_E \eta}}{\Gamma(\eta)} \int_0^{\hat{\omega}} \mathrm{d}\hat{\omega}' \, \frac{\hat{S}(\hat{\omega}',\mu_0)}{\mu_0^{\eta}(\hat{\omega}-\hat{\omega}')^{1-\eta}} \,.\end{aligned} \tag{3.55}$$

Apart from the RG exponent, there is an additional dependence on the scale evolution in the parameter $\eta = 2a_\Gamma(\mu_0,\mu_i)$.

We can collect all the dependence on RG factors and anomalous dimensions from the above considerations into one factor $U_y(\mu_h,\mu_i,\mu_0)$, by using a relation between anomalous dimensions at different scales [77]

$$a_\Gamma(\mu_1,\mu_2) + a_\Gamma(\mu_2,\mu_3) = a_\Gamma(\mu_1,\mu_3) \,. \tag{3.56}$$

This way, all effects from the RG running (apart from the dependence on η) are bundled in one coefficient in the structure functions. It reads

$$\begin{aligned}U_y(\mu_h,\mu_i,\mu_0) \;=\; \exp\Bigg[&2\mathcal{S}(\mu_h,\mu_i) + 2\mathcal{S}(\mu_0,\mu_i) + 2a_{\gamma_J}(\mu_i,\mu_0) \\ &- 2a_{\gamma'}(\mu_h,\mu_0) - 2a_\Gamma(\mu_h,\mu_i)\ln\frac{m_b y}{\mu_h}\Bigg] \,.\end{aligned} \tag{3.57}$$

In the above, we need the RG factors as input. The cusp–anomalous dimension has been calculated to three [78] and four–loop accuracy [79]. The jet anomalous dimension γ_J is known up to three loops [77], as well as the the anomalous dimension of the SCET currents γ', which was determined to two– [80] and three–loop accuracy [81]. The expressions of the respective quantities can also be found in appendix A.2.

Finally we may write down the factorized form of the leading power structure function with the above considerations for the RG evolution. Note that the jet function as written in eq.(3.48) is a complicated distribution, as was shown for example in [20, 70]. To simplify the expression, it can be transformed it into Laplace space [70, 71], where it contains merely simple derivatives, acting on the scale parameter η appearing in a star distribution, which is defined as

$$\int_0^Q \mathrm{d}x \, \left[\frac{1}{x}\left(\frac{x}{a}\right)^\eta\right]_* f(x) = \int_0^Q \mathrm{d}x \, \frac{f(x)-f(0)}{x}\left(\frac{x}{a}\right)^\eta + \frac{f(0)}{\eta}\left(\frac{Q}{a}\right)^\eta \,. \tag{3.58}$$

This enables us to systematically include higher order perturbative corrections into the factorization formula, because every dependence on the RG parameter η is automatically generated to the order required. In addition only one integral over the star distribution needs to be determined, as all dependence on higher orders is contained in the Laplace transform $\tilde{j}$ of the jet function. The final factorized form of the leading power structure function reads

$$f_i^{(0)}(P_+, y) = U_y(\mu_h, \mu_i, \mu_0)\, H_{ui}(y, \mu_h)\, \widetilde{j}\left(\ln\frac{m_b\mu_0 y}{\mu_i^2} + \partial_\eta, \mu_i\right) \times \frac{e^{-\gamma_E \eta}}{\Gamma(\eta)} \int_0^{P_+} \mathrm{d}\hat{\omega} \left[\frac{1}{P_+ - \hat{\omega}}\left(\frac{P_+ - \hat{\omega}}{\mu_i}\right)^\eta\right]_* \hat{S}(\hat{\omega}, \mu_0)\ . \tag{3.59}$$

As written, this formula achieves a factorization of the perturbative contributions at the different scales and can in general be extended to an arbitrary order. Formally the results that are obtained with eq.(3.59) are independent of the scales μ_0, μ_i and μ_h, however a residual dependence remains from missing higher order terms. By varying the scales, we can estimate the size of the error this causes. We perform our analyses at NNLO, since both the perturbative corrections to the hard– and jet function, as well as the RG exponents are fully known to this order. For the actual calculations we then need to reexpand eq.(3.59) in terms of α_s. We assign the same power counting to the strong coupling at different scales and reexpand the final structure functions in them. The expansion for any terms $\sim \alpha_s(\mu_0)$ in the modelling of the shape function must be treated in a different way and we discuss the implications for it in chapter 6.3.

3.4 Mass schemes

In the previous section we established an expansion in the inverse quark mass, as well as in the strong coupling α_s for inclusive decays. Upon performing the phase space integration, it becomes apparent that the leading term in the expansion has a very strong dependence on the quark mass

$$\mathrm{d}\Gamma \sim G_F^2 |V_{\mathrm{CKM}}|^2 m_b^5\,, \tag{3.60}$$

which is expected since, without corrections in the inverse quark mass, the decay of the meson is simply the decay of its respective bound heavy quark. However in nature, quarks can never appear as free particles. They must always be confined in bound states

due to the phenomenon known as confinement. Therefore there is no unambiguous way to determine the mass of a quark, unlike for leptons (or other particles) that do appear as asymptotic states and hence can be measured experimentally. Consequently, any deviation in the value of the quark mass introduces a very large effect on the decay width, due to its enhancement by the fifth power.

In the following we want to show schematically how the choice of a suitable mass scheme can reduce the size of the perturbative corrections. We may derive relations between different mass schemes – in general their definition is related to the quark propagator

$$S(p) = \frac{-i}{\not{p} - m_0 + \Sigma(p, m_Q^{\text{scheme}})}\,, \tag{3.61}$$

with the bare mass m_0 and the self–energy Σ. Masses in different schemes are related to the bare mass m_0 by a perturbative series with divergent coefficients c_n that must be renormalized

$$m_0 = \left[1 + \sum_{n=1}^{\infty} c_n \left(\frac{\alpha_s}{\pi}\right)^n\right] m_Q^{\text{scheme}}\,. \tag{3.62}$$

Depending on the choice of the renormalization procedure, there are several distinct possibilities for the relation of the bare mass to the mass in a particular scheme. Since the quark mass is not directly experimentally accessible there is no unique choice – however one must make sure that all physical observables are unaffected by the scheme. For the on–shell (or pole) and the $\overline{\text{MS}}$ scheme the first coefficient can be determined [35]

$$\begin{aligned} c_1^{\text{OS}} &= -\frac{3}{4} C_F \left(\frac{1}{\varepsilon} + \gamma_E - 4\pi + \ln\frac{\mu^2}{\left(m_Q^{\text{OS}}\right)^2} + \frac{4}{3} + \mathcal{O}(\varepsilon)\right) \\ c_1^{\overline{\text{MS}}} &= -\frac{3}{4} C_F \left(\frac{1}{\varepsilon} + \gamma_E - 4\pi\right)\,. \end{aligned} \tag{3.63}$$

Note that the scale μ in the OS scheme is fixed by the on–shell condition, but the $\overline{\text{MS}}$ scheme stays scale dependent. Since both schemes can formally be defined by their perturbative series, it is possible to find a relation between the two

$$m_Q^{\text{OS}} = z^{\text{OS}\to\overline{\text{MS}}} m_Q^{\overline{\text{MS}}}\,, \tag{3.64}$$

in which the factor z is expressed in yet another perturbative series that can be written

as

$$z^{\mathrm{OS}\to\overline{\mathrm{MS}}} = 1 + \sum_{n=1}^{\infty} a_n \left(\frac{\alpha_s}{\pi}\right)^n \quad \text{and} \quad a_1 = -C_F \left(\frac{3}{4} \ln \frac{\mu^2}{\left(m_Q^{\mathrm{OS}}\right)^2} + 1\right) , \tag{3.65}$$

where all coefficients a_n are now finite after renormalization. Thus the choice of the mass scheme has direct impact on the perturbative series for observables. To make this explicit we write the differential rate from eq.(3.60) in the $\overline{\mathrm{MS}}$ scheme instead of the on–shell scheme

$$\mathrm{d}\Gamma \sim G_F^2 |V_{\mathrm{CKM}}|^2 \left(m_b^{\overline{\mathrm{MS}}}\right)^5 (z^{\mathrm{OS}\to\overline{\mathrm{MS}}})^5 \left(1 + \frac{\alpha_s}{\pi} r_1 + \left(\frac{\alpha_s}{\pi}\right)^2 r_2 + \dots\right) \tag{3.66}$$

$$= G_F^2 |V_{\mathrm{CKM}}|^2 \left(m_b^{\overline{\mathrm{MS}}}\right)^5 \left(1 + \frac{\alpha_s}{\pi}(r_1 + 5a_1) + \dots\right) , \tag{3.67}$$

where the dots denote higher order corrections in α_s. Thus we can conclude that by a suitable choice for the mass scheme, we may decrease the size of the perturbative corrections.

It was shown for example in [82, 83] that the on–shell scheme, which is often the natural choice for particles appearing as asymptotic states, is a particularly bad choice for quark masses . Computing observables in the on–shell scheme yields a badly behaved perturbative series. This is related to the fact that the on–shell mass m_Q^{OS} suffers from a so–called renormalon ambiguity [84, 85]. Using a short–distance mass scheme (such as e.g. $\overline{\mathrm{MS}}$) cures this problem since such schemes are by definition free of renormalons. Computing observables in a suitable short–distance scheme eventually yields a more rapidly converging perturbative series, which means in turn that the bad behaviour of the series in the on–shell scheme is related to the problem of renormalons in the on–shell mass.

In fact, the renormalon ambiguities cause an intrinsic uncertainty of $\mathcal{O}(\Lambda_{\mathrm{QCD}})$, which renders all predictions in higher orders of $1/m_b$ in HQET meaningless. The $\overline{\mathrm{MS}}$ scheme does not suffer from such renormalon issues, however still has a relatively bad convergence in the perturbative series for B meson observables [86, 87]. This is related to the fact that the $\overline{\mathrm{MS}}$ scheme is designed to work for scales $\mu > m_b$, while the scales in the Heavy Quark Expansion are typically $\mu < m_b$. For this reason specific mass schemes have been defined which we introduce in the next chapter.

3.4.1 Kinetic mass scheme

Due to the above considerations it becomes apparent that a mass scheme is needed specifically for the purpose of treating infrared contributions. One of such schemes is the kinetic mass scheme [88, 89]. The definition of the kinetic mass is based on the scheme independence of the meson mass m_H. By means of the Lagrangian from eq.(2.30) and the normalization from eq.(3.21) we can derive a systematic expansion for m_H in terms of the non–perturbative matrix elements introduced in the former section [34, 42, 89]

$$m_{\bar{H}} = m_Q + \bar{\Lambda} + \frac{\mu_\pi^2}{2m_Q} + \mathcal{O}\left(\frac{1}{m_Q^2}\right) , \tag{3.68}$$

where $m_{\bar{H}} = (m_H + 3m_{H^*})/4$ is the average mass of the ground state and excited meson H and H^*, respectively. The additional term $\bar{\Lambda}$ resembles the binding energy of the quark inside the meson and can be defined as $\bar{\Lambda} = m_B - m_b$ in the heavy quark limit. Because the l.h.s. of eq.(3.68) is an actually measurable quantity, the r.h.s. must necessarily be scheme independent [2]. This means, that for any specific choice of a mass scheme, all ambiguities in the mass definition must be compensated by a corresponding shift of the other parameters. It is worth mentioning that in higher orders, there appear non–local matrix elements in this formula [88], whose numerical values have not been determined experimentally yet.

All parameters in the kinetic scheme are connected to their counterparts in the OS scheme by means of a perturbative series, for example like $\bar{\Lambda}^{\rm OS} = \bar{\Lambda}^{\rm kin} + [\bar{\Lambda}]_{\rm pert}$. Here all α_s corrections are contained in $[\bar{\Lambda}]_{\rm pert}$. By considering eq.(3.68) in the kinetic as well as in the OS scheme, a relation between the two mass definitions can be derived [86]

$$m_Q^{\rm OS} = m_Q^{\rm kin}(\mu) + [\bar{\Lambda}(\mu)]_{\rm pert} + \frac{[\mu_\pi^2(\mu)]_{\rm pert}}{2m_Q^{\rm kin}(\mu)} + \mathcal{O}\left(\frac{1}{m_Q^2}\right) . \tag{3.69}$$

Here we explicitly denoted the scale μ, which serves as a Wilsonian cutoff $\Lambda_{\rm QCD} \ll \mu \ll m_Q$ which separates short– and long distance effects. As demonstrated in [86, 88], one can relate the perturbative corrections of the HQE parameters to the QCD sum rules in the small–velocity limit, i.e. in the limit where the three–momentum of

[2] Of course this statement is only true, when one considers eq.(3.68) to all orders in $1/m_b$. By employing a cutoff, uncertainties from the choice of the mass scheme might reappear.

the final state is much smaller than m_b and m_c in the rest frame of the B meson.

The perturbative corrections to the mass, as well as the HQE parameters are currently known at NNLO [90] and N^{3}LO [86] – their respective expressions are given in appendix A.3 for completeness. Knowing the conversion between schemes to this order in α_s is necessary, as the corrections to the partonic rates are known to the same accuracy.

Chapter 4

CP Violation in three–body B decays

We investigate the violation of CP symmetry in multibody B decays. As discussed in chapter 1.3 a difference in the strong as well as in the weak phase is necessary to have non–vanishing CP violation in the SM. While the latter is given in terms of the CKM matrix, the strong phase is often challenging to compute and a full QCD–based theoretical description is missing for most processes of interest.

In the last decades large amounts of data became available on B decays from BaBar, Belle(II) and LHCb. For charmless nonleptonic two–body decays the method of QCD factorization (QCDF) [91, 92, 93, 94] has been established, which is set up as a double expansion in α_s and $\Lambda_{\rm QCD}/m_b$.

A large part of nonleptonic B decays are however three– and more–body decays. They come with the added benefit that the strong phases and therefore also the CP asymmetries depend on one of the kinematical variables such that they differ across phase space. First attempts to use QCDF to calculate decay rates and CP asymmetries show that the leading order can reproduce the gross features for the Dalitz distributions, but does not seem to describe the corresponding CP asymmetries properly [95, 96].

Consequently, the current description of multibody B decays relies to a large extent on modelling of the corresponding decay amplitudes (see e.g. [97, 98, 99, 100, 101, 102, 103, 104]). In this chapter we introduce a new parameterization for such decays by dividing the amplitude into $\mathcal{A}_u$ and $\mathcal{A}_c$, which contain valence u and c quarks, respectively. This allows us to extend the usual amplitude analysis with charmonium loops at high invariant masses, which may be governed by charm resonances or even charmonium–like exotic states. Unlike the usual resonance description, this generates large CP effects, that we discuss using several scenarios for intermediate states [13].

4.1 Modelling the three–body amplitudes

In this chapter we focus on the process $B^+(p_B) \to \pi^+(p_1)\pi^-(p_2)\pi^+(p_3)$, however the approach can also be extended to $B \to hhh$ with $h = \pi, K$ decays. In the SM, the decay is described by the weak effective Hamiltonian for the $b \to d$ flavour transition eq.(2.19). For the sake of modelling the amplitudes, we are only interested in the difference of operators containing u quarks and c quarks. Therefore we use eq.(1.21) to eliminate the CKM element $V_{tb}V_{td}^*$ and rewrite the Hamiltonian as

$$\mathcal{H}_{\text{eff}} = \frac{G_F}{\sqrt{2}} \left(V_{ub}V_{ud}^* \, \mathcal{O}_u + V_{cb}V_{cd}^* \, \mathcal{O}_c \right) , \tag{4.1}$$

where $\mathcal{O}_{u,c}$ contain the current–current as well as the relevant penguin operators. Explicitly employing the convention that the CP–violating weak phase of the CKM matrix enters via $V_{ub} = |V_{ub}|e^{-i\gamma}$, the decay amplitude can be written as

$$\mathcal{A}_\pm(s_{12}, s_{23}) \coloneqq \langle B^\pm | \mathcal{H}_{\text{eff}} | \pi\pi\pi \rangle = \mathcal{A}_u(s_{12}, s_{23}) \, e^{\mp i\gamma} + \mathcal{A}_c(s_{12}, s_{23}) \tag{4.2}$$

with

$$\mathcal{A}_q(s_{12}, s_{23}) = \frac{G_F}{\sqrt{2}} |V_{qb}V_{qd}^*| \langle B | \mathcal{O}_q | \pi\pi\pi \rangle \, . \tag{4.3}$$

The amplitudes $\mathcal{A}_\pm$ and $\mathcal{A}_u$ contain CP–conserving strong phases and are complex valued functions of the kinematic variables s_{12} and s_{23}, which are defined as

$$s_{ij} \coloneqq m_{ij}^2 = (p_i + p_j)^2 \, . \tag{4.4}$$

Direct CP violation is induced by the interference of the matrix elements of the two operators $\mathcal{O}_u$ and $\mathcal{O}_c$, analogously to the general case from eq.(1.27).

The matrix elements $\mathcal{A}_q$ are non–perturbative and therefore their values have to be extracted from data by means of an amplitude analysis. In general, $\mathcal{A}_+$ and $\mathcal{A}_-$ are fitted separately using a model ansatz. Frequently used are isobar models, which parameterize the three–body amplitudes as pseudo two–particle decays, where one of the two particles is a resonance that subsequently decays into two stable particles [14]. Schematically this reads

$$\mathcal{A}_\pm(s_{12}, s_{23}) = \sum_k \frac{c_k^\pm P_k^{(\ell)}(s_{12}, s_{23})}{s_{12} - m_k^2 + i m_k \Gamma_k} + \sum_l \frac{c_l^\pm P_l^{(\ell)}(s_{12}, s_{23})}{s_{23} - m_l^2 + i m_l \Gamma_l} \, . \tag{4.5}$$

Here $P^{(\ell)}$ are the Legendre polynomials describing the spin of the decaying resonances with masses m and widths Γ. In the simplest isobar model the propagators of the decaying resonances are described by Breit–Wigner shapes. More sophisticated approaches make use of Blatt–Weisskopf factors [105] to account for different spin configurations or employ the so called K–matrix approach [106], which preserves unitarity in contrast to the Breit–Wigner model. However all of these approaches contain the complex parameters $c_k^{\pm}$ which are assumed to be constant throughout the Dalitz distribution, such that all the kinematic dependence arises from the Breit–Wigner form. Therefore the strong phases extracted from the differential rates depend strongly on the underlying shape of the these models. In addition there is no possibility to include non–resonant effects in the analysis, which pose a valid source of CP violation.

As the weak CKM phase γ is constant throughout the Dalitz plane, the CP distribution gives a direct measure of the strong phase differences between the amplitudes $\mathcal{A}_u$ and $\mathcal{A}_c$. This difference is driven by the mass of the charm quark. If the charm and up–quark mass would be equal, the CP asymmetry would vanish, since then $\mathcal{A}_u$ and $\mathcal{A}_c$ would be identical.

In the isobar model, the kinematical dependence of the phases in $\mathcal{A}_u$ and $\mathcal{A}_c$ arises from the Breit–Wigner shapes and is related to the asymptotic final–state interactions of the decay products of the resonance. These asymptotic interactions are not related to CP violation, which is evident since both interfering amplitudes will have the same Breit–Wigner phase. Therefore, the fact that the thresholds for charm states are fundamentally different from light quark states will manifest itself in the CP asymmetry close the charm thresholds. Such effects would contribute to $\mathcal{A}_c$, while they would be absent (or strongly suppressed) in $\mathcal{A}_u$. Interestingly, the distribution of CP violation for $B \to \pi\pi\pi$ obtained by the LHCb Collaboration [14, 15, 16] shows pronounced structures in the center of the Dalitz plane close to the invariant mass of $c\bar{c}$ states.

Therefore, parameterizing the amplitudes in terms of $\mathcal{A}_u$ and $\mathcal{A}_c$ is the natural choice in which the known mechanisms of CP violation in the SM are incorporated. It is thus advantageous to perform the analysis using not the amplitudes $\mathcal{A}_+$ and $\mathcal{A}_-$, but rather $\mathcal{A}_u$ and $\mathcal{A}_c$. Specifically this implies

$$\mathcal{A}_{\pm}(s_{12}, s_{23}) = \sum_k \frac{(a_k^{(u)} e^{\mp i\gamma} + a_k^{(c)}) P_k^{(\ell)}(s_{12}, s_{23})}{s_{12} - m_k^2 + i m_k \Gamma_k} + \sum_l \frac{(b_l^{(u)} e^{\mp i\gamma} + b_l^{(c)}) P_l^{(\ell)}(s_{12}, s_{23})}{s_{23} - m_l^2 + i m_l \Gamma_l}\,, \tag{4.6}$$

with the same set of complex fit parameters $a^{(u)}$ and $a^{(c)}$ for both amplitudes. In

addition, the benefit of a set up using $\mathcal{A}_u$ and $\mathcal{A}_c$ is, that charm effects which are expected to play a dominant role above the open–charm threshold can be included systematically. We discuss the inclusion of these threshold effects in the next section.

We note that the isobar–model parameterization has a few interesting features. First of all, in the case of very narrow resonances (meaning that their width is small compared to the mass spacing between the different resonances) the relation in eq.(4.6) implies

$$\frac{\mathrm{d}^2\Gamma_\pm}{\mathrm{d}s_{12}\,\mathrm{d}s_{23}} = \sum_k \delta(s_{12}-m_k^2)P_k^{(\ell)}(m_k^2,s_{23})\mathcal{B}(B^\pm\to\pi R_k)\,, \tag{4.7}$$

where

$$\mathcal{B}(B^\pm\to\pi R_k) = \frac{1}{\Gamma_{\mathrm{tot}}}\left|a_k^{(u)}e^{\mp i\gamma}+a_k^{(c)}\right|^2\,, \tag{4.8}$$

is the branching ratio of the two–body decay $B\to\pi R_k$. In this approximation, the rate asymmetry is completely determined by those of the two particle decays. Therefore, if only low lying resonances with masses well below the charm threshold are taken into account, the narrow width example clearly shows how the complex structure in the CP asymmetries at high invariant masses can hardly be accounted for.

A second remark needs to be made concerning the current fits of the data. In the most recent analysis of the LHCb Collaboration [14, 15] the residues of the resonances are parameterized as

$$c_k^\pm = a_k^{(u)}e^{\mp i\gamma}+a_k^{(c)} = x_k\pm\delta x_k + i(y_k\pm\delta y_k)\,, \tag{4.9}$$

with real parameters $x_k, y_k, \delta x_k, \delta y_k$ and where $a^{(q)} = |a^{(q)}|e^{i\phi^{(q)}}$. This shows that the two parameterizations are related and contain the same information. However we emphasize, that when using $x, y, \delta x, \delta y$, the assignment to the matrix elements appearing in the effective Hamiltonian is not evident anymore. In practice, the fit values are extracted with respect to the ρ resonance [14, 15]. This means that y_ρ and δy_ρ are fixed to 0 corresponding to a phase choice, because the overall phase of amplitude $\mathcal{A}_\pm$ is not observable. For our parameterization this implies that $\phi_\rho^{(u)} = 90°$. In addition for the isobar fit, x_ρ is fixed to 1, so the values of $x, y, \delta x, \delta y$ for other resonances are in units of the value for the ρ resonance. The relative strength of the

two matrix elements $\mathcal{A}_u$ and $\mathcal{A}_c$ is then given by

$$\frac{|a_\rho^{(u)}|}{|a_\rho^{(c)}|} \simeq \delta x_\rho \simeq \mathcal{O}(10^{-3})\,, \tag{4.10}$$

where the numerical factor can be obtained by using the fit result for δx_ρ from [15]. The smallness of the ratio seems to indicate that the amplitude for the ρ resonance is driven by $\mathcal{A}_c$. This seems counter–intuitive as the ρ can be immediately formed from the valence u quarks in $\mathcal{A}_u$. Therefore, we expect the ratio in eq.(4.10) to be much larger. The small ratio may very well be an artefact of the analysis as charmed resonances are not included. In fact, rewriting the fit parameters $x, y, \delta x, \delta y$ from [15] for the S–wave resonance σ and the D–wave resonance f_2 also leads to a small ratio $a^{(u)}/a^{(c)}$. This indicates that charmed resonances and threshold effects might play a role.

4.2 Parameterization of threshold effects

We now want to turn our attention to the parameterization of the charm threshold effects and include them into the isobar fit. In addition we study whether this extension to current fit models changes the ratio in eq.(4.10) to more plausible values.

To parameterize the impact of the open–charm threshold effects, we concentrate on the current–current part of the operator $\mathcal{O}_c$. We insert a full set of intermediate states $1 = \sum |n\rangle\langle n|$ to write it as

$$\langle B^+|\mathcal{O}_c|\pi\pi\pi\rangle = \sum_n \langle B^+|\mathcal{O}_c|n\rangle\,\langle n|\pi\pi\pi\rangle\,. \tag{4.11}$$

The sum over these intermediate states can be split into the states with and without valence charm quarks. We assume that the difference between the matrix elements of the operators $\mathcal{O}_c$ and $\mathcal{O}_u$ is mainly driven by the states involving valence charm quarks and hence focus on them. We naively factorize the matrix element $\langle B^+|\mathcal{O}_c|n\rangle$, by employing a Fierz identitiy on the four–quark operator

$$\langle\mathcal{O}_c\rangle = \frac{1}{N_c}\langle\bar{b}\gamma_\mu(1-\gamma_5)d\rangle\langle\bar{c}\gamma_\mu(1-\gamma_5)c\rangle + \langle\bar{b}\gamma_\mu T^a(1-\gamma_5)d\rangle\langle\bar{c}\gamma_\mu T^a(1-\gamma_5)c\rangle\,. \tag{4.12}$$

The invariant mass of the intermediate states $|n\rangle$ must be close to the B meson mass, and therefore the lowest possible (hadronic) state with valence charm quarks is a $c\bar{c}$ resonance $R_{c\bar{c}}$ and a pion. At leading order in the Fock state, the $c\bar{c}$ reso-

nance is in a color singlet state, thus only the first term in eq.(4.12), which is $1/N_c$ suppressed, contributes. Furthermore, the $c\bar{c}$ resonance $R_{c\bar{c}}$ is in a V − A isopin–zero state. The (axial)–vector current generates a tower of J/ψ (1^{--}) (and orbitally excited charmonium) resonances which decay into two pions, but only with small branching ratios [26]. Thus it is reasonable to assume that they do not mark the most significant contributions in the process.

The color–allowed second term in eq.(4.12) produces the two charm quarks in a color–octet state. Its leading hadronic contribution arises through intermediate states containing a $D^{(*)}\bar{D}^{(*)}$ pair. A similar picture emerges in QCD factorization of two body decays, where the charm loop drives the CP asymmetry. This is sketched in Fig. 4.1, where the cut shows that the $D\bar{D}$ states can appear as intermediate states. In two–body decays, the loop momentum q has $q^2 = m_B^2$ and therefore this contribution is subleading in $1/m_b$. However, in three–body decays such $D\bar{D}$ intermediate states can rescatter into two pions which leads to a threshold behaviour once the invariant mass of the two pions crosses the value $2m_D$. In general, the amplitude $\mathcal{A}_c$ will thus contain – aside from Breit–Wigner like contributions as modelled in the isobar model – also threshold-like singularities

$$\mathcal{A}_c = \langle B^+|\mathcal{O}_c|R_{c\bar{c}}\pi\rangle \langle R_{c\bar{c}}\pi|\pi\pi\pi\rangle + \langle B^+|\mathcal{O}_c|D\bar{D}X\rangle \langle D\bar{D}X|\pi\pi\pi\rangle \,, \tag{4.13}$$

where for simplicity we only consider the $D\bar{D}$ threshold. We denote the intermediate $D\bar{D}X$–state by R, where R contains the $c\bar{c}$ pair in a color-octet configuration. The second term in eq.(4.13) is challenging to calculate, even if one constructs a mesonic model based on heavy–meson chiral perturbation theory. The diagrams encountered in this approach can in general become divergent whenever orbitally excited D^* mesons appear in the loop–induced decay [97]. In order to render the diagrams finite it is

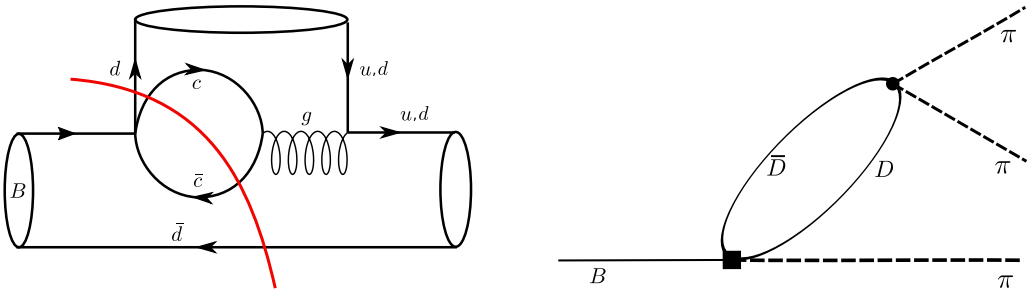

Figure 4.1: Left: Sketch of color–octet contribution in QCD factorization, where the blobs correspond a single or two-pion states. Right: example of a mesonic diagram corresponding to the one on the left.

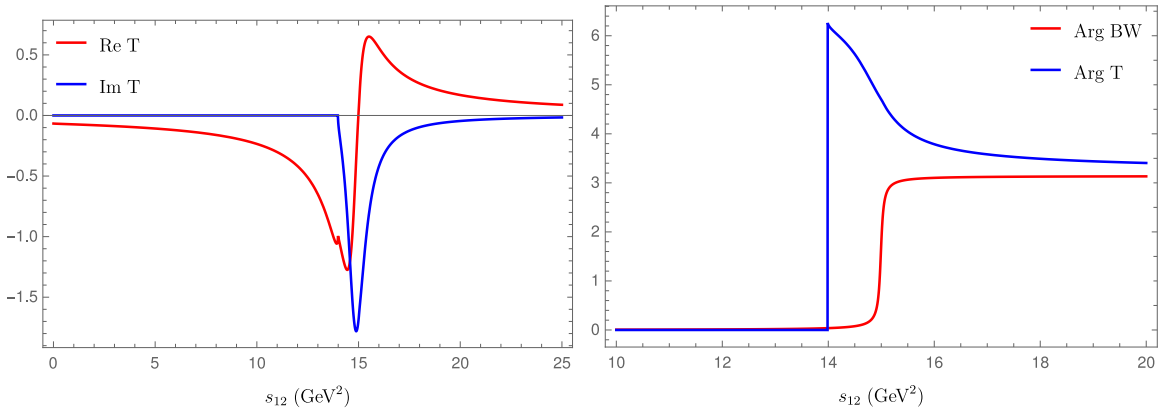

Figure 4.2: Left: Real and imaginary parts of the modified propagator T_R below and above the open–charm threshold. Right: Comparison of the argument of T_R and a standard Breit–Wigner shape.

necessary to introduce a formfactor that regulates the diagram [99, 100]. Since this also poses a model assumption there is no advantage in actually constructing such diagrams – the number of parameters that must be determined by experiment does not decrease this way. The same problem applies to a dispersive treatment, where additional subtraction constants need to be introduced, that limit the predictive power of the approach in the same way. Because of these issues, we propose a simple model ansatz for the threshold contributions. While this procedure does not contain more parameters that need fixing with experimental data than more sophisticated approaches, it is much easier to extend existing Dalitz analyses with it.

The intermediate state R can be described with a modified propagator corresponding to a two–point function of a quantum field

$$T_R(s_{12}) = \frac{1}{s_{12} - (m_R^{\text{bare}})^2 + \Sigma(s_{12})} = \frac{1}{s_{12} - m_R^2 + [\Sigma_R(s_{12}) - \text{Re}\,\Sigma_R(m_R^2)]}\,, \qquad (4.14)$$

where $\Sigma_R(s_{12})$ is the self energy of the state R. To ensure that the pole is located at the physical mass m_R, the bare mass is renormalized by Re $\Sigma_R(m_R^2)$[1]. Here we focus on the contributions from the open–charm loops to the self–energy, which entail the standard bubble summation diagrams. The underlying assumption of this parameterization is the fact, that the self energy of the resonance decaying into two pions may be represented by this particular threshold contribution. These loops generate a dynamical width for the resonance above the open–charm threshold, which we parameterize by

[1] We do not explicitly consider the field renormalization, as these terms would only alter the residue of the propagator which is a model parameter.

the threshold function

$$\Sigma_R(s_{12}) = g_R m_R \sqrt{s_{\text{thres}} - s_{12}} \arctan\left(\frac{1}{\sqrt{\frac{s_{\text{thres}}}{s_{12}} - 1 + i\epsilon}}\right) , \tag{4.15}$$

where s_{thres} is the open-charm threshold and g_R is the coupling of the intermediate state R to an open–charm system. Note that the threshold function acquires an imaginary part, once its threshold is crossed, while the real part has a cusp there. Figure 4.2 depicts the real and imaginary part of T_R below and above the open–charm threshold, and a comparison between the argument of T_R and a standard Breit–Wigner shape. This shows that the strong phase introduced from the threshold is fundamentally different from that in a standard Breit–Wigner parameterization. The sharp sign change at the $D\bar{D}$ threshold was also found in [103, 104], which shows how this parameterization shares features with an approach using mesonic loop–diagrams. As a consequence, our parameterization generates much larger structures in the CP distribution. We note that in principle the coupling g_R can be fixed once the width of R is determined from experiment. In addition also effects of composite states could be described by eq.(4.15).

Finally, the threshold effects described by T_R are accounted for via

$$\mathcal{A}_c(s_{12}, s_{23}) = \sum_R a_R e^{i\phi_R} \left(P_R^{(\ell)}(s_{12}, s_{23}) T_R(s_{12}) + (s_{12} \leftrightarrow s_{23}) \right) + \dots , \tag{4.16}$$

where a_R and ϕ_R are constant normalization constants and phases, and the dots indicate low–lying resonances that can be parameterized in the usual way. In principle, m_R, g_R, a_R and ϕ_R are fit parameters that should be determined from the amplitude analysis.

Furthermore known exotic charmonium resonances can also be explicitly included with this parameterization. For example $X(3872)$ or $Z_c(3900)$, which decay predominantly into a pair of open–charm states (like $D\bar{D}$, $D\bar{D}^*$, ...) and lie very close to their respective thresholds. Finally, we emphasize that these $D\bar{D}$ threshold effects may be even more pronounced in $B \to KKK$ or $B \to K\pi\pi$ decays. The above discussion can be similarly applied to these decays and our model ansatz for $\mathcal{A}_c$ in eq.(4.16) can directly be applied to these analyses as well.

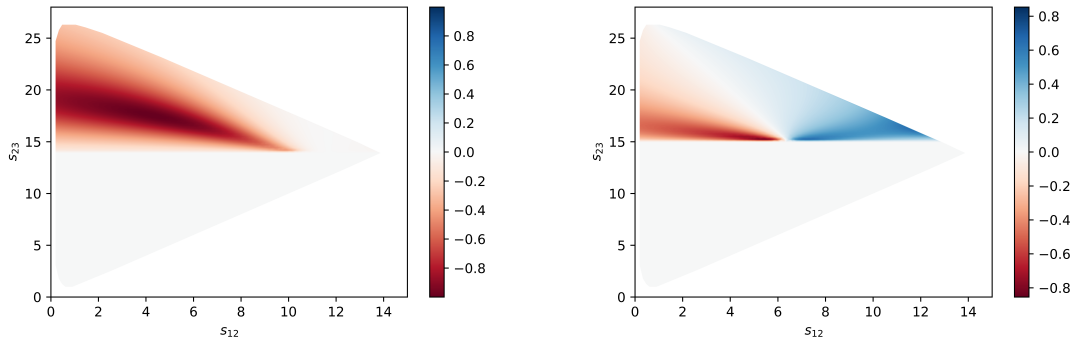

Figure 4.3: CP distributions from the resummed propagator T_R. Left: the S–wave resonance $\chi_{c0}(3860)$. Right: the P–wave resonance $X(3872)$.

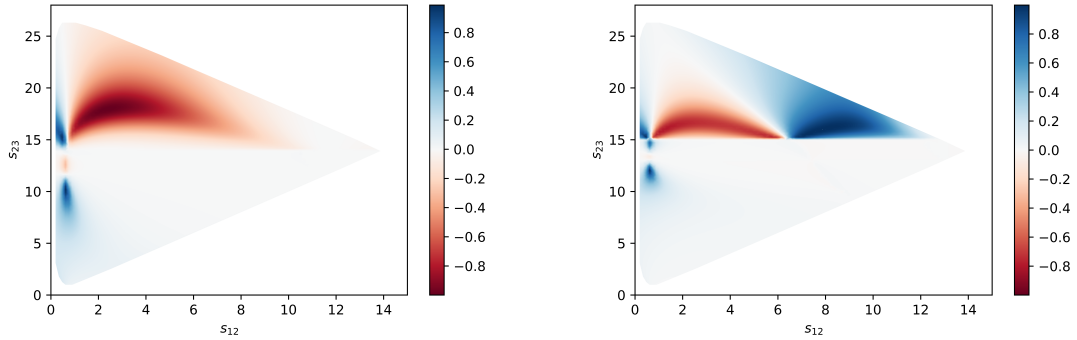

Figure 4.4: CP distributions from interference of a ρ resonances and the resummed propagator T_R. Left: the S–wave resonance $\chi_{c0}(3860)$. Right: the P–wave resonance $X(3872)$.

4.3 Discussion and conclusion

The model ansatz for the threshold effects, that we presented in this chapter, should be tested in a full analysis of the $B \to hhh$ data to see if the CP asymmetries in the high–energy region can be described. As discussed, it would be particularly interesting to see, if the fit results for the lower–lying resonances change, such that they are more in line with the expectation of a dominating $\mathcal{A}_c$ contribution. Furthermore it would be interesting to see how these effects influence an $B \to KKK$ amplitude analysis.

A full analysis of the experimental data cannot be obtained in this thesis, because it requires the inclusion of the lower–lying resonances and specific S and D wave parameterizations that the LHCb Collaboration uses (see [14, 15] for a recent elaborate study). These are unfortunately only implicitly denoted in the respective publications, such that an extraction of their explicit model is very cumbersome. Nevertheless we

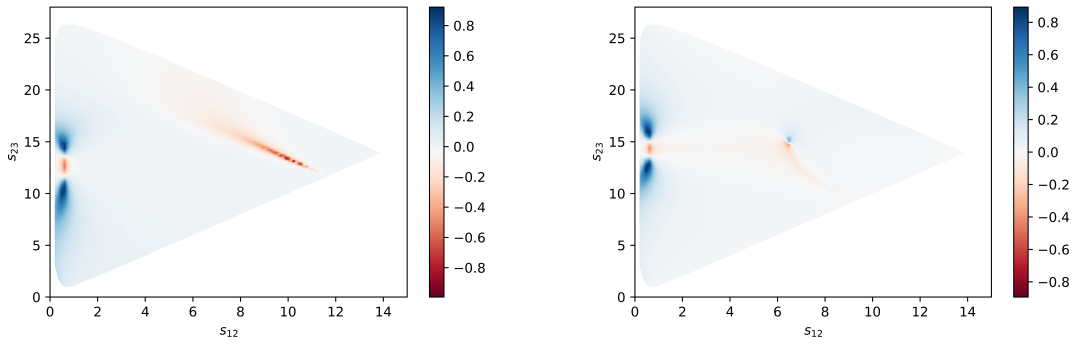

Figure 4.5: CP distributions from the interference of a ρ resonances and Breit–Wigner parameterizations. Left: the S–wave resonance $\chi_{c0}(3860)$. Right: the P–wave resonance $X(3872)$.

illustrate that the sharp change in the strong phase, due to the opening of the $D\overline{D}$ threshold, can generate interesting CP patterns. For this we discuss four exemplary studies.

In figure 4.3 we show the effect of T_R in the high–s region with the assumption that $\mathcal{A}_u$ is constant and considering the effect of one resonance in $\mathcal{A}_c$. To emphasize the difference between S and P–wave contributions, we consider the scalar $\chi_{c0}(3860)$ and the vector $X(3872)$ described by the resummed propagator T_R. There the relevant charmonium thresholds are $D\bar{D}$ and $D\bar{D}^*$, respectively. We emphasize that these states are just examples to illustrate the effect of T_R. In fact, our parameterization is not limited to these known resonances and can be applied more generally by leaving the parameters m_R and g_R unconstrained in the analysis. For the purpose of these examples, we fixed m_R to the value of the respective resonance and assumed $g_R = 0.1$. We observe that the inclusion of the charm–loops, causes large patterns of CP violation of $\mathcal{O}(1)$ above the open–charm threshold. Similarly large effects were found in the recent analysis of [104], where a model based on hadronic charm loops combined with a χ_c^0 resonance is discussed.

Of course, the assumption of $\mathcal{A}_u$ poses a large simplification, as in a full fit this amplitude contains a series of low–lying resonances (correspondingly also $\mathcal{A}_c$ can contain such resonances). To illustrate the effect that the interference of these resonances with $\mathcal{A}_c$ has, we include a ρ resonance, parameterized with a Breit–Wigner shape in the amplitude $\mathcal{A}_u$. In figure 4.4 we show the corresponding CP distributions again for both the scalar $\chi_{c0}(3860)$ and the vector $X(3872)$ resonance described by the resummed propagator T_R. Even in parameterizing $\mathcal{A}_u$ in such a simplistic way, we observe a wide

variety of CP violation in different regions of the Dalitz as the model generates $\mathcal{O}(1)$ CP violation in the high–energy region. To stress the difference of our model with a standard Breit–Wigner parameterization, we generate in figure 4.5 the corresponding plots using Breit–Wigner parameterizations for the ρ as well as the χ_c and X resonance. Because these resonances are very narrow, CP violation is only observed in their very close vicinity. This is particularly contrasted by the center region of the Dalitz distribution, where such a parameterization cannot create any structures at all.

We see that the model ansatz, which includes effects from open–charm threshold states, can indeed cause intricate structures with $\mathcal{O}(1)$ CP violation. Moreover, we conclude that it is feasible to perform the amplitude analysis in terms of the amplitudes $\mathcal{A}_u$ and $\mathcal{A}_c$, instead of $\mathcal{A}_+$ and $\mathcal{A}_-$. This allows to better distinguish effects from different physical sources and directly probe the strong phases, which drive the strength of CP violation. From the experimental point of view it will become relevant to include open–charm effects and exotic states in one way or the other, once data becomes more precise. The framework established here is an easy to implement possibility to do that. Thus, employing this model ansatz into a full amplitude analysis, may give valuable insights and help improve the theoretical description of multibody decays.

Chapter 5

First extraction of inclusive V_{cb} from q^2 moments

In this chapter, we want to turn our attention to the inclusive determination of the CKM element V_{cb} from $B \to X_c \ell \nu$ decays. As mentioned before, V_{cb} is present in several different processes such that enhancing its precision is a key component even beyond the decays considered here. Furthermore, improving our knowledge of V_{cb} is important given the longstanding tension between V_{cb} obtained from exclusive $B \to D^{(*)} \ell \nu$ decays and the inclusive result, known as the V_{cb} puzzle (for recent works see e.g. [107, 108]). In some observables (like $B_s \to \mu^+ \mu^-$), the uncertainty on V_{cb} is already the dominating contribution to the full error. Beyond that, also the extraction of HQE parameters from the process is important, as they form an input in, for example, the SM prediction for inclusive $B \to X_{s,d} \ell\ell$ decays [109, 110].

The determination of V_{cb} has reached an impressive percent–level of accuracy due to both experimental and theoretical progress (see e.g. [111] for a recent review). As we explained in chapter 3.1 and 3.2.1, inclusive determinations are based on the Heavy-Quark Expansion, allowing for an OPE of the differential semileptonic rate as a power expansion in the inverse bottom quark mass, $1/m_b$. We want to tackle the problem of proliferations that appears at $\mathcal{O}(1/m_b^4)$ for the non–perturbative matrix elements and use a new method utilizing q^2 moments to determine an updated value for V_{cb}.

All previous inclusive extractions of V_{cb} use centralized moments of the lepton energy and hadronic invariant mass decay spectra that are normalized and do not depend on V_{cb}. These moments allow for the extraction of the non–perturbative hadronic matrix elements, which are in turn used in combination with the total semileptonic rate to determine V_{cb}.

The current most precise determination employs the kinetic scheme for the b quark

mass, outlined in [112] (see also [113, 114]):

$$|V_{cb}| = (42.16 \pm 0.30|_{\text{th}} \pm 0.32|_{\text{exp}} \pm 0.25|_{\Gamma}) \cdot 10^{-3} = (42.16 \pm 0.51) \cdot 10^{-3} \ . \qquad (5.1)$$

This state–of–the–art determination includes the recently calculated α_s^3 corrections to the total rate [115] and power corrections up to $1/m_b^3$. At this level, only the four hadronic parameters are present, that we introduced in eq.(3.22, 3.23): μ_π^2 and μ_G^2 at order $1/m_b^2$, and ρ_{LS}^3 and ρ_D^3 at $1/m_b^3$. Computing the expansion at even higher orders, the number of hadronic matrix elements increases rapidly with an additional nine elements at $1/m_b^4$ and eighteen at $1/m_b^5$ [37, 38, 116]. This proliferation of HQE elements hinders their full extraction from data. On the other hand, using the lowest–lying state saturation (LLSA) assumption [38, 117], the size of the $1/m_b^4$ and $1/m_b^5$ parameters can at least be estimated. Using these estimates as Gaussian priors, the $1/m_b^4$ and $1/m_b^5$ parameters were included in an analysis of the inclusive semileptonic $b \to c$ data [40, 112]. The inclusion of the higher power corrections mentioned above, is found to reduce the value of V_{cb} by about 0.25% [40]. In addition, a recent analysis using the 1S–scheme provided a value for V_{cb} consistent with (5.1), but exhibiting a slightly larger uncertainty [118].

In this chapter, we use the methods described in chapter 3.2.2 to perform the first determination of V_{cb} using the approach suggested in [41] based on the moments of the four–momentum transfer q^2 spectrum. These moments have recently been measured experimentally with high precision by both Belle [17] and Belle II [18]. Furthermore they are reparameterization invariant quantities and thus we may significantly reduce the number of HQE parameters, that are necessary up to $\mathcal{O}(1/m_b^4)$ – see eq.(3.31).

This chapter is outlined as follows. We first summarize the method to determine V_{cb} from q^2 moments and discuss the available α_s corrections. In chapter 5.2, we discuss the fit procedure as well as the inputs and the treatment of the theoretical uncertainties. We continue discussing our results for several scenarios for the theoretical correlations.

All of the results in this chapter were published in [19].

5.1 The new method to determine $\mathbf{V_{cb}}$

5.1.1 Preliminaries

We consider the semileptonic decay of a B meson $B(p_B) \to X_c(p_X)\ell(p_\ell)\nu_\ell(p_\nu)$, with $\ell = e, \mu$, triggered by the effective Hamiltonian from eq.(3.3), with a transition into a charm quark:

$$\mathcal{H}_{\text{eff}} = \frac{G_F}{\sqrt{2}} V_{cb} \left(\bar{c}b\right)_{\text{V}-\text{A}} \left(\bar{\ell}\nu\right)_{\text{V}-\text{A}} + \text{h.c.}\,. \tag{5.2}$$

In order to include the spectral moments $\langle M^k \rangle$ of the inclusive decay, we generalize the phase space integration over the total semileptonic rate Γ_{sl} in eq.(3.7) by multiplying with a certain weight function $w(v, p_\ell, p_\nu)$, raised to an integer power n

$$\langle M^n[w] \rangle = \int \text{d}\Phi \, w^n(v, p_\ell, p_\nu) \, W^{\mu\nu} L_{\mu\nu} \,. \tag{5.3}$$

Here $v = p_B/m_B$ is the B meson velocity and p_ν and p_ℓ denote the momenta of the neutrino and the charged–lepton, respectively. The prediction for Γ_{sl} is obtained with $w(v, p_\ell, p_\nu) = 1$, while moments of the leptonic invariant mass (q^2 moments) correspond to the weight function $w(v, p_\ell, p_\nu) = q^2$, where $q = p_\ell + p_\nu$ is the momentum of the lepton pair. In this prescription it is also simple to generate other spectral moments. For example, for the hadronic invariant mass moments, one sets $w(v, p_\ell, p_\nu) = (m_B v - q)^2$ with $p_X = p_B - q$, while moments of the charged lepton energy in the B meson rest frame are obtained with $w(v, p_\ell, p_\nu) = v \cdot p_\ell$.

The calculation of the total semileptonic rate proceeds via the OPE of the time–ordered product of the hadronic tensor, yielding the HQE we derived in chapter 3.2.1. Just like for the total rate, we may utilize this method to determine an expansion in inverse m_b for the spectral moments as well

$$\langle M^n[w] \rangle = \sum_{n=0}^{\infty} \frac{C^{(n)}_{\mu_1 \ldots \mu_n}}{m_b^{n+3}} \langle B | \bar{b}_v (iD^{\mu_1} \cdots iD^{\mu_n}) b_v | B \rangle \,, \tag{5.4}$$

where we explicitly denoted the suppression in the heavy quark mass.

The total rate and the q^2 moments are invariant under the reparameterization transformation δ_{RP} that we introduced in eq.(3.27). This can easily be seen, when applying

the transformation to the generalized moments from eq.(5.3)

$$\delta_{\mathrm{RP}}\langle M^n[w]\rangle = \int \mathrm{d}\Phi\,[\delta_{\mathrm{RP}} w^n(v,p_\ell,p_\nu)]\,W^{\mu\nu}L_{\mu\nu}\,. \tag{5.5}$$

Note that the RP transformation only acts on the weight function on the r.h.s. here, because it is the only quantity which can be velocity dependent. Obviously the weights of the rate and the q^2 moments do not depend on v and thus they are fundamentally RPI. On the contrary, the hadronic invariant mass and charged–lepton energy moments are not invariant under reparameterization, since their associated weight functions $\delta_{\mathrm{RP}} w(v,p_\ell,p_\nu) \neq 0$. In [41, 48] it was shown that the invariance under reparameterization of the total rate and the q^2 moments, which implies $\delta_{\mathrm{RP}}\Gamma_{\mathrm{sl}} = 0$ and $\delta_{\mathrm{RP}}\langle (q^2)^n\rangle = 0$, holds also for their corresponding OPE and connects subsequent orders in $1/m_b$ in eq.(5.4). As we have shown in chapter 3.2.2, we can exploit this fact to reduce the number of parameters that need to be determined by experiment significantly from thirteen to eight at $\mathcal{O}(1/m_b^4)$ – see eq.(3.31) for the definition of the RPI matrix elements.

The spectral moments are measured at B factories with various threshold selections on the charged–lepton energy. On the one hand these selections are necessary to suppress backgrounds from low–energy electrons. On the other hand, measurements with different selections provide additional information on the HQE parameters. Predictions for the moments with threshold selections on the charged–lepton energy are obtained by including a proper veto function in the weight, e.g. $w(v,p_\ell,p_\nu) \to w(v,p_\ell,p_\nu)\theta(v\cdot p_\ell - E_{\mathrm{cut}})$. However, introducing a similar phase–space constraint in the q^2 moments breaks their invariance under reparameterization. Therefore it was suggested in [41] to study q^2 moments with a threshold selection directly on q^2, which then preserves the RPI of the observable. Note that the constraint on the minimum value of q^2 also implies a bound on the charged–lepton energy, because $q^2 \leq 4E_\ell E_\nu$. In particular we see

$$E_\ell \geq \frac{m_B^2 + q^2_{\mathrm{cut}} - m_D^2 - \lambda^{1/2}(m_B^2, q^2_{\mathrm{cut}}, m_D^2)}{2m_D}\,, \tag{5.6}$$

where $\lambda^{1/2}(m_B^2, q^2_{\mathrm{cut}}, m_D^2)$ is the Källén function. The q^2 threshold selection cannot be chosen too large, since a value at high q^2 would significantly reduce the available phase space and render the decay no longer sufficiently inclusive, as pointed out in [41].

5.1.2 Spectral q^2 moments in the HQE

In accordance with eq.(5.3), we may write the moments of the q^2 spectrum with a threshold selection by

$$\mathcal{Q}_n(q^2_{\rm cut}) \coloneqq \frac{1}{\Gamma_0}\int \mathrm{d}\Phi\,(q^2)^n\,\theta(q^2-q^2_{\rm cut})\,W^{\mu\nu}L_{\mu\nu} = \frac{1}{\Gamma_0}\int\limits_{q^2_{\rm cut}}^{m_b^2(1-\sqrt{\rho})^2}\mathrm{d}q^2\,(q^2)^n\,\frac{\mathrm{d}\Gamma}{\mathrm{d}q^2}\,, \tag{5.7}$$

where $\Gamma_0 = G_F^2 m_b^5 |V_{cb}|^2 A_{\rm ew}/(192\pi^3)$ and $\rho = m_c^2/m_b^2$. In addition the factor

$$A_{\rm ew} = (1+\frac{\alpha}{\pi}\log(M_Z/m_b))^2 \simeq 1.01435 \tag{5.8}$$

accounts for short–distance radiative corrections at the electroweak scale [119]. We define the normalized moments of the spectrum in the following way

$$\left\langle (q^2)^n \right\rangle_{q^2\geq q^2_{\rm cut}} \coloneqq \int\limits_{q^2_{\rm cut}}^{m_b^2(1-\sqrt{\rho})^2}\mathrm{d}q^2\,(q^2)^n\,\frac{\mathrm{d}\Gamma}{\mathrm{d}q^2}\Bigg/\int\limits_{q^2_{\rm cut}}^{m_b^2(1-\sqrt{\rho})^2}\mathrm{d}q^2\,\frac{\mathrm{d}\Gamma}{\mathrm{d}q^2} = \frac{\mathcal{Q}_n(q^2_{\rm cut})}{\mathcal{Q}_0(q^2_{\rm cut})}\,. \tag{5.9}$$

Furthermore we can define the central moments of the q^2 spectrum, because they can in general be measured more precisely

$$\begin{aligned} q_1(q^2_{\rm cut}) &\coloneqq \left\langle q^2 \right\rangle_{q^2\geq q^2_{\rm cut}} \text{ for } n=1\,,\\ q_n(q^2_{\rm cut}) &\coloneqq \left\langle (q^2-\left\langle q^2\right\rangle)^n \right\rangle_{q^2\geq q^2_{\rm cut}} \text{ for } n>1\,. \end{aligned} \tag{5.10}$$

These moments are related to the normalized ones from eq.(5.9) via the binomial formula

$$\left\langle (q^2-a)^n \right\rangle = \sum_{i=0}^{n}\binom{n}{i}\left\langle (q^2)^i\right\rangle (-a)^{n-i}\,. \tag{5.11}$$

In the HQE, the moments are expressed as a double expansion in α_s and $1/m_b$; equivalently to the differential rate that was schematically shown in eq.(3.24) and (3.25)

$$\begin{aligned}\mathcal{Q}_n(q^2_{\text{cut}}) = (m_b^2)^n \Bigg\{ & \mu_3 \left[X_0^{(n)} + \left(\frac{\alpha_s}{\pi}\right) X_1^{(n)} + \dots \right] \\ & + \frac{\mu_G^2}{m_b^2}\left[g_0^{(n)} + \left(\frac{\alpha_s}{\pi}\right) g_1^{(n)} + \dots \right] + \frac{\rho_D^3}{m_b^3}\left[d_0^{(n)} + \left(\frac{\alpha_s}{\pi}\right) d_1^{(n)} + \dots \right] \\ & + \frac{r_E^4}{m_b^4} l_{r_E}^{(n)} + \frac{r_G^4}{m_b^4} l_{r_G}^{(n)} + \frac{s_B^4}{m_b^4} l_{s_B}^{(n)} + \frac{s_E^4}{m_b^4} l_{s_E}^{(n)} + \frac{s_{qB}^4}{m_b^4} l_{s_{qB}}^{(n)} \Bigg\}, \end{aligned} \tag{5.12}$$

where the strong coupling constant $\alpha_s \equiv \alpha_s^{(4)}(\mu_s)$ is evaluated at the renormalization scale μ_s. The overall factor of $(m_b^2)^n$ is introduced to ensure that the various functions appearing in eq.(5.12) are dimensionless.

The tree–level expressions up to $\mathcal{O}(1/m_b^4)$ of $\mathcal{Q}_n(q^2_{\text{cut}})$, with $n = 0, \dots, 4$ are computed and listed in [41]. The q^2 spectrum in the free–quark approximation was calculated at NLO several times [120, 121, 122], while NNLO corrections are currently not known. The calculations in [87, 123, 124] focus solely on the hadronic invariant mass and charged–lepton energy moments, such that their results are not applicable to the analysis at hand. NLO corrections to the power suppressed terms of order $1/m_b^2$ are computed in [125, 126, 127], while the corrections at $\mathcal{O}(1/m_b^3)$ were presented just recently [128].

The total rate Γ_{sl} within the HQE was introduced schematically in eq.(3.24). To leading order in the HQE, perturbative QCD corrections are computed to NLO [129], NNLO [123, 130, 131, 132] and recently at N^{3}LO [115] (results for the Abelian colour factors are also confirmed in [133]). At orders $1/m_b^2$ and $1/m_b^3$ the NLO corrections are computed in [128, 134], while for higher orders they are currently not known.

5.1.3 NLO corrections to the q^2 moments

There are basically two sources of $\mathcal{O}(\alpha_s)$ corrections to the differential q^2 rate. On the one hand there are what we call 'genuine' corrections, which are the NLO corrections to the Wilson coefficients that were discussed before. On the other hand the change to a suitable mass scheme introduces further corrections of $\mathcal{O}(\alpha_s)$, as we saw in chapter 3.4 in detail. The genuine NLO corrections were first derived in [120], utilizing the on–shell (or pole) renormalization scheme for the charm and bottom mass. These corrections

Γ	tree	α_s	α_s^2	α_s^3
Partonic	✓	✓	✓	✓
μ_G^2	✓	✓		
ρ_D^3	✓	✓		
$1/m_b^4$	✓			
$m_b^{\text{kin}}/m_c^{\overline{\text{MS}}}$		✓	✓	✓

$\langle (q^2)^n \rangle$	tree	α_s	α_s^2	α_s^3
Partonic	✓	✓		
μ_G^2	✓	✓		
ρ_D^3	✓	✓		
$1/m_b^4$	✓			

Table 5.1: Schematic overview of the perturbative corrections available for the partial rate Γ and the q^2 moments. Green checkmarks denote corrections that are known and built into our code. Red checkmarks indicate corrections that are in general known, but currently not part of our package. For references and further information we refer to the text.

correspond to $X_1^{(n)}$ in eq.(5.12)) and they are given by

$$X_1^{(n)} = \frac{1}{(m_b^2)^n \Gamma_0} \int\limits_{q^2_{\text{cut}}}^{m_b^2(1-\sqrt{\rho})^2} \mathrm{d}q^2 \, (q^2)^n \, \frac{\mathrm{d}\Gamma^{(1)}}{\mathrm{d}q^2} \,, \tag{5.13}$$

where the explicit expression for $\mathrm{d}\Gamma^{(1)}/\mathrm{d}q^2$ has been derived in [120] (see also [128]). Reexpanding the q^2 moments in eq.(5.9) in α_s, gives the explicit dependence on $\mathcal{O}(\alpha_s)$ terms for the normalized q^2 moments

$$\langle (q^2)^n \rangle \Big|_{\alpha_s} = \frac{\alpha_s}{\pi} \frac{1}{\left(X_0^{(0)}\right)^2} \left(X_0^{(0)} X_1^{(n)} - X_0^{(n)} X_1^{(0)} \right) . \tag{5.14}$$

Equivalently we can obtain the genuine $\mathcal{O}(\alpha_s)$ corrections for the centralized moments in terms of the non–normalized q^2 moments from eq.(5.9).

The expressions in the on–shell scheme are affected by a renormalon ambiguity, leading to a badly behaved perturbative series, as we discussed in chapter 3.4. To avoid this, the heavy quark masses are converted from the on–shell scheme to a short–distance scheme. For the determinations in this chapter we adopt the kinetic scheme (see chapter 3.4.1) for the bottom quark mass, while for the charm mass we use the $\overline{\text{MS}}$ scheme. Since the mass relations are known to N^{3}LO [86] we can consistently apply the conversion between different mass schemes to the computations in this chapter.

In the kinetic scheme, the HQE parameters are also redefined by subtracting the

respective perturbative correction – for the parameters at hand this means particularly

$$\begin{aligned}\mu_\pi^2(0) &= \mu_\pi^2(\mu) - [\mu_\pi^2(\mu)]_{\text{pert}}\,,\\ \mu_G^2(0) &= \mu_G^2(\mu) - [\mu_G^2(\mu)]_{\text{pert}}\,,\\ \rho_D^3(0) &= \rho_D^3(\mu) - [\rho_D^3(\mu)]_{\text{pert}}\,,\end{aligned} \tag{5.15}$$

where the HQE parameter at $\mu = 0$ denotes the pole scheme. In our analysis, we thus extract the values of the kinetic scheme HQE parameters.

The conversion of the bottom (charm) mass to kinetic ($\overline{\text{MS}}$) scheme is performed after reexpanding the expressions for the centralized q^2 moments in the on–shell scheme up to $\mathcal{O}(\alpha_s)$. In that way, the mass scheme redefinitions yield additional α_s corrections besides the genuine α_s corrections described before. Note that it is only possible to consistently use corrections from both sources, if they are included to the same order.

In figure 5.1 we show the theoretical predictions for the partonic part of the first four centralized moments, including both genuine and scheme change α_s corrections. The ratio between the LO and NLO prediction is shown in the lower panel of each plot. Note that for consistency, we neglected all terms $\sim \alpha_s \times$ HQET parameters (i.e. corrections of $\mathcal{O}(\alpha_s/m_b^2)$), since we have not included the genuine α_s corrections to these parameters for the q^2 moments. The shaded area in the ratios represents the uncertainty obtained by varying the scale of μ_s in the range $m_b^{\text{kin}}/2 < \mu_s < 2m_b^{\text{kin}}$. We observe that for larger cuts in q^2 the NLO corrections become more important for the second to fourth moments.

In the software package developed for the calculation of inclusive V_{cb} as described above, all genuine α_s corrections as well as all corrections associated with the scheme conversion are implemented [11]. The integrals appearing in eq.(5.13) are solved numerically with fixed order gaussian quadrature. Furthermore, we implement the charm mass m_c in both the kinetic and $\overline{\text{MS}}$ scheme, allowing for the current, most precise value to be used as input. For the bottom mass m_b we fix the choice of the mass scheme to be kinetic. We finally point out that it is easily possible to extend this package to even higher order corrections, once they become available. In table 5.1, we present an overview of the perturbative corrections available and those included in the current version. Very recently, also the α_s corrections to ρ_D^3 for the moments have become available [135]. These will be implemented in an updated version of the code.

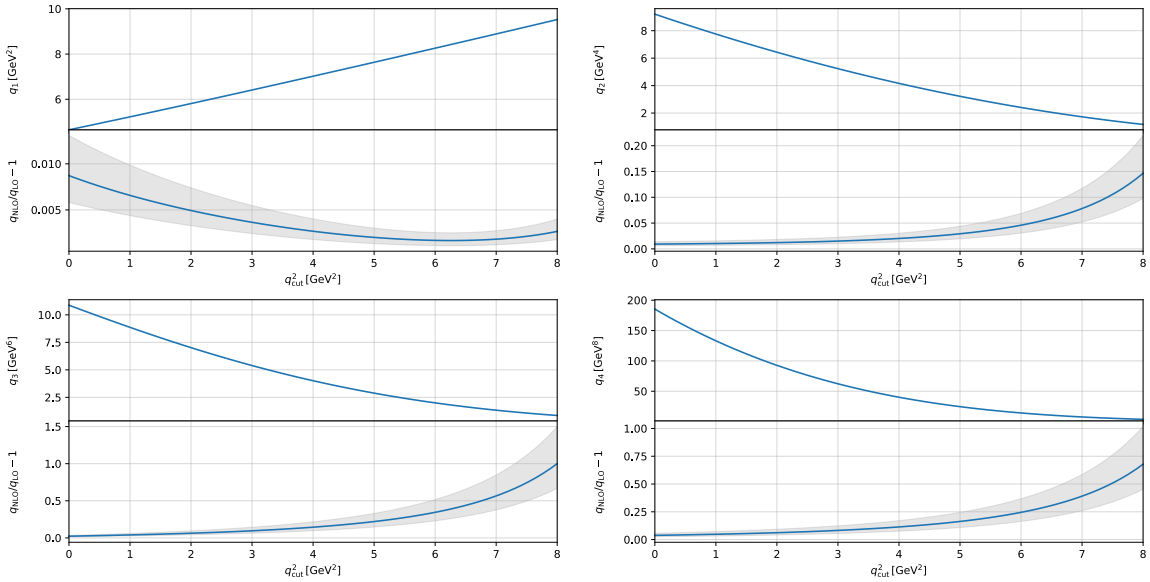

Figure 5.1: The first to fourth order centralized q^2 moments and their NLO/LO ratio for the perturbative α_s contributions. Note that the NLO part in the ratio is depicted without the leading order contribution. The grey area represents the uncertainty due to variations of the scale μ.

5.1.4 Dependence on μ_3 and μ_π^2

It is worth emphasizing that eq.(5.12) is not explicitly dependent on the HQE parameter μ_π^2. Due to RPI, the Wilson coefficient of $\mu_\pi^2/(2m_b^2)$ is always equal to the one of the free quark decay μ_3 which was defined in terms of its HQE matrix element in eq.(3.31a). Both parameters have a direct correspondence, shown in eq.(3.32). This means that there is a direct connection between μ_3 and μ_π^2 in the HQE after employing RPI. Due to the normalization of the q^2 moments in eq.(5.9) there is no sensitivity in the fit for μ_3 and the dependence on μ_π^2 becomes effectively of order $1/m_b^4$, once the ratio in eq.(5.9) is reexpanded in $1/m_b$.

This can be seen explicitly in the normalized moments

$$\begin{aligned}\frac{\mathcal{Q}_n(q^2_{\text{cut}})}{\mathcal{Q}_0(q^2_{\text{cut}})} &= \frac{\mu_3 X_0^{(n)} + \frac{\mu_G^2}{m_b^2}\, g_0^{(n)} + \mathcal{O}\left(\frac{1}{m_b^3}\right)}{\mu_3 X_0^{(0)} + \frac{\mu_G^2}{m_b^2}\, g_0^{(0)} + \mathcal{O}\left(\frac{1}{m_b^3}\right)} \\ &= \frac{X_0^{(n)}}{X_0^{(0)}}\left[1 + \frac{\mu_G^2}{m_b^2}\left(\frac{g_0^{(n)}}{X_0^{(n)}} - \frac{g_0^{(0)}}{X_0^{(0)}}\right) - \frac{(\mu_G^2)^2}{m_b^4}\left(\frac{1}{2} + \frac{g_0^{(0)}}{X_0^{(0)}}\right)\left(\frac{g_0^{(n)}}{X_0^{(n)}} - \frac{g_0^{(0)}}{X_0^{(0)}}\right)\right. \\ &\qquad \left. + \frac{\mu_\pi^2 \mu_G^2}{2m_b^4}\left(\frac{g_0^{(n)}}{X_0^{(n)}} - \frac{g_0^{(0)}}{X_0^{(0)}}\right)\right], \end{aligned} \tag{5.16}$$

where we neglected all terms at order $1/m_b^3$ for easier readability in the last line. Consequently, the moments are, in fact, insensitive to μ_π^2, while μ_3 is an important input for the total rate and thus the V_{cb} determination. At the moment, we circumvent this problem by using an external constraint on μ_π^2, as discussed in more detail in chapter 5.2.2. For this reason our code contains the parameter μ_π^2 instead of μ_3.

5.1.5 Dependence on $1/m_b^4$ parameters

The exploitation of RPI enables us to extract the reduced set of HQE parameters up to $\mathcal{O}(1/m_b^4)$ consistently from data. However we observe that not all parameters are equally sensitive to the q^2 moments at this order. In figure 5.2 we show the sensitivity of the first to fourth central q^2 moments to the $1/m_b^4$ matrix elements by individually varying them between $\pm 1\,\text{GeV}^4$. The largest variation is observed for r_G and r_E, while there is only limited sensitivity to s_E, s_B, and s_{qB}. We also note that different orders of moments exhibit different differential dependencies as a function of the q^2 threshold. In other words, the simultaneous analysis of different orders should allow us – similar to the existing inclusive V_{cb} hadronic and leptonic moment fits – to separate parameter contributions from each other. In figure 5.3 we illustrate the impact of different choices for the subleading terms on the value of V_{cb} by varying them individually between $\pm 1.5\,\text{GeV}^4$. In the following, we include r_E^4 and r_G^4, along with ρ_D^3, μ_G^2 and μ_π^2 in our fits, as we expect very little sensitivity to the other $1/m_b^4$ parameters. In turn, the precise value of the other parameters will only have a small impact on the description of the moments and, due to their subleading contributions to the total rate, on V_{cb}. Since the measured experimental information from Belle and Belle II do not provide partial branching fractions of $B \to X_c \ell \bar{\nu}_\ell$ with q^2 cuts, the extraction of V_{cb} will rely on the total branching fraction as an input. We discuss this issue in chapter 5.2.4.

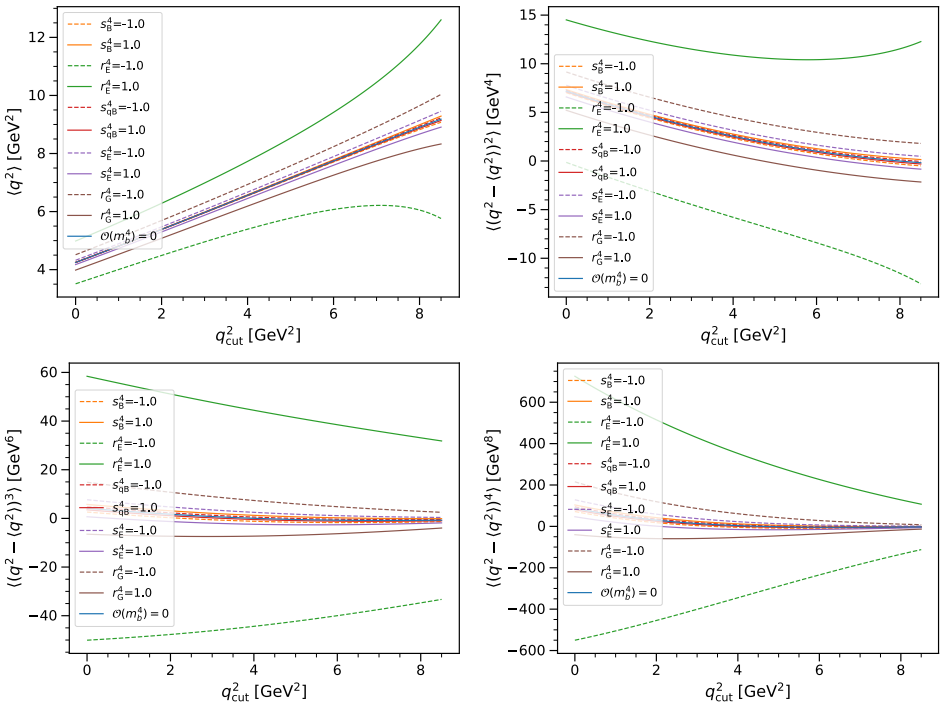

Figure 5.2: Sensitivity of the central q^2 moments for individual contributions of $1/m_b^4$ HQE terms, obtained by varying their values between $\pm 1\,\text{GeV}^4$. We observe that the strongest dependence is coming from the parameters r_E and r_G, while the others have almost no effect.

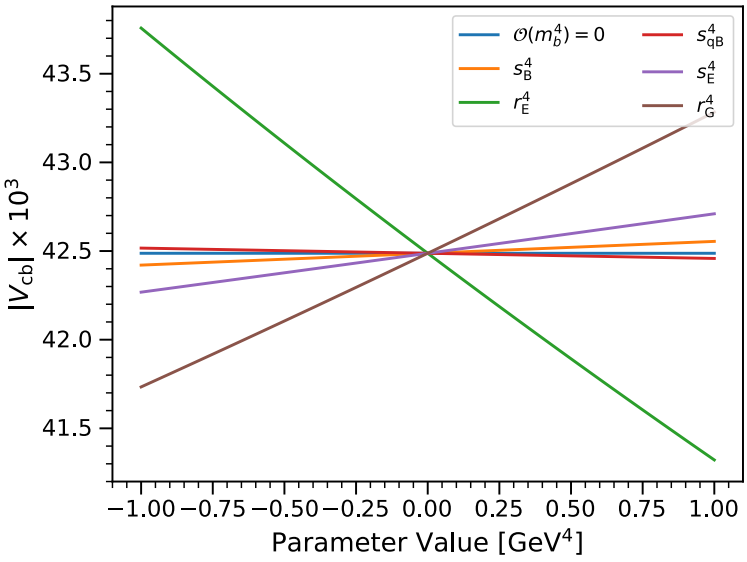

Figure 5.3: Illustration of the variation of $|V_{\text{cb}}| \times 10^3$ as a function of $\mathcal{O}(1/m_b^4)$ HQE terms.

5.2 The fit procedure using Belle (II) data

Having defined the q^2 moments with the perturbative corrections that are included in our default fit, the extraction of V_{cb} can straightforwardly be approached. The normalized or centralized q^2 moments with different threshold selections q^2_{cut}, defined in (5.9) and (5.10), combined with the measured total rate (without lepton energy cut), can now be used to extract the reduced set of HQE parameters. As mentioned, this includes only eight parameters up to $\mathcal{O}(1/m_b^4)$, instead of the thirteen that are necessary when using non–RPI observables and hence the level of proliferation is significantly reduced. The recently measured q^2 moments from Belle and Belle II, allow us to obtain $|V_{cb}|$ using this alternative method for the first time. Furthermore we can determine the $1/m_b^4$ HQE parameters from the datasets and investigate the effect of correlations between the different moments for different threshold selections.

5.2.1 Fit setup

The HQE parameters and $|V_{cb}|$ are determined in a simultaneous χ^2 fit, that takes into account both experimental and theoretical correlations. The full χ^2 function reads

$$\begin{aligned}\chi^2(|V_{cb}|,\vec{\theta}) =& \frac{\left(\mathcal{B} - \frac{\tau_B}{\hbar}\,\Gamma(|V_{cb}|,\vec{\theta})\right)^2}{\sigma_{\mathcal{B}}^2 + \sigma_{\Gamma}^2} \\ &+ \left(\vec{q}(\vec{\theta}) - \vec{q}_{\text{meas}}\right) C^{-1} \left(\vec{q}(\vec{\theta}) - \vec{q}_{\text{meas}}\right)^T \\ &+ \sum_{i=1}^{4} \frac{\left(\theta_i - \theta_i^{\text{cons}}\right)^2}{\sigma_{\theta_i}^2}\,, \end{aligned} \tag{5.17}$$

where $\mathcal{B}$ is the experimental branching ratio for $B \to X_c \ell \nu$ and Γ the theoretical prediction for the rate introduced above. In addition $\vec{q}$ denotes the theoretical expressions for the different q_n moments at different cuts, while $\vec{q}_{\text{meas}}$ are the corresponding measured moments. In addition, we use the B meson life time $\tau_B = (1.579 \pm 0.004)$ ps [26] and define $\vec{\theta} = \left\{m_b^{\text{kin}}, \overline{m}_c, \mu_G^2, \mu_\pi^2\right\}$ for the constrained fit parameters, which we further discuss in chapter 5.2.2. Furthermore we include external constraints to the parameters as discussed in the next section whenever possible. Finally, $C = C_{\text{stat}} + C_{\text{syst}} + C_{\text{theo}}$ denotes the sum of the statistic, systematic and theory covariance matrix respectively.

The statistical and systematical covariance matrices are obtained directly from the Belle and Belle II data. The theoretical covariance matrix however is less straightforward to determine. As we discuss in chapter 5.2.3, we include an estimate for missing

higher–order contributions for which the correlation between different q^2 moments is unknown. In addition, a single moment q_i at different values of q^2_{cut} is expected to be highly correlated. We therefore introduce two separate correlation parameters ρ_{cut} and ρ_{mom}. The first parameterizes the correlation between two moments of the same order but with different q^2 threshold selections

$$\rho\left(q_n(q^2_{\text{cut,A}}), q_n(q^2_{\text{cut,B}})\right) \equiv \rho^x_{\text{cut}} \quad \text{and} \quad x = \frac{\left|q^2_{\text{cut,B}} - q^2_{\text{cut,A}}\right|}{0.5\,\text{GeV}^2}\,, \tag{5.18}$$

meaning that we consider two observables at consecutive cuts to be more strongly correlated than those with larger separation. This way of parameterizing the correlation was inspired by the detailed study performed in [114].

For moments of different order and different q^2 cuts, the correlation parameter ρ_{mom} is constructed as

$$\rho\left(q_m(q^2_{\text{cut,A}}), q_n(q^2_{\text{cut,B}})\right) = \text{sign}(\rho_{\text{mom}}) \cdot |\rho_{\text{mom}}|^{|m-n|} \cdot \rho\left(q_n(q^2_{\text{cut,A}}), q_n(q^2_{\text{cut,B}})\right)\,, \tag{5.19}$$

which results in a decrease of correlations for moments of different order. The size of the parameter ρ_{mom} is the percentual change in correlation and it increases if orders are further apart. Note that both correlation scenarios impair each other, i.e. moments of different order and at different cuts are influenced by both parameters and thus are less strongly correlated than moments that are closer together in either the order or cut. In order to minimize the effect of choosing a specific value for the correlation parameters ρ_{cut} and ρ_{mom}, we include the correlation as nuisance parameters into the fit. These parameters are constrained using a flat prior, built from a double Fermi–Dirac function

$$f_{\text{DFD}}(\rho, a, b) = \frac{1}{2(1+e^{w(\rho-b)})(1+e^{-w(\rho-a)})}\,, \qquad b > a\,, \tag{5.20}$$

with $w = 50$. The parameters a and b denote the lower and upper boundaries for ρ, respectively. We constrain ρ_{cut} between 0 and 1, while ρ_{mom} is allowed to take negative values with a lower boundary of -0.45. These constraints for ρ_{cut} and ρ_{mom} are included in the χ^2 function as additional terms like

$$\chi^2 \mapsto \chi^2 + \chi^2_{\text{DF}} = \chi^2 - 2\ln f_{\text{DFD}}(\rho_{\text{cut}}, 0, 1) - 2\ln f_{\text{DFD}}(\rho_{\text{mom}}, -0.45, 1)\,. \tag{5.21}$$

5.2.2 External constraints to the fit

The fit parameters $\vec{\theta}$ that we previously discussed, can be constrained by external inputs. Most importantly, as discussed in detail in [114], only a linear combination of m_b and m_c is constrained by the fit. Therefore it is beneficial to employ external constraints on these parameters, as otherwise they are not easy to fix. For our default fit we work in the kinetic mass scheme for m_b. Taking the values in the $\overline{\text{MS}}$ scheme that were obtained in lattice calculations $\overline{m}_b(\overline{m}_b) = 4.198(12)\,\text{GeV}$ and $\overline{m}_c(3\,\text{GeV}) = 0.988(7)\,\text{GeV}$ [136], we find for the bottom quark mass in the kinetic scheme

$$m_b^{\text{kin}}(1\,\text{GeV}) = 4.565 \pm 0.015 \pm 0.013\,\text{GeV} = 4.565 \pm 0.020\,\text{GeV}\,, \tag{5.22}$$

where the first error is the theoretical uncertainty coming from the scheme conversion [86] and the second stems from the $\overline{m}_b(\overline{m}_b)$ error. In addition, we use the charm quark mass m_c in the $\overline{\text{MS}}$ scheme, for which precise determinations exist from lattice [136] and QCD sum rules [137, 138]. This way, we ensure to use the strongest possible constraints on the value of m_c in the fit. Using `RunDec` with four–loop accuracy, we obtain

$$\overline{m}_c(2\,\text{GeV}) = 1.093 \pm 0.008\,\text{GeV}\ . \tag{5.23}$$

We implement the above considerations on the masses as Gaussian constraints in our default fit. Moreover, we may place a constraint on μ_G^2. Using the mass difference between the vector meson B^* and the ground state B, we find

$$m_{B^*} - m_B = \frac{2}{3}\frac{\mu_G^2}{m_b} + \mathcal{O}(\alpha_s\mu_G^2, 1/m_b^3)\,. \tag{5.24}$$

Note that our convention for the definition of the HQE parameters uses the rephased QCD fields (see the explanations in chapter 3.2.1), while the mass difference above is defined in the infinite mass limit of HQET. In general the difference between the two approaches introduces corrections in the higher orders of the relation, which are non–local and currently unknown. However for the purpose of finding a constraint on μ_G this issue can be neglected and thus we find

$$\mu_G^2 = (0.362 \pm 0.07)\ \text{GeV}^2\,, \tag{5.25}$$

which is implemented as a Gaussian constraint in our default fit as well. Finally, as discussed in chapter 5.1.4, we have a limited sensitivity to μ_π^2. Therefore we add a rather loose Gaussian constraint on μ_π^2 for the analysis

$$\mu_\pi^2 = (0.432 \pm 0.24)\,\mathrm{GeV}^2\,, \tag{5.26}$$

which we obtain by using the value that was computed in [40] and inflating the uncertainty by a factor of approximately four. It then agrees with $\mu_\pi^2 = 0.477 \pm 0.056\,\mathrm{GeV}^2$, found in the most recent V_{cb} analysis [112]. The need to put a constraint (even though loose) on μ_π^2 is somewhat of a downside to our approach. However, we stress that in future analyses, it may become possible to extract the parameter μ_3 directly with other non–perturbative methods (see discussion in [41]). In addition, progress on the lattice (see [139, 140]) may also give additional insights into the HQE parameters and thus sharpen the constraints further.

5.2.3 Theoretical uncertainties and correlations

In order to generate the theoretical uncertainties to the nominal and centralized q^2 moments, we use m_b and m_c as given in eq.(5.22) and eq.(5.23) as inputs, respectively. As a default for the strong coupling, we use

$$\alpha_s(m_b^{\mathrm{kin}}) = 0.2184\,, \tag{5.27}$$

which was obtained using `RunDec` [141, 142] with $n_f = 4$ active flavours and five loop accuracy, as well as the initial value of $\alpha_s^{(5)}(M_Z) = 0.1179(9)$ [26].

We account for three types of theoretical uncertainties due to missing higher–order terms:

- For missing higher–order corrections in α_s, we vary the scale of $\alpha_s(\mu_s)$ between $m_b^{\mathrm{kin}}/2 < \mu_s < 2m_b^{\mathrm{kin}}$.
- For missing higher–order $1/m_b^5$ corrections, we vary the contribution of ρ_D^3 by 30%.
- For missing $\alpha_s/m_b^{2,3}$ corrections, we vary the contribution of μ_G^2 by 20%.

Note that for the power corrections, these variations were inspired by the uncertainties implemented in [113, 114]. Since this was the first determination of V_{cb} and the HQE elements using the q^2 method, we use these variations as a conservative estimate. In

future determinations with possible α_s/m_b^2 corrections included, these variations may be reduced. Finally, we do not include uncertainties on the input values of m_b or m_c. As these inputs are very precisely known, they would not contribute to the theory uncertainty in any substantial way.

In order to estimate the theory uncertainties, we need default values for the HQE parameters μ_G^2 and ρ_D^3, which we take from the analyses in [40]

$$\mu_G^2 = 0.362\,\text{GeV}^2, \quad \rho_D^3 = 0.127\,\text{GeV}^3\,. \tag{5.28}$$

Contributions from the $1/m_b^4$ terms are currently not varied, because their corrections are already accounted for in the variation of ρ_D^3.

5.2.4 Experimental input

The $B \to X_c \ell \bar{\nu}_\ell$ branching fraction

Knowledge of the branching ratio of $B \to X_c \ell \bar{\nu}_\ell$ is instrumental to determine $|V_{cb}|$. The current measurements of this branching ratio either quote partial branching fractions as a function of the lepton energy cut, or provide the full $B \to X \ell \bar{\nu}_\ell$ rate. Also in the latter case, the total rate is measured with a cut on the lepton energy and then extrapolated to the full phase space. Unlike in the fits of [112, 114], we cannot directly make use of the partial branching fraction results, since a lepton energy cut spoils RPI. We therefore need to use the total branching fraction. Currently only a small number of results are available that quote the total branching fraction and thus we also extrapolate partial branching fractions with a cut on the lepton energy $\mathcal{B}_{\text{cut}}$ to the full phase space. This is done with a correction factor $\Delta(E_{\text{cut}})$, such that

$$\mathcal{B}(B \to X_c \ell \bar{\nu}_\ell) = \Delta(E_{\text{cut}}) \mathcal{B}_{\text{cut}}(B \to X_c \ell \bar{\nu}_\ell)\,. \tag{5.29}$$

The factor $\Delta(E_{\text{cut}})$ can be calculated reliably in the local OPE. Using the partial branching rate at leading order in the HQE and including perturbative corrections up to NLO, we find

$$\Delta(0.6\,\text{GeV}) = 1.047 \pm 0.004\,, \qquad \Delta(0.4\,\text{GeV}) = 1.014 \pm 0.001\,. \tag{5.30}$$

The quoted uncertainty is obtained by including the power corrections up to $1/m_b^3$ and evaluated with the values obtained in [112]. Additional uncertainties due to the variation of the renormalization scale μ_s are negligible. We note that, as expected, this

correction factor is rather insensitive to power corrections, due to the small extrapolation region.

In table 5.2, we list the available measurements for $B \to X\ell\bar{\nu}_\ell$ and $B \to X_c\ell\bar{\nu}_\ell$ branching fractions and quote the extrapolations to the full phase space. We correct the branching fractions of $B \to X\ell\bar{\nu}_\ell$, by subtracting the $|V_{ub}|^2$ suppressed $B \to X_u\ell\bar{\nu}_\ell$ contribution via

$$\mathcal{B}(B \to X_c\ell\bar{\nu}_\ell) = \mathcal{B}(B \to X\ell\bar{\nu}_\ell) - \Delta\mathcal{B}(B \to X_u\ell\bar{\nu}_\ell)/\epsilon_{\Delta\mathcal{B}}\,. \tag{5.31}$$

We use $\Delta\mathcal{B}(B \to X_u\ell\bar{\nu}_\ell) = (0.159 \pm 0.017)\%$ from [143], which has a lepton–energy cut of $E_\ell > 1\,\text{GeV}$. To correct for this cut, we use a factor of $\epsilon_{\Delta\mathcal{B}} = 0.858 \pm 0.008$ [1]. This yields a total branching fraction of $\mathcal{B}(B \to X_u\ell\bar{\nu}_\ell) = (0.185 \pm 0.020)\%$.

Averaging the indicated measurements listed in Table 5.2, we obtain

$$\mathcal{B}(B \to X_c\ell\bar{\nu}_\ell) = (10.48 \pm 0.13) \cdot 10^{-2}\,, \tag{5.32}$$

which we use as our default branching ratio.

The central value of the branching ratio will dominate the central value of V_{cb}, so a few comments are in order. Our default value differs by $\approx 1.4\,\sigma$ from the value obtained in [112] which is $(10.66 \pm 0.15) \cdot 10^{-2}$. This difference is caused most notably by the inclusion of the Babar measurement [144] into our average, while [112] only include the Belle [145] and BaBar [146] results. In their analysis, the total branching ratio of $B \to X_c\ell\bar{\nu}_\ell$ is a prediction of the fit, determined from the used partial branching ratio measurements at different E_ℓ cuts and the analyzed moments. This approach allows for a self–consistent extrapolation. To allow for an easier comparison with their results, we also determine V_{cb} using an average based on the same branching fractions [145, 146]

$$\mathcal{B}(B \to X_c\ell\bar{\nu}_\ell) = (10.63 \pm 0.19) \cdot 10^{-2}\,. \tag{5.33}$$

This value is in excellent agreement with the value obtained by [112].

In the future, new branching ratio measurements are imperative to clarify the mild tension between the two averages shown above. In addition, new branching ratio measurements with (different) q^2 thresholds would be the natural input for the RPI V_{cb} determination. This way uncertainties from subtracting the $b \to u$ contributions can be avoided, increasing the experimental precision.

[1] We thank Lu Cao, author of [143], for providing this correction to us.

	$\mathcal{B}(B \to X\ell\bar{\nu}_\ell)$ (%)	$\mathcal{B}(B \to X_c\ell\bar{\nu}_\ell)$ (%)	In Average
Belle [145] $E_\ell > 0.6\,\text{GeV}$	-	10.54 ± 0.31	✓
Belle [145] $E_\ell > 0.4\,\text{GeV}$	-	10.58 ± 0.32	
CLEO [147] incl.	10.91 ± 0.26	10.72 ± 0.26	
CLEO [147] $E_\ell > 0.6\,\text{GeV}$	10.69 ± 0.25	10.50 ± 0.25	✓
BaBar [148] incl.	10.34 ± 0.26	10.15 ± 0.26	✓
BaBar SL [146] $E_\ell > 0.6\,\text{GeV}$	-	10.68 ± 0.24	✓
Our Average	-	10.48 ± 0.13	
Average Belle [145] & BaBar [146] $E_\ell > 0.6\,\text{GeV}$	-	10.63 ± 0.19	

Table 5.2: Available measurements of the inclusive $B \to X\ell\bar{\nu}_\ell$ and $B \to X_c\ell\bar{\nu}_\ell$ branching fractions, extrapolated to the full region using the correction factors in (5.30). The χ^2 of our average with respect to the included measurements is 2.2, corresponding to a p-value of 52%.

Belle and Belle II q_n measurements

Belle [17] and Belle II [18] recently presented first measurements of q^2 moments. The Belle measurement presents separate moments for electrons and muons with a minimal q^2 threshold selection of $3.0\,\text{GeV}^2$ up to a maximum value of $10.5\,\text{GeV}^2$. We average the Belle measured electron and muon q^2 moments, fully correlating identical systematic uncertainty sources. Belle II provides measurements with a q^2 threshold starting at $1.5\,\text{GeV}^2$ up to $8.5\,\text{GeV}^2$. Due to the high degree of correlations between the measured moments, we do not analyze the full set of each experiment, but focus on the subset listed in table 5.3. We stress that the result of the analysis is fairly insensitive to the choice of the subset. We do not use moments with thresholds larger than $8\,\text{GeV}^2$, to avoid the endpoint of the q^2 spectrum, whose contributions are dominated by exclusive states. We fully correlate the systematic uncertainties between both measurements related to the composition of the X_c system and form factor uncertainties.

	q^2 threshold $[\text{GeV}^2]$
Belle [143]	$3, 4, 5, 6, 7, 8$
Belle II [18]	1.5, 2.5, 3.5, 4.5, 5.5, 6.5, 7.5

Table 5.3: Analyzed measured q^2 moments from Belle and Belle II.

5.3 Fit results

5.3.1 First V_{cb} determination from q^2 moments

We will now combine the first four central moments of the Belle and Belle II measurements and the branching ratio of eq. (5.32) in our default fit for $|V_{cb}|$. The parameters $|V_{cb}|$, ρ_D^3, r_G^4, and r_E^4 are free parameters in the fit, while m_b, m_c, μ_G^2, and μ_π^2 are included with Gaussian constraints as discussed in chapter 5.2.2. We set the remaining $1/m_b^4$ parameters to zero, as we have limited sensitivity to them, and we include the correlation parameters ρ_{mom} and ρ_{cut} as nuisance parameters in the fit. The result of the fit is listed in table 5.4. We find in particular for $|V_{cb}|$

$$\begin{aligned} |V_{cb}| &= \left(41.69 \pm 0.27\big|_{\mathcal{B}} \pm 0.31\big|_{\Gamma} \pm 0.18\big|_{\text{exp.}} \pm 0.17\big|_{\text{theo.}} \pm 0.34\big|_{\text{constr.}}\right) \cdot 10^{-3}\,, \\ &= (41.69 \pm 0.59) \cdot 10^{-3}\,, \end{aligned} \tag{5.34}$$

where the uncertainties stem from the experimental branching ratio $\mathcal{B}$, the theoretical uncertainty on the total rate Γ, the experimental and theoretical uncertainties on the q^2 moments and the uncertainty from the external constraints, respectively. We are able to determine V_{cb} with percent level uncertainty, which clearly shows the potential of this method. Note that the most important error sources for V_{cb} come from the constraints on the parameters and the uncertainties of the experimental branching fraction and the theoretical value for the total rate. In order to enhance them, more precise determinations would be desirable, especially for the HQE parameters. As already elaborated on in chapter 5.1.4, a determination of μ_3 with lattice values (or another method) could also help improve this error. Regarding the uncertainty of the branching fraction, new determinations with cuts on the q^2 threshold for the total rate may reduce this error significantly. Finally note that the error due to the q^2 moments is relatively small for V_{cb} even though they are known less precisely than the total rate.

	$\lvert V_{cb}\rvert \times 10^3$	m_b^{kin}	$\overline{m}_c$	μ_G^2	μ_π^2	ρ_D^3	r_G^4	$r_E^4 \times 10$	ρ_{cut}	ρ_{mom}
Value	41.69	4.56	1.09	0.37	0.43	0.12	-0.21	0.02	0.05	0.09
Uncertainty	0.59	0.02	0.01	0.07	0.24	0.20	0.69	0.34	$^{+0.03}_{-0.01}$	$^{+0.10}_{-0.10}$

Table 5.4: Results of our default fit using both Belle and Belle II data for $|V_{cb}|$, the masses m_b^{kin} and $\overline{m}_c$, the HQE parameters (which are included in the fit), and the correlation parameters ρ_{cut} and ρ_{mom}. All parameters are expressed in GeV at the appropriate power.

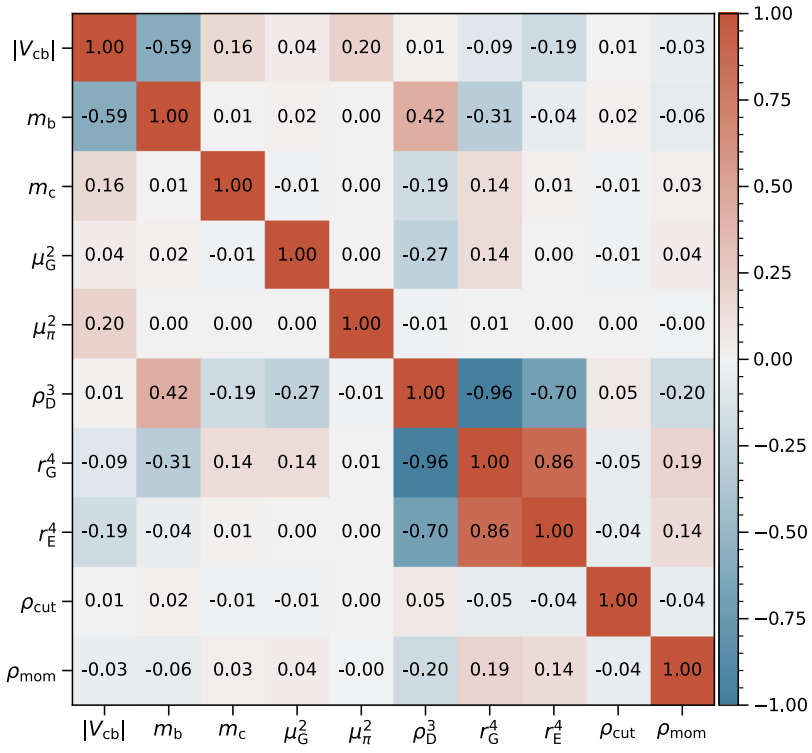

Figure 5.4: Correlation matrix for $|V_{cb}|$, the HQE parameters, and the correlation parameters ρ_{cut} and ρ_{mom}.

However because we use normalized moments, V_{cb} drops out and thus their effect is only indirectly affecting it via the HQE parameters.

In addition we depict the correlation of the different fit parameters in figure 5.4. We note that $|V_{cb}|$ shows a small correlation to m_c and the HQE parameters, while a larger negative correlation of -0.59 with m_b is observed. This is caused by the overall m_b dependence of the total rate. Moreover we find that the parameters r_E^4, r_G^4 and ρ_D^3 are strongly correlated amongst each other. This effect might be caused by relations between their respective matrix elements via the equations of motion of eq.(3.20). In contrast to the normalized moments, $|V_{cb}|$ has a moderate correlation with μ_π^2, because its effect is not shifted to $1/m_b^4$ in the total rate. Finally, as already noted in figure 5.3, r_E^4 and r_G^4 also show an effect on V_{cb} in the correlation matrix.

In figure 5.5, we show the fit results for the four central q^2 moments as a function of q^2_{cut}, together with the analyzed Belle and Belle II measurements. We find $\chi^2_{\text{min}} = 7.17$ for our fit with 49 degrees of freedom (dof), indicating that the fit converged excellently. Just like the former analyses [112, 114, 126] we recover a poor fit $\chi^2/\text{dof} = 5.02$, when we do not include the theory covariance. The obtained $|V_{cb}|$ and ρ_D^3 values are

compared in figure 5.6, indicating a strong agreement between the individual fits and the combined Belle and Belle II ones.

We discussed in chapter 5.2.4 that there is a mild tension between the different branching fractions. In order to use a different input of the $B \to X_c \ell \bar{\nu}_\ell$ branching ratio, the corresponding V_{cb} value can be easily obtained by a rescaling

$$|V_{cb}| = \sqrt{\frac{\mathcal{B}(B \to X_c \ell \bar{\nu})}{(10.48 \pm 0.13)\%}} \times (41.69 \pm 0.59) \cdot 10^{-3} \,. \tag{5.35}$$

Using (5.33), we thus find

$$|V_{cb}| = (41.99 \pm 0.65) \cdot 10^{-3} \,. \tag{5.36}$$

This value is in excellent agreement with the results [112], especially when taking into account that their fit results include estimates for the power corrections, which decreases the value given in (5.1) by about 0.25%.

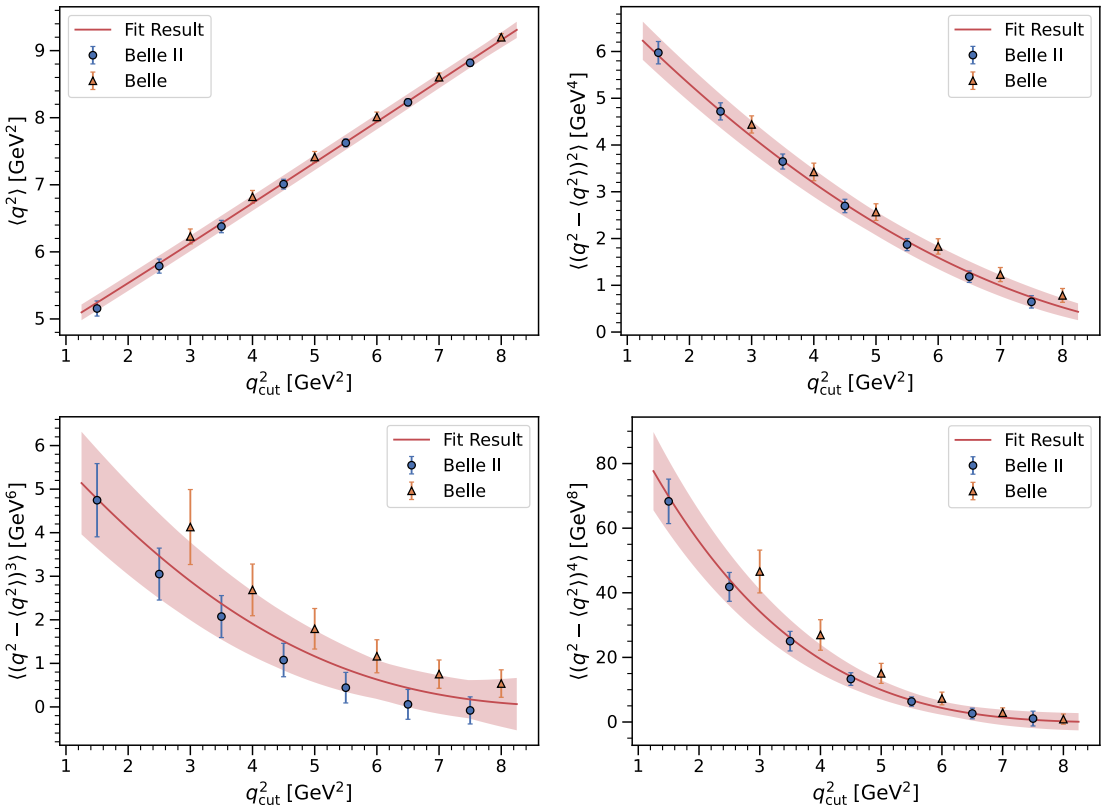

Figure 5.5: Fit projections for the central q^2 moments as a function of the q^2 threshold, combined with the measured moments from both Belle and Belle II.

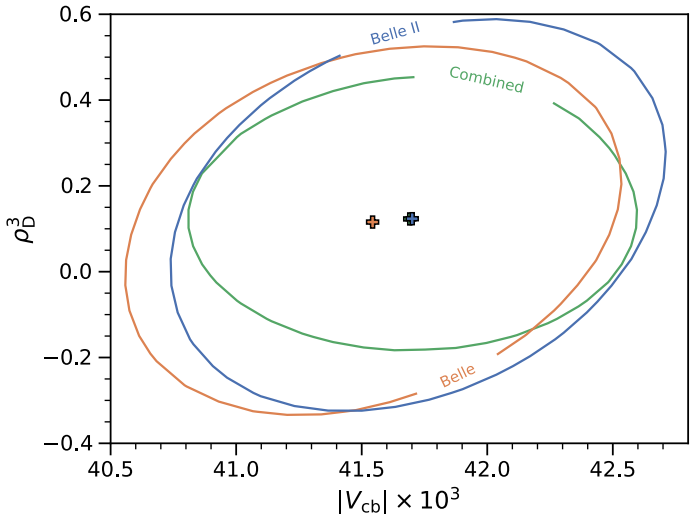

Figure 5.6: Comparison between Belle, Belle II and the combined fit for the correlation between $|V_{cb}|$ and ρ_D^3. The crosses indicate the best-fit points.

5.3.2 Theory correlations and HQE parameters versus V_{cb}

In our default fit, we introduce the two correlation parameters ρ_{mom} and ρ_{cut} as nuisance parameters to let the optimizer find their best–fit value. The result for this procedure is listed in table 5.4. In appendix A.5, we find that the one dimensional χ^2 profiles of these parameters have a non–parabolic behaviour. This means that the Gaussian approximation around the minimum is not well justified anymore and thus we may not use the inverse of the Hesse matrix to determine the uncertainty on these parameters. To estimate the confidence intervals, which are quoted in table 5.4, we therefore make use of ensembles of pseudo–experiments. This means, we fix the other parameters of the fit to their obtained values in the theoretical prediction, while varying the respective correlation parameter. This lets us determine the confidence interval from table 5.4.

Of particular interest is also the effect of the chosen values of ρ_{mom} and ρ_{cut} on V_{cb}. To investigate this, we show in figure 5.7 the 2D scans of the $\Delta\chi^2 = \chi^2 - \chi^2_{\text{min}}$ contours for V_{cb} versus ρ_{cut} and ρ_{mom}. Profiling over a large range of both ρ_{mom} and ρ_{cut} only has a small impact on the determined value of V_{cb}. In other words, our uncertainty on V_{cb} includes a large range of possible correlation coefficients. For completeness, we also performed fits for fixed values of ρ_{mom} and ρ_{cut}. The fit results for V_{cb}, ρ_D^3, r_E^4 and r_G^4 are given appendix A.5. These scans also show, that V_{cb} is stable against variations of ρ_{mom} and ρ_{cut}, which backups the findings of figure 5.7. A similar conclusion was presented in [114]. In summary, we conclude that V_{cb} is very stable with respect to both of our nuisance parameters. As these parameters are a priori unknown and fully

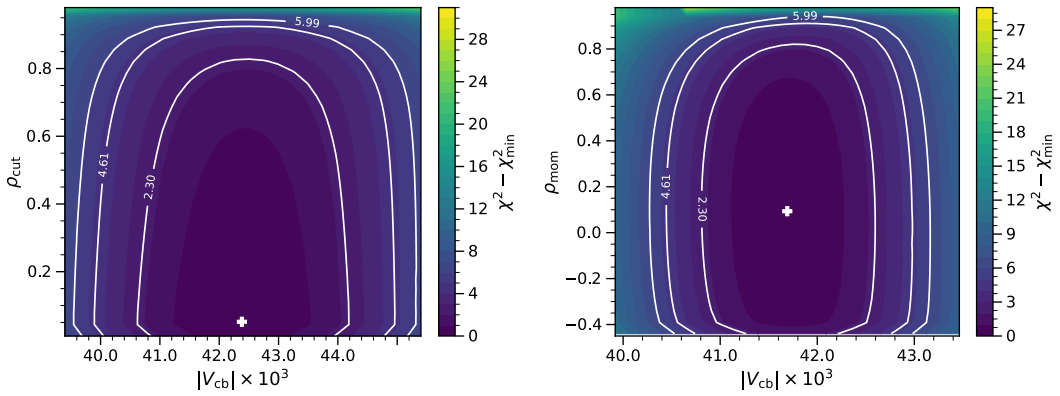

Figure 5.7: 2D χ^2 profile scans of $|V_{cb}|$ versus ρ_{cut} and ρ_{mom}. The minimum χ^2_{min} is subtracted from the χ^2 function.

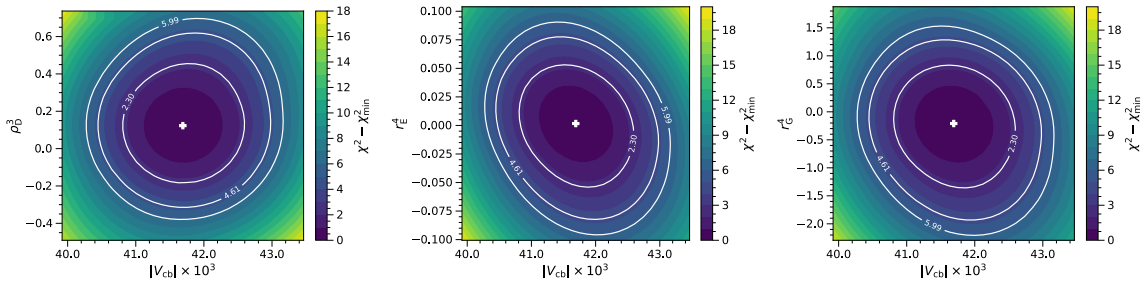

Figure 5.8: 2D χ^2 profile scans of $|V_{cb}|$ versus ρ^3_D, r^4_E and r^4_G. The minimum χ^2_{min} is subtracted from the χ^2 function.

depend on the chosen form of the theoretical correlation this is an important finding.

In figure 5.8, we show the two–dimensional profile scan of $\Delta\chi^2$ between ρ^3_D, r^4_E and r^4_G versus V_{cb}. We observe no sizeable correlations here and so conclude that the fit is stable with regard to these parameters.

5.3.3 Determination of the HQE parameters

Besides our our main result – the determination of V_{cb} – also the determination of the HQE parameters is insightful. In our fit, both μ^2_π and μ^2_G are constrained by external inputs, and our fit results in table 5.4 show that our sensitivity is too limited to constrain both parameters beyond their default values. On the other hand, ρ^3_D, r^4_E and r^4_G are free parameters in our default fit scenario and can be determined from the q^2 moments. We find

$$\rho^3_D = \left(0.12 \pm 0.12\big|_{\mathrm{exp.}} \pm 0.13\big|_{\mathrm{theo.}} \pm 0.11\big|_{\mathrm{constr.}}\right) \mathrm{GeV}^3 = (0.12 \pm 0.20)\,\mathrm{GeV}^3\,, \quad (5.37)$$

where the uncertainty stems from the experimental and theoretical uncertainty on the moments and the external inputs, respectively. For the $1/m_b^4$ parameters, we are able to constrain r_E^4 and r_G^4 for the first time in a completely data–driven way. We find

$$\begin{aligned} r_E^4 &= \left(0.02 \pm 0.21\big|_{\text{exp.}} \pm 0.27\big|_{\text{theo.}} \pm 0.00\big|_{\text{constr.}}\right) \cdot 10^{-1}\,\text{GeV}^4 \qquad (5.38)\\ &= (0.02 \pm 0.34) \cdot 10^{-1}\,\text{GeV}^4\,, \\ r_G^4 &= \left(-0.21 \pm 0.42\big|_{\text{exp.}} \pm 0.49\big|_{\text{theo.}} \pm 0.25\big|_{\text{constr.}}\right) \text{GeV}^4 \qquad (5.39)\\ &= (-0.21 \pm 0.69)\,\text{GeV}^4\,. \end{aligned}$$

Both values are relatively small and compatible with zero within their uncertainties. We note that r_E^4 – the $1/m_b^4$ parameter we are most sensitive to – is constrained to be very well below $1\,\text{GeV}^4$ or even Λ_{QCD}^4, and also our result for r_G^4 excludes spuriously (unexpected) large values for this parameter. This implies that the HQE seems to be well behaved and converges well up to this order.

Our determination of ρ_D^3 is compatible with zero. In figure A.7 of appendix A.5, we observe that this also remains true for all fixed ρ_{mom} and ρ_{cut} choices. We note that our definition of ρ_D^3 differs from that used in [112], because we include an additional $1/m_b$ contribution, namely its RPI completion, as discussed in chapter 3.2.2. Therefore the result in [112], which reads $\rho_D^3 = (0.185 \pm 0.031)\,\text{GeV}^3$, cannot be directly compared to ours. However, it is worth exploring the apparent difference in sensitivity for ρ_D^3 between the q^2 method and the moment fit of [112]. To understand this differences, we investigated the two–dimensional contours in $\Delta\chi^2$ of ρ_D^3 vs. r_E^4 and r_G^4 as well as r_E^4 vs r_G^4. These scans are given in the left, middle and right panel of figure. 5.9, respectively. The contours reveal a large (anti)correlation between the three parameters. In fact, the slope of the moments, as a function of q_{cut}^2, is similar for the variation of the three parameters. This indicates that they can compensate each other. Especially the slope, induced by different values of ρ_D^3 and r_G^4 is very similar. This suggests that, at least in this analysis, we are only sensitive to a linear combination of these parameters. This, combined with the rather conservative theoretical uncertainties, can explain our limited sensitivity to ρ_D^3. Although they are independent in the HQE, this may be a hint that a further reduction of parameters is possible – for example when expressing everything in full QCD states (see discussion in [41]).

On the other hand, for a more direct comparison with [112], we may also consider a fit with all $1/m_b^4$ corrections set to zero. We find the results listed in table A.3 in appendix A.5, most notably $\rho_D^3 = (0.03 \pm 0.02)\,\text{GeV}^3$. This determination differs

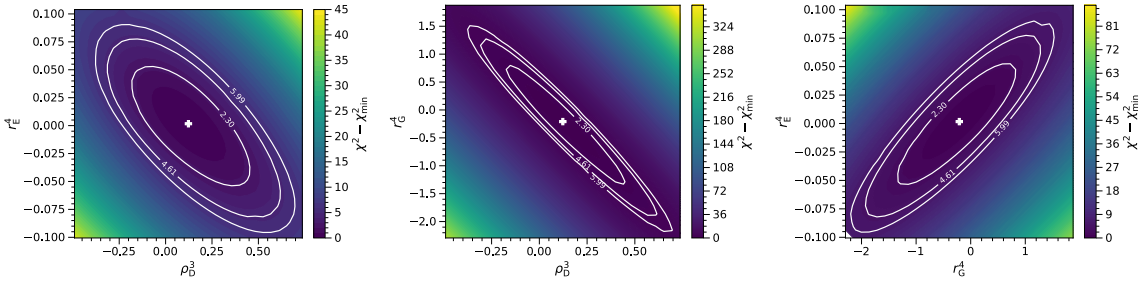

Figure 5.9: 2D χ^2 profile scans of ρ_D^3 versus (left) r_E^4 and (middle) r_G^4, and of r_E^4 versus r_G^4 (right). The minimum χ^2_{min} is subtracted from the χ^2 function.

substantially from that obtained by [112] and could indicate that the q^2 moments actually add additional information on the HQE parameters.

5.3.4 Including all $1/m_b^4$ terms

In our default fit, we only consider the $1/m_b^4$ terms r_E^4 and r_G^4, because the sensitivity to the others is very limited. To study the effect of these neglected parameters, we further perform a fit including s_B^4, s_E^4 and s_{qB}^4. In order to have the fit converge, we need to include a constraint on each of the parameters. We include standard normal Gaussian constraints (i.e. mean of zero, standard deviation one) for all $1/m_b^4$ terms. The result is given in table 5.5, where we observe no significant deviations from the default fit results. As expected, this fit shows that the most sensitive $\mathcal{O}(1/m_b^4)$ parameters are r_G^4 and r_E^4, since the post–fit parameter uncertainties can be reduced from unity. For the remaining HQE parameters, no significant uncertainty reduction can be reported. Most importantly, we obtain exactly the same V_{cb} value as from our default fit, namely

$$|V_{cb}| = (41.69 \pm 0.59) \cdot 10^{-3} \,. \tag{5.40}$$

To account for missing higher–order corrections from neglecting s_E^4, s_B^4 and s_{qB}^4, we add an additional uncertainty to our default fit in (5.34) by including variations of these parameters of $\pm 1\,\text{GeV}^4$.

	$\lvert V_{cb}\rvert \times 10^3$	m_b^{kin}	$\overline{m}_c$	μ_G^2	μ_π^2	ρ_D^3	r_G^4	$r_E^4 \times 10$	s_E^4	s_{qB}^4	s_B^4	ρ_{cut}	ρ_{mom}
Value	41.69	4.56	1.09	0.37	0.43	0.10	-0.12	0.04	-0.04	-0.02	0.04	0.05	0.10
Uncertainty	0.59	0.02	0.01	0.07	0.24	0.18	0.68	0.31	0.95	0.99	0.95	$^{+0.03}_{-0.01}$	$^{+0.10}_{-0.10}$

Table 5.5: Fit result including all $1/m_b^4$ parameters with a standard normal Gaussian constraint. All parameters are expressed in GeV at their appropriate power.

In total, we find a variation on V_{cb} of $0.23 \cdot 10^{-3}$, which is dominated by the contribution of s_E^4. Our final default result for $|V_{cb}|$ including all error sources is therefore

$$|V_{cb}| = \left(41.69 \pm 0.59\big|_{\text{fit}} \pm 0.23\big|_{\text{h.o.}}\right) \cdot 10^{-3} = (41.69 \pm 0.63) \cdot 10^{-3}\,, \tag{5.41}$$

where we added both uncertainties in quadrature. This value presents an independent cross–check of previous inclusive V_{cb} determinations, using both new data and a new method. It shows good agreement with the previously obtained inclusive V_{cb} in eq.(5.1) from [112], which was obtained from lepton–energy and hadronic invariant mass moments. We emphasize that any tension between the two determinations is fully due to a different input for the total branching ratio.

Our analysis can be improved in the future by adding higher–order perturbative corrections as indicated in table 5.1. We expect that their inclusion can reduce the uncertainty on the extraction of the HQE parameters. In addition the found correlations between ρ_D^3, r_E^4 and r_G^4 should be further studied. Finally it may be beneficial to combine our analysis with that of [112], to include lepton moments and hadronic invariant mass moments. This requires using the full set of HQE parameters, but may have the benefit of higher statistics. All these future improvements have the potential to push the inclusive V_{cb} determination to below percent level uncertainty.

Chapter 6

New analysis of semileptonic $B \to X_u \ell \nu$ decays

In this last chapter, we discuss the determination of V_{ub} from the inclusive, semileptonic decay $B \to X_u \ell \bar{\nu}$. Just as V_{cb}, the CKM element V_{ub} poses an important input in a variety of processes and is often the key component in precision. In addition, there is also a relatively strong discrepancy of about $3\,\sigma$ between the inclusive and exclusive determinations [111, 149]. Currently the world average of inclusive and exclusive measurements are [150]

$$\begin{aligned} |V_{ub}^{\text{excl.}}| &= (3.67 \pm 0.09 \pm 0.12) \times 10^{-3}\,, \\ |V_{ub}^{\text{incl.}}| &= \left(4.32 \pm 0.12^{+0.12}_{-0.13}\right) \times 10^{-3}\,, \end{aligned} \tag{6.1}$$

which shows that an increase in precision is highly desirable from both sides.

In contrast to the transition into a charm quark, we are now facing a situation in which we have to subtract the unwanted background coming from Cabbibo–favoured $B \to X_c \ell \nu$ decays. Its branching fraction is about 100 times larger and thus large kinematical cuts need to be applied in order to render the experimental measurements possible. In particular this puts us in a situation in which the hadronic final states carry very large energies $E \sim m_B$, yet only have a moderate invariant mass $m_X^2 \sim m_B \Lambda_{\text{QCD}}$, as discussed in chapter 3.3.1. This kinematic region introduces new non–perturbative and non–local quantities – the shape functions we introduced in chapter 3.3.2. Because their exact form is not known and can (currently) not be determined with theoretical methods, their underlying functional form has to be modeled. This introduces an additional source of uncertainties, since they can only be constrained through the moments of the local OPE. Attempts were made using neural networks [151] or the

spectra of $B \to X_s\gamma$ [152, 153] to determine the leading shape function more model–independently. However, they have not been realized in analyses of V_{ub} yet or suffer from non–universal effects.

Besides, there are basically two sources of corrections to the partial rates. On the one hand there are perturbative corrections in α_s, that can be systematically introduced when factorizing the hadronic tensor, as discussed in chapter 3.3.3. On the other hand there are higher power corrections to the shape function. At subleading order, a set of additional non–local objects emerges, which, like the leading shape function, need to be modelled. Further power corrections are currently only constrained by the local matrix elements of the full OPE.

To tackle the challenge of modelling the shape functions and systematically introducing corrections to the rate, several approaches were developed. Most notably there are BLNP [20], GGOU [154] and DGE [155]. The method used in GGOU is similar to BLNP in that it utilizes perturbative results to the hadronic tensor, but the shape functions are defined differently. They include subleading effects to all orders, but are non–universal as a result. In DGE ("dressed gluon exponentiation") the perturbative result is continued into the infrared regime using the renormalon structure obtained in the large β_0 limit.

We follow the idea of BLNP and factorize the hadronic contributions as discussed in chapter 3.3. Currently the the framework only contains the NLO corrections to the perturbative quantities, while the power corrections were determined up to $1/m_b^2$. Since all ingredients for the NNLO determination are available now [58], we develop a program which contains all of these state–of–the–art corrections and provide this to the experimental community [12]. In addition we use a new novel method to include all possible information into the shape function. It is inspired by the approach in [152] and models the radiative tail of the shape function by convoluting with the partonic soft function. Furthermore, we transition to the kinetic scheme with a method that preserves the full RG evolution. Finally, we treat the subleading shape functions fully independently from the leading one, allowing for a separate estimation of the uncertainties from the respective contribution.

6.1 Modelling the shape function

6.1.1 Model ansatz and requirements

Any model for the shape function must fulfil two conditions, when integrated over a sufficiently large interval $-\Lambda_{\rm cut} \leq \omega \leq \bar{\Lambda}$, where $\Lambda_{\rm cut} \sim \mu_0 \gg \Lambda_{\rm QCD}$. On the one hand its moments need to coincide with the matrix elements of the local OPE and on the other hand its radiative tail is determined by a perturbative expansion.

The moments of the full OPE are recovered, because the operator in the matrix element of eq.(3.47) can be expanded in a series of local operators as [60, 152]

$$S(\omega,\mu_0) = \sum_n C_n(\omega,\mu_0)\langle B|\bar{b}_v(inD)^n b_v|B\rangle + \dots \,, \tag{6.2}$$

where $C_n(\omega,\mu_0)$ are a set of Wilson coefficients that contain the perturbative information on the shape function and the dots represent operators of dimension six and higher, which we do not take into account. The moments of the unshifted shape function yield then

$$M_n(\Lambda_{\rm cut},\mu_0) = \int\limits_{-\Lambda_{\rm cut}}^{\bar{\Lambda}} {\rm d}\omega\, \omega^n S(\omega,\mu_0) = \sum_n \langle B|\bar{b}_v(inD)^n b_v|B\rangle \int\limits_{-\Lambda_{\rm cut}}^{\bar{\Lambda}} {\rm d}\omega\, \omega^n C_n(\omega,\mu_0)\,, \tag{6.3}$$

meaning they are determined by the local matrix elements plus the perturbative information contained in the C_n [20]. This perturbative information generates a radiative tail, which should be included as adequately as possible. In BLNP this tail was "glued" onto the shape function at some high value of ω [20]. However to harness all available information for the shape function, we follow a different approach suggested in [152]. The radiative part of the shape function, even though a non–perturbative object, can formally be calculated by evaluating it with free quark states. This yields the partonic part of the shape function $S^{(\rm part)}$, which is known up to NNLO [72] and given in eq.(A.6). We include it in our model by convoluting with a non–perturbative model function $\hat{F}(\hat{k})$

$$\hat{S}(\hat{\omega},\mu_0) = \int\limits_0^{\hat{\omega}} {\rm d}\hat{k}\, S^{(\rm part)}(\hat{\omega}-\hat{k},\mu_0)\hat{F}(\hat{k})\,, \tag{6.4}$$

where the integration variable is written in terms of the hatted form $k = \bar{\Lambda} - \hat{k}$ as before. Note that all dependence on the soft scale μ_0 comes from the partonic shape function and thus the RG evolution from eq.(3.59) remains correct to all orders. Moreover, this way of modelling the shape function has the radiative tail automatically built in, as long as the model function $\hat{F}(\hat{k})$ is suppressed at large $\hat{k}$. It furthermore allows for a simplification when evolving the shape function to the intermediate scale μ_i, as we will show below. Note that this ansatz should not be misconstrued as a factorization of perturbative and non–perturbative effects. It merely contains information on the behaviour of the shape function for larger $\hat{\omega}$ that is technically obtained as an expansion in $\alpha_s(\mu_0)$. However the shape function itself for small values of $\hat{\omega} \sim \Lambda_{\rm QCD}$ is entirely non–perturbative. When allowing for an expanded phase space, for example with very modest kinematical cuts or even the total decay width, this ansatz transitions smoothly between the shape function region and the local OPE.

Note that the prescription in eq.(6.4) is consistent with the OPE result. Expressing the moments of $\hat{S}(\hat{\omega}, \mu_0)$ with a cutoff in terms of the unshifted shape function reads

$$M_n(\Lambda_{\rm cut}, \mu_0) = \int\limits_{-\Lambda_{\rm cut}}^{\bar{\Lambda}} \mathrm{d}k\, F(k) \int\limits_{0}^{\Lambda_{\rm cut}+k} \mathrm{d}\ell\, S^{(\rm part)}(\ell, \mu_0)(k-\ell)^n \,. \tag{6.5}$$

After expanding the inner integral around $k = 0$ one obtains an expansion involving perturbative coefficients to the cutoff moments $m_j(\Lambda_{\rm cut})$ of $F(k)$. Therefore, as in eq.(6.3), the moments of the model function $F(k)$ are given by the matrix elements of the local OPE, which read

$$m_0(\Lambda_{\rm cut}) = 1\,, \quad m_1(\Lambda_{\rm cut}) = 0\,, \quad m_2(\Lambda_{\rm cut}) = \frac{1}{3}\mu_\pi^2 \quad m_3(\Lambda_{\rm cut}) = -\frac{1}{3}\rho_D^3\,. \tag{6.6}$$

This way, we utilize the information about the radiative tail included in $S^{(\rm part)}$ and identify the moments of the model function $F(k)$ with the ones from the OPE. The perturbative coefficients involve logarithms of the form $\ln {}^{\Lambda_{\rm cut}}\!/_{\mu_0}$, which are under control as long as the cutoff and the scale are of comparable order. Therefore there should be no support for $\hat{F}(\hat{k})$ in the region where $k > \mu_0$, i.e. at some cutoff k_c, the model function shall vanish $\hat{F}(\hat{k} > k_c) = 0$. We expect this cutoff to lie somewhere around $k_c \sim \mu_0 + \bar{\Lambda} \approx 2\,\mathrm{GeV}$. For $b \to u$ transitions experimental cuts are well below this value. However, in order to recover the full OPE result in this framework, it is necessary to ensure that the shape function has this feature. To that end we introduce a compactification operator in chapter 6.1.4, which guarantees a finite support for the

model function, while conserving the moment relations. This will serve as a less restrictive and more soundly motivated alternative to the demand for positivity in other approaches [152, 154].

Finally we demonstrate how the radiative tail given by $S^{(\text{part})}$ and the model function $\hat{F}(\hat{k})$ can be smoothly integrated into the factorized formula for the leading structure functions eq.(3.59). The procedure is equivalent to the Laplace transform of the jet function. First note that the partonic part of the shape function can be written in terms of its Laplace transform with derivative operators [71]

$$S^{(\text{part})}(\ell, \mu_0) = \tilde{s}(\partial_\tau, \mu_0) \frac{\mathrm{e}^{-\gamma_\mathrm{E}\tau}}{\Gamma(\tau)} \frac{1}{\ell} \left(\frac{\ell}{\mu_0}\right)^\tau , \tag{6.7}$$

where $\tau \to 0$ after taking the derivatives. We may now plug eq.(6.7) and eq.(6.4) into the factorized structure functions from eq.(3.59), where we only depict the last line for simplicity

$$f_i^{(0)}(P_+, y) \sim \tilde{s}(\partial_\tau, \mu_0) \frac{\mathrm{e}^{-\gamma_\mathrm{E}(\eta+\tau)}}{\Gamma(\eta)\Gamma(\tau)} \int_0^{P_+} \mathrm{d}k\, F(k) \int_k^{P_+} \mathrm{d}\omega\, (P_+ - \omega)^{\eta-1} (\omega - k)^{\tau-1} \mu_0^{-(\eta+\tau)} . \tag{6.8}$$

Here we changed the orders of integration and pulled the Laplace transform of the shape function out of the integral. The integral over ω can be solved analytically and yields

$$\int_k^{P_+} \mathrm{d}\omega\, (P_+ - \omega)^{\eta-1} (\omega - k)^{\tau-1} = (P_+ - k)^{\eta+\tau-1} \frac{\Gamma(\eta)\Gamma(\tau)}{\Gamma(\eta+\tau)} \tag{6.9}$$

and thus upon defining $\eta' = \eta + \tau$, eq.(6.8) becomes

$$f_i^{(0)}(P_+, y) \sim \tilde{s}(\partial_{\eta'}, \mu_0) \frac{\mathrm{e}^{-\gamma_\mathrm{E}\eta'}}{\Gamma(\eta')} \int_0^{P_+} \mathrm{d}k\, F(k) \frac{1}{P_+ - k} \left(\frac{P_+ - k}{\mu_0}\right)^{\eta'} . \tag{6.10}$$

Note that we changed the variable of the derivative in $\tilde{s}(\partial_{\eta'}, \mu_0)$ (and in the full structure function also $\tilde{j}$) as well, because it generates the same logarithms when taken with respect to η'. With this procedure we have the same advantage that we had with the Laplace transform of the jet function. We automatically generate the correct scale evolution from $\mu_0 \to \mu_i$ and as an added benefit, do not have to take care of the

interference of the distributions in the jet and partonic shape functions. In turn higher order corrections to $\tilde{s}$ can easily be implemented, when enhancing the precision of this method in the future.

6.1.2 Change to the kinetic scheme

In order to ensure that we do not suffer from renormalon issues, we transfer the mass and the OPE parameters to the kinetic scheme. In contrast to the procedure for $B \to X_c \ell \bar{\nu}$, we have to make sure that the scheme transition does not affect the RG evolution and that the radiative corrections in the partonic shape function do not spoil the convergence after the scheme change. In other words, we want to shift the $\mathcal{O}(\alpha_s)$ contributions between $S^{(\text{part})}$ and the OPE parameters $\bar{\Lambda}$ and μ_π in such a way that infrared renormalon ambiguities cancel each other and thus the overall perturbative series has a better convergence.

First of all we need the moments of the shifted model function $\hat{F}(\hat{k})$, which read

$$M_n^{\text{pole}} = \int_0^\infty \mathrm{d}\hat{k}\, \hat{k}^n \hat{F}^{\text{pole}}(\hat{k})\,, \tag{6.11}$$

where for this section, we explicitly denote the mass scheme of each quantity. In terms of the unshifted moments they are easily obtained to be

$$M_0^{\text{pole}} = 1\,, \quad M_1^{\text{pole}} = \bar{\Lambda}\,, \quad M_2^{\text{pole}} = \bar{\Lambda}^2 + \frac{1}{3}\mu_\pi^2\,, \quad M_3^{\text{pole}} = \bar{\Lambda}^3 + \bar{\Lambda}\mu_\pi^2 + \frac{1}{3}\rho_D^3\,. \tag{6.12}$$

Changing the model function to the kinetic mass scheme amounts to adding a function $g_n(\hat{k})$ with an appropriate corrective coefficient to $\hat{F}^{\text{pole}}(\hat{k})$, where the function $g_n(\hat{k})$ has vanishing moments up to the order we are including, ensuring that the coefficients start at order α_s. Specifically the scheme change is obtained via

$$\hat{F}^{\text{pole}}(\hat{k}) = \hat{F}^{\text{kin}}(\hat{k}) + \sum_{n=1}^{\infty} c_n(\alpha_s(\mu_0)) g_n(\hat{k})\,, \tag{6.13}$$

where the coefficients c_n contain the α_s correction from the scheme change. The functions g_n are not unique and can be model–dependently or independently constructed. In [152] moments up to $n = 2$ were included and the function g_n were constructed from the first n derivatives of $\hat{F}^{\text{kin}}(\hat{k})$. Written in terms of derivative operators this achieves model–independence on a formal level, because the effects of the derivative can be applied to the partonic shape function when integrated by parts. The downside

of this ansatz is determined by the behaviour of $\hat{F}^{\rm kin}(\hat{k})$ near the origin. When acting on it with higher order derivatives, the model preferably has to behave at least like a monomial of the same order. In the specific case of [152], moments up to $n = 2$ had been included and thus $\hat{F}^{\rm kin}(\hat{k})$ needed to vanish faster than $\hat{k}^2$ near the origin. Thus including more moments requires to include ever slower onsets. We circumvent this problem by choosing an ansatz, where g_n contains derivatives with respect to $\ln \hat{k}$, which do not alter the behaviour at the origin. It reads

$$\hat{F}^{\rm pole}(\hat{k}) = \mathbf{G}(\alpha_s(\mu_0))\hat{F}^{\rm kin}(\hat{k}, \mu_0)\,, \tag{6.14}$$

where we defined

$$\mathbf{G}(\alpha_s(\mu_0)) = \sum_{n=0}^{\infty} c_n(\alpha_s)\mathbf{g}_n(\hat{k})\,, \quad \mathbf{g}_n(\hat{k}) = \sum_{\ell=0}^{n} \binom{n}{\ell} \frac{\hat{k}^\ell}{\ell!} \left(\frac{\mathrm{d}}{\mathrm{d}\hat{k}}\right)^\ell . \tag{6.15}$$

The perturbative coefficients can easily be determined by comparing the moments of $\hat{F}^{\rm kin}(\hat{k}, \mu_0)$ and $\hat{F}^{\rm pole}(\hat{k})$ with the above ansatz; they read in closed form

$$c_n(\alpha_s) = \sum_{\ell=0}^{n} \binom{n}{\ell} (-1)^\ell \left(\frac{M_\ell^{\rm pole}}{M_\ell^{\rm kin}}\right)\,, \tag{6.16}$$

where all HQE parameters in $M_\ell^{\rm pole}$ are related to those in the kinetic scheme by the perturbative corrections explicitly denoted before in eq.(5.15). This procedure enables us to change from the pole to any small–distance scheme in a model–independent fashion, by applying derivatives to our model function $\hat{F}(\hat{k})$. Also no care needs to be taken for the behaviour near the origin, as taking the derivatives with respect to $\ln \hat{k}$ ensure that no discontinuities are generated.

6.1.3 Simple models for $\hat{F}^{\rm kin}(\hat{k})$

Having defined the overall model ansatz for the shape function, we may now proceed by modelling the function $\hat{F}^{\rm kin}(\hat{k})$. For convenience we introduce a dimensionless variable $x := \hat{k}/k_0$, where k_0 is a model–dependent constant that provides a scale for each of the models we construct. The existence of finite moments implies further that the functions must fall toward zero for $x \to \infty$ faster than any monomial. In general such functions have a large x behaviour $\sim x^{-\xi(x)} = \exp(-\xi(x) \ln x)$, where $\xi(x)$ grows beyond any boundary. Typical examples are $\xi(x) = x/\ln x$ (exponential model), or a faster growing $\xi(x) = x^2/\ln x$ (Gaussian model), or a slower growing $\xi(x) = \ln x$

(logarithmic model).

First we pick a weight function $w(x)$ that determines the asymptotic behaviour of the model for small and large x. These already contain parameters that may be freely chosen. All of the models we consider here will have $\hat{F}^{\text{kin}}(0) = 0$, i.e. they are continuous model functions. The explicit weight functions we consider are

$$\begin{aligned} w_{\text{fin}}(x) &= x^{\alpha}(1-x)^{\beta}\theta(1-x)\,, \\ w_{\text{gauss}}(x) &= x^{\alpha}\mathrm{e}^{-x^2}\,, \\ w_{\text{exp}}(x) &= x^{\alpha}\mathrm{e}^{-\beta x}\,, \\ w_{\log}(x) &= \mathrm{e}^{\ln^2 x}\,. \end{aligned} \tag{6.17}$$

Here α controls the onset for small x, while β is used to rescale k_0 in the exponential model. For the finite model it controls the offset of the function for large x.

The second step in the construction is to multiply the weight function with a polynomial $p(x)$, whose degree matches the number of moments one wishes to include. Its coefficients are tuned exactly such that they obey the aforementioned moment constraints M_n^{kin}. Thus the model ansatz for the function $\hat{F}^{\text{kin}}(\hat{k})$ finally reads

$$\hat{F}^{\text{kin}}(\hat{k}) = \frac{1}{k_0} w\left(\frac{\hat{k}}{k_0}\right) p\left(\frac{\hat{k}}{k_0}\right)\,. \tag{6.18}$$

With the model parameters α, β and k_0, as well as the weight functions, there is an abundance of different options to choose from. The guiding principle we follow is to have as little features as manageable, since for the study of inclusive B decays, we cannot resolve any resonances or features of exclusive decays with our model. Thus this "smoothness" of the model function may be considered an application of Ockhams razor, according to which a theory with fewer assumptions is in general to be preferred.

Note that we may further motivate the ansatz eq.(6.18) in the following way. As explained, we would like to avoid unnecessary oscillations in $\hat{F}^{\text{kin}}(\hat{k})$, even though we do not require it to be positive definite. To determine a general form for the ansatz fulfilling these conditions, we consider the functional

$$\chi^2[\hat{F}^{\text{kin}}] = \frac{k_0}{2}\int_0^{\infty} \mathrm{d}\hat{k}\, \frac{\hat{F}^{\text{kin}^2}(\hat{k})}{w(\hat{k}/k_0)}\,, \tag{6.19}$$

and minimize it, while keeping the moments of $\hat{F}^{\text{kin}}(\hat{k})$ constrained. By considering the norm of $\hat{F}^{\text{kin}}(\hat{k})$, it is clear, that large oscillations will lead to a larger χ^2 and thus be

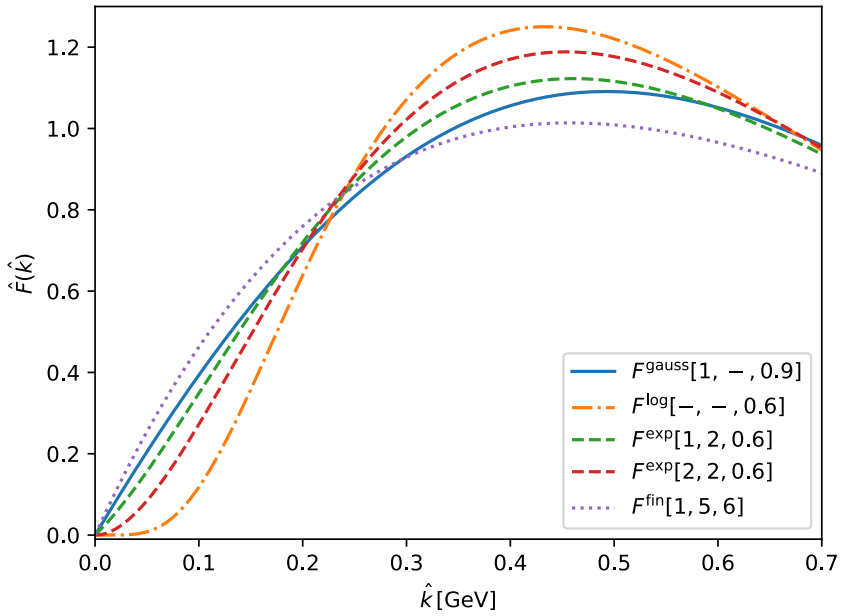

Figure 6.1: Cluster of different models for $\hat{F}^{\text{kin}}(\hat{k})$, which we use for our analyses. The legend depicts the respective chosen weight function from eq.(6.17) and the set of inputs for the free parameters as $F^{\text{weight}}[\alpha, \beta, k_0]$.

excluded by the minimum. In addition, the regions $\hat{k} \to 0$ and $\hat{k} \to \infty$ receive diverging weights, which forces $\hat{F}^{\text{kin}}(\hat{k})$ to vanish there fast enough such that the integral still converges. Varying $\hat{F}^{\text{kin}}(\hat{k})$, while simultaneously keeping the moment constraints fixed with Lagrange multipliers λ_n leads to

$$0 = \frac{\delta}{\delta \hat{F}^{\text{kin}}} \int_0^\infty \mathrm{d}\hat{k} \left[\frac{k_0 \hat{F}^{\text{kin}^2}(\hat{k})}{2w(\hat{k}/k_0)} + \sum_{n=0}^{N} \lambda_n \left(\frac{\hat{k}}{k_0} \right)^n \hat{F}^{\text{kin}}(\hat{k}) \right] , \tag{6.20}$$

from which eq.(6.18) immediately follows.

The cluster of models we work with is shown in figure 6.1. While their moments over the entire space $0 \leq \hat{k} \leq \infty$ are identical by construction, they differ slightly in the shape function region. In order to determine the error to the partial rates caused by the model choice, we use these functions to estimate the uncertainty. Computing the mean and standard deviation, we find that their moments in this region give relative errors of 4.0%, 5.3% and 7.5% for the zeroth, first and second moment respectively, which we judge as reasonable. As per default, we will in the following use the model function with the Gaussian kernel as well as $\alpha = 1$ and $k_0 = 0.9\,\text{GeV}$.

The model with the finite weight function w_{fin} requires a further comment. Its free parameters reside at much higher values as those of the other models. If in particular k_0 is chosen too small, the model will display large fluctuations, due to the sharp cutoff at a relatively small value of k_0. The only possible set of coefficients that may fulfil the moment constraints in such a case for mundane polynomials thus fluctuate strongly, which is an unwanted relic of the weight function choice. We can circumvent the problem however, by choosing a much higher value, in this case $k_0 = 6\,\text{GeV}$, which results in a model function that resembles the form of the others in the cluster. We emphasize that this choice is not arbitrary, because it directly influences the uncertainty estimation of the model choice. If one of the models fluctuates strongly in the low $\hat{k}$ region – even though this does not effect the value for the partial rate for relaxed kinematical cuts – it artificially blows up the error caused by the model choice for stricter cuts.

6.1.4 Compactification

At this point we introduced simple models for $\hat{F}^{\text{kin}}(\hat{k})$ and performed the change to the kinetic scheme via the operator $\mathbf{G}$. We already noted before that the modelling of $\hat{F}^{\text{kin}}(\hat{k})$ may generate fluctuations at higher $\hat{\omega}$, which are unwanted and a mere relic of the modelling process. The left plot in figure 6.2 shows the evolution of the model function for one and two loop order of $\mathbf{G}$. It does not resemble large oscillations in the low $\hat{\omega}$ region, however goes through zero near $2.3\,\text{GeV}$ and oscillates thereafter. Enhancing this effect for a higher moment in $\hat{k}$, this feature is more visible in the right side of the figure.

In order to transition as smoothly as possible from the shape function region to the full OPE, we describe a moment–preserving algorithm that compactifies the model function in such a way that it terminates at some value of $\hat{k} \approx 2\,\text{GeV}$. Like in the case of $\mathbf{G}\hat{F}^{\text{kin}}(\hat{k})$, we need a set of functions to correct for the moments. Again we choose derivatives with respect to $\ln \hat{k}$ and define

$$h_j(\hat{k}) \coloneqq \frac{\hat{k}^j}{j!} \left(\frac{\mathrm{d}}{\mathrm{d}\hat{k}} \right)^j \hat{F}^{\text{kin}}(\hat{k}) \,. \tag{6.21}$$

We need the moments $M^{(j)}_{\text{comp},n}(\kappa)$ of these functions, but this time over the finite interval $\hat{k} \in [0, \kappa]$, keeping the upper limit κ variable. The idea is to use a κ–dependent linear combination of the h_j to build a family of compact functions $F_{\text{comp}}(\hat{k}, \kappa)$, which end in general at a finite value, but all have the same desired moments. This way

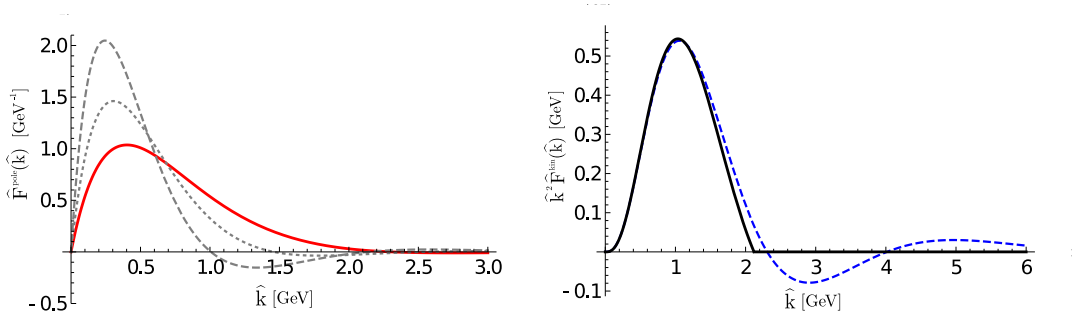

Figure 6.2: Example for the model construction, based on the exponential weight. Left: The solid (red) line is $\hat{F}_{\mathrm{pol}}$ at LO, which is identical to $\hat{F}_{\mathrm{kin}}$. The dotted and dashed (gray) curves are $\hat{F}_{\mathrm{pol}}$ at NLO and NNLO, respectively. Right: The solid (black) function is $\hat{k}^2\mathbf{C}\hat{F}_{\mathrm{kin}}(\hat{k})$, and the dashed (blue) line shows the uncompactified $\hat{k}^2\hat{F}_{\mathrm{kin}}(\hat{k})$.

we preserve all moment relations, but generate a model that necessarily terminates at some endpoint, where the fluctuations start (which is in general different for each chosen model). The compact functions and their moments read

$$\begin{aligned} F_{\mathrm{comp}}(\hat{k},\kappa) &= \theta(\kappa-\hat{k})\sum_j b_j(\kappa)h_j(\hat{k})\,, \\ \int_0^\infty \mathrm{d}\hat{k}\,\hat{k}^n F_{\mathrm{comp}}(\hat{k},\kappa) &= \sum_j b_j(\kappa)M^{(j)}_{\mathrm{comp},n}(\kappa) = M_{\mathrm{kin},n} \quad \forall\kappa\,, \end{aligned} \tag{6.22}$$

where the compact moments are defined as

$$M^{(j)}_{\mathrm{comp},n}(\kappa) = \int_0^\kappa \mathrm{d}\hat{k}\,\hat{k}^n h_j(\hat{k})\,. \tag{6.23}$$

If one of the functions in the family terminates in zero, we identify it as our compactified model. This defines the size of the interval k_c such that

$$F_{\mathrm{comp}}(\kappa,\kappa)\Big|_{\kappa=k_c} = 0\,, \qquad \mathbf{C}\hat{F}_{\mathrm{kin}}(\hat{k}) = F_{\mathrm{comp}}(\hat{k},k_c)\,. \tag{6.24}$$

If there is no zero in $F_{\mathrm{comp}}(\kappa,\kappa)$, the algorithm will not converge in general. Thus, if after several iterations with various values for κ no solution was found, the starting function $\hat{F}^{\mathrm{kin}}(\hat{k})$ was probably positive definite and thus the compactification unnecessary. Altogether, applying the operator $\mathbf{C}$ determines the natural value of $\hat{k}$ at which the model needs to terminate to avoid model relics, while preserving all moment relations.

The effect of the compactification procedure is shown in the right plot of figure 6.2,

where the black solid line is the compactified model. We see that, while preserving all moments of $\hat{F}^{\text{kin}}(\hat{k})$, the model function terminates at some value k_c and shows no oscillations afterwards anymore. It also becomes apparent, that this procedure has almost no effect for the shape function region which is of interest in a V_{ub} determination. In fact, in the above example, we have $b_0(k_c) = 0.998$, $b_1(k_c) = -0.007$ and $b_2(k_c) = -0.013$, which indicates how closely the compactified function follows the uncompactified one in the low $\hat{k}$ region.

Compactifying the full shape function including all effects from its radiative tail is more involved than the method we described in this chapter. In general the operators **G** and **C** do not commute and thus it is necessary to compactify everything order by order. It is clear however, that we can in general get rid of all oscillations outside of the shape function region with the algorithm presented here. For the purpose of partial rate determinations with kinematical cuts, it is unnecessary to alter our model function and thus in the following we will use the simple models presented in chapter 6.1.3 for further considerations.

6.2 Power corrections to the structure functions

In chapter 3.3 we derived the expression for the leading shape function in the light–cone expansion. However, as for the full OPE, there are power corrections for higher powers of $1/m_b$, which we want to include. In contrast to the treatment of inclusive $B \to X_c \ell \bar{\nu}$, there are several sources of these corrections. On the one hand there are corrections that are only suppressed by the inverse mass, because we restrict the phase space to a certain kinematic region. These terms do not introduce any new hadronic quantities and we call them kinematical corrections. On the other hand there are contributions from subleading shape functions, which arise for higher orders in the light–cone expansion. They form the dominant hadronic contributions and, as the leading shape function, need to be modelled. Lastly when relaxing the cuts enough, we require to have a smooth overlap between the shape function region and the full OPE. Since the power counting in both regions is different, there are hadronic corrections, that are present in the full OPE and had not been picked up by the subleading shape functions. These residual hadronic contributions are usually tiny, yet necessary for a consistent treatment.

6.2.1 Kinematical power corrections

The first kind of power corrections we want to introduce are the kinematical corrections. They do not introduce any new hadronic quantities and are suppressed due to the restriction of the variable P_+ to a kinematically suppressed region. Generally speaking, they may be viewed as the power corrections generated by the hard– and jet function in the factorization. As these contributions are generated at the one–loop level, the kinematical corrections are further suppressed by the strong coupling and therefore scale like α_s/m_b. They can be extracted from the one–loop expression derived in [156] and are then convoluted with the shape function. Note that the one–loop expressions from [156] are known for fixed–order perturbation theory and thus do not inherit any RGE evolution factor. Since the Sudakov exponents would be the same as for the leading power terms, we may estimate that the scale evolution only introduces effects well below 1 %. Hence, we assign the intermediate scale μ_i to the strong coupling appearing in these terms without further RGE running.

The expressions for the structure functions have been determined in [21] – we list them here for completeness:

$$
\begin{aligned}
f_1^{\text{kin}}(P_+,y) &= \frac{1}{m_B-P_+}\,\frac{C_F\alpha_s(\mu_i)}{4\pi}\int_0^{P_+}\!\mathrm{d}\hat{k}\,\hat{S}(\hat{k}) \\
&\quad\times\left[\frac{f_1(x,y)}{(1+x)^2y(x+y)}-\frac{2g_1(x,y)}{x(1+x)^2y^2(x+y)}\ln\left(1+\frac{y}{x}\right)-\frac{4}{x}\ln\left(y+\frac{y}{x}\right)\right], \\
f_2^{\text{kin}}(P_+,y) &= \frac{1}{m_B-P_+}\,\frac{C_F\alpha_s(\mu_i)}{4\pi}\int_0^{P_+}\!\mathrm{d}\hat{k}\,\hat{S}(\hat{k}) \\
&\quad\times\left[\frac{f_2(x,y)}{(1+x)^2y^2(x+y)}-\frac{2x\,g_2(x,y)}{(1+x)^2y^3(x+y)}\ln\left(1+\frac{y}{x}\right)\right], \\
f_3^{\text{kin}}(P_+,y) &= \frac{1}{m_B-P_+}\,\frac{C_F\alpha_s(\mu_i)}{4\pi}\int_0^{P_+}\!\mathrm{d}\hat{k}\,\hat{S}(\hat{k}) \\
&\quad\times\left[\frac{f_3(x,y)}{(1+x)^2y^3(x+y)}+\frac{2g_3(x,y)}{(1+x)^2y^4(x+y)}\ln\left(1+\frac{y}{x}\right)\right],
\end{aligned}
\tag{6.25}
$$

where the variable $x \coloneqq \frac{P_+ - \hat{k}}{m_B - P_+}$ and the functions $f_i(x)$ and $g_i(x)$ are given by

$$\begin{aligned}
f_1(x,y) &= -9y + 10y^2 + x(-16 + 12y + 6y^2) + x^2(13y - 12)\,, \\
g_1(x,y) &= -2y^3 - 2xy^2(4+y) - x^2y(12 + 4y + y^2) - 4x^3(y+2) + 3x^4(y-2)\,, \\
f_2(x,y) &= y^2 + xy(8 + 4y + y^2) + 3x^2y(10 + y) + x^3(12 + 19y) + 10x^4\,, \\
g_2(x,y) &= 2y^2 + 4xy(1+2y) + x^2y(18 + 5y) + 6x^3(1+2y) + 5x^4\,, \\
f_3(x,y) &= 2y^3(2y - 11) + xy^2(-94 + 29y + 2y^2) + 2x^2y(-72 + 18y + 13y^2) \\
&\quad + x^3(-72 - 42y + 70y^2 - 3y^3) - 10x^4(6 - 6y + y^2)\,, \\
g_3(x,y) &= 4y^4 - 6x(y-5)y^3 - 4x^2y^2(-20 + 6y + y^2) + x^3y(90 - 10y - 28y^2 + y^3) \\
&\quad + x^4(36 + 36y - 50y^2 + 4y^3) + 5x^5(6 - 6y + y^2)\,.
\end{aligned} \tag{6.26}$$

The above contributions give the correct $\mathcal{O}(\alpha_s)$ corrections to the total rate, when integrated over the full phase space. In the shape function region, where $P_+ \ll P_-$ they are (strongly) suppressed and can be expanded in inverse powers of $m_B - P_+$. This makes it easier to compare them order by order with the hadronic power corrections, but has the downside that singularities in y are introduced, which need to be treated specifically [21]. Thus, we refrain from such an expansion and use the full results in the following.

6.2.2 Subleading shape function contributions

The dominant hadronic correction in the shape function region is given by the subleading shape functions. By going to higher orders in the light–cone expansion from chapter 3.3.2, one finds a new class of non–local matrix elements, which give rise to a set of non–perturbative, subleading shape functions at order $1/m_b$ [53, 54, 55, 157]. Equivalently these functions can also be derived in SCET [56, 158, 159], where they take the same form than in the light–cone expansion, as was shown in [21, 56].

In principle the subleading shape functions are treated in the same way than the leading shape function: with the help of moment relations to local matrix element, their modelled functional form can be constrained. Apart from their first few moments, little is known about the subleading shape functions. In particular it is unnecessary to perform any RG evolution for them, because corrections from these procedures of order $\mathcal{O}(\alpha_s/m_b)$ or higher and can safely be neglected. Note that these corrections are parametrically of the same order as the ones from the kinematical corrections in chapter 6.2.1. The difference is that the kinematical corrections are enhanced in some

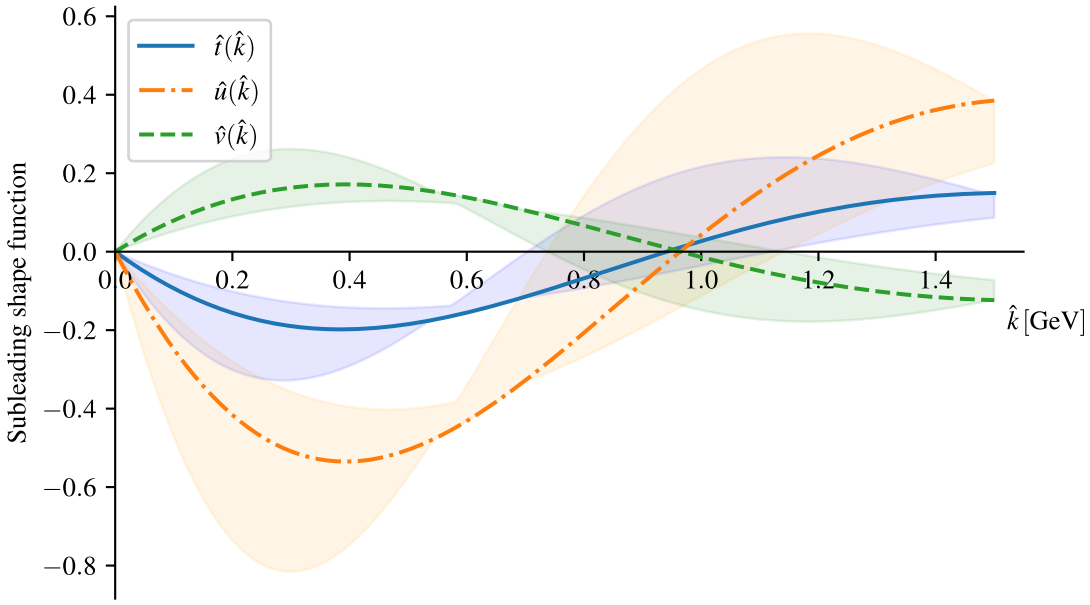

Figure 6.3: The subleading shape functions $\hat{t}(\hat{k}), \hat{u}(\hat{k})$ and $\hat{v}(\hat{k})$ for a Gaussian kernel with $\alpha = 1$. The coloured bands show the variation of k_0 between $[1\,\text{GeV}, 1.8\,\text{GeV}]$ and the continuous lines have $k_0 = 1.5\,\text{GeV}$ fixed.

parts of phase space and might pose a viable addition to the partial rate this way, while the RG evolution corrections are in general already small without any $1/m_b$ suppression.

Adopting the notation from [21, 56], the relevant subleading shape functions at tree level $\hat{t}(\hat{k}), \hat{u}(\hat{k})$ and $\hat{v}(\hat{k})$ are incorporated into our structure functions by [21]

$$\begin{aligned} f_1^{(1)}(P_+, y) &= \frac{1}{m_B - P_+}\left((\bar{\Lambda} - P_+)\,\hat{S}(P_+) + \hat{t}(P_+) + \frac{\hat{u}(P_+) - \hat{v}(P_+)}{y}\right), \\ f_3^{(1)}(P_+, y) &= \frac{1}{m_B - P_+}\frac{2}{y}\left(-(\bar{\Lambda} - P_+)\,\hat{S}(P_+) - 2\hat{t}(P_+) + \frac{\hat{t}(P_+) + \hat{v}(P_+)}{y}\right). \end{aligned} \tag{6.27}$$

In [54, 157] moment relations similar to the ones for the leading shape function were found. The zeroth moment of the subleading shape functions always vanishes (which is a consequence of Luke's theorem again). The higher moments of the unshifted subleading shape functions are further given by relations to the local matrix elements

of the full OPE

$$t(k) = \frac{\mu_G^2}{3}\,\delta'(k) + \frac{\rho_{\rm LS}^3}{6}\delta''(k)\,, \quad u(k) = \frac{2\mu_\pi^2}{3}\,\delta'(k)\,, \quad v(k) = -\frac{\mu_G^2}{3}\,\delta'(k)\,. \tag{6.28}$$

which we may now use in the same way as in chapter 6.1 to derive a functional form. In former attempts like [21, 56] the derivative of the leading shape function was used as a model ansatz and then modified with functions that do not contribute to the moments. There is, however, no known connection between the non–local matrix elements at leading and subleading order and consequently they should be treated as independently. We thus model the subleading contributions as we had done for the leading shape function. That is, we use the ansatz from eq.(6.18) and tune the coefficients of the polynomial to the moment relations above. As the subleading contributions are only very weakly constraint by their moments, we do not choose different weight functions or onsets here, but merely derive one overall form for each of the three contributions. We will, however, still test the model dependence by varying the freely choosable parameter k_0.

The result of the modelling is shown in figure 6.3, where we depict the three models for the Gaussian weight with $\alpha = 1$ and $k_0 = 1.5\,\text{GeV}$ for the continuous lines. The error bands show the variation of the subleading models between $k_0 \in [1\,\text{GeV}, 1.8\,\text{GeV}]$. Note that we obtained this range by introducing an unknown third moment and varying it between zero and one. The knowledge on the first few moments constraints the subleading models very weakly, which in turn will be reflected in the uncertainty for the partial rates that we investigate in chapter 6.3.2. As our default, we choose the upper limit of this range $k_0 = 1.8\,\text{GeV}$, since the fluctuations of the subleading shape functions are reduced then and their effect is milder on the central value for the partial rates. Nonetheless we will include the full range of possible k_0 values into our error analysis in chapter 6.3.2.

We observe that the overall subleading contribution will reduce the value of the partial rates especially for the shape function region, where P_+ is small. If integrated over the full phase space, their contribution is fully determined by the moments of the local OPE and thus such local effects may play an important role especially for more restrictive kinematical cuts. Furthermore all three subleading shape functions inherit oscillations, which is due to their vanishing zeroth moment.

6.2.3 Residual hadronic corrections

At order $1/m_b^2$ a new set of subsubleading shape functions enters, about which only very sparse information exist. In the low P_+ region it suffices to absorb most of their effects into the subleading shape functions. When the subsubleading shape functions are integrated over the major part of phase space, their contributions are distinct. While the norm of the subleading shape functions vanishes then, this need not be true for the subsubleading ones, as matrix elements of the local OPE at $1/m_b^2$ emerge. To include such contributions, one first identifies all terms in the local OPE [160] and converts them into the (v, n) basis. Subsequently the leading and subleading shape functions are expanded in their moments, such that by subtracting both results the contributions from the local OPE at $\mathcal{O}(1/m_b^2)$ remain. The result of these manipulations was derived in [21] and reads

$$\begin{aligned} f_1^{(2)}(P_+, y) &= \frac{1}{(m_B - P_+)^2} \left(\frac{-4\mu_\pi^2 - 2\mu_G^2}{3y^2} + \frac{\mu_\pi^2 - \mu_G^2}{3} \right) \hat{S}(P_+)\,, \\ f_2^{(2)}(P_+, y) &= \frac{1}{(m_B - P_+)^2} \left(\frac{2\mu_\pi^2 + \mu_G^2}{3y^2} \right) \hat{S}(P_+)\,, \\ f_3^{(2)}(P_+, y) &= \frac{1}{(m_B - P_+)^2} \left(\frac{-4\mu_\pi^2 + 8\mu_G^2}{3y^2} + \frac{4\mu_\pi^2 - 3\mu_G^2}{3y} \right) \hat{S}(P_+)\,. \end{aligned} \tag{6.29}$$

These terms together with eq.(6.27) account for all known first and second–order contributions, both in the shape function and local OPE region. In addition, further corrections from $1/m_b^3$ terms are expected to be tiny [21], which coincides with our numerical findings in chapter 6.3. Besides, terms at this order can only consistently be applied, by introducing higher order corrections in the transition of hadronic and partonic kinematic variables. Such a procedure lies beyond the scope of this analysis and hence we neglect all contributions of terms $\sim 1/m_b^3$.

6.3 Numerical evaluation of partial rates

Having defined all perturbative and non–perturbative ingredients for the structure functions, we are now ready to numerically evaluate predictions for the partial rate Γ_u with various kinematical cuts. The values for the masses m_b and m_B as well as all relevant HQE parameters are updated compared to the ones used in chapter 5, because [112] was published during the course of this thesis. For convenience, we reference the newer values in table 6.1. The parameter $\bar{\Lambda}^{\text{kin}}$ is not accessible by experiment and thus

m_b	$(4.573 \pm 0.012)\,\text{GeV}$
m_B	$(5.2793 \pm 0.00012)\,\text{GeV}$
μ_π^2	$(0.477 \pm 0.056)\,\text{GeV}^2$
μ_G^2	$(0.306 \pm 0.05)\,\text{GeV}^2$
ρ_D^3	$(0.185 \pm 0.031)\,\text{GeV}^3$
ρ_{LS}^3	$(-0.130 \pm 0.092)\,\text{GeV}^3$
$\alpha_s(m_b)$	0.218

Table 6.1: Default inputs for the masses and HQE parameters for the numerical analysis of chapter 6.3. All values are taken from [112], except for the meson mass m_B, which was taken from [26]. The value for the strong coupling α_s is obtained with `RunDec` with four–loop accuracy [141, 142].

we use eq.(3.68) to fix it in terms of m_b, μ_π^2 and μ_G^2. Note that this reinforces the dependence on m_b, as it formerly only appeared in logarithms of the hard function. In addition we choose the default values for the different scales as $\mu_0^{\text{def}} = 1.3\,\text{GeV}$, $\mu_i^{\text{def}} = 1.5\,\text{GeV}$ and $\mu_h^{\text{def}} = 3\,\text{GeV}$, respectively. The soft scale lies very close to the intermediate one, as it must be large enough to trust perturbative results. The hard scale is generally of order $\sim m_b$, however in perturbative logarithms it appears in the combination (ym_b/μ_h) and thus we are guided by the average $\langle y \rangle m_b \approx 3\,\text{GeV}$ here.

Further note that we have to reexpand the leading power structure functions simultaneously in the strong coupling at the different scales. Parametrically the different scales can be treated identically for the sake of power counting and thus the reexpansion gets rid of any artificial contributions of $\mathcal{O}(\alpha_s^3)$ from the product of the hard and jet functions as well as the RG coefficient. The shape function also contains terms $\sim \alpha_s(\mu_0)$ from the transition to the kinetic scheme. However, since the shape function is fully non–perturbative, we do not expand it together with the other terms but instead neglect all terms $\mathcal{O}(\alpha_s^3)$ in it separately.

For illustrative purposes we perform all default analyses in this chapter with the leading and subleading shape function with the Gaussian kernel and the aforementioned model parameters. In section 6.3.2 we vary the model contributions with the other obtained models, to determine the uncertainty on the partial rates.

6.3.1 Double differential rate

The methods we utilized for the calculation of the partial rates are optimized for the shape function region. Nonetheless it is instructive to also study some of the

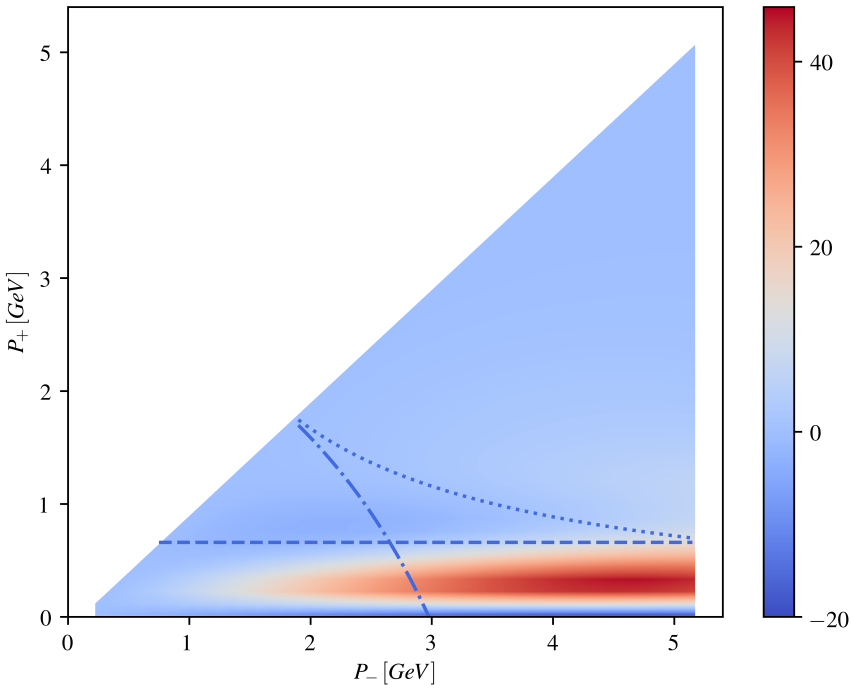

Figure 6.4: The double differential rate of eq.(6.30) with all power corrections and the default Gaussian kernel for the leading and subleading shape function. Standard cuts on $P_+ \leq m_D^2/m_B$ (dashed), $m_X \leq m_D$ (dotted) and $q^2 \geq (m_B - m_D)^2$ (dashed–dotted) are depicted in the double differential rate.

differential spectra, to analyze local effects for different values of P_+ and P_-. The double differential rate in those two variables is obtained by integrating eq.(3.39) over the lepton momentum P_ℓ in the range $P_+ \leq P_\ell \leq P_-$, which yields

$$\begin{aligned}\frac{\mathrm{d}^2\Gamma_u}{\mathrm{d}P_+\mathrm{d}P_-} =& \frac{G_F^2|V_{ub}|^2}{96\pi^3}(m_B - P_+)(P_- - P_+)^2 \\ &\times \left[(3m_B - 2P_- - P_+)f_1 + 6(m_B - P_-)f_2 + (P_- - P_+)f_3\right].\end{aligned} \tag{6.30}$$

In figure 6.4 we show the resulting spectrum for our input of the structure functions. Most of the events that are generated with this procedure lie in the region where $P_+ \ll P_-$. This phase space slice is quite narrow and therefore relaxing kinematical cuts will only have a small effect on the resulting partial rates. We observe that the NLO and NNLO corrections to the leading structure function clench this region. Below there is a very small patch, where the rate becomes negative, which is a relic of the scheme change in the shape function. Since cuts are never applied to the $P_+ \ll P_-$

region, this does not alter the partial rate in any significant way. Above the populated region, there is another patch, where the rate becomes slightly negative too. This effect is caused by the modelling of the subleading shape functions. Fortunately this region is relatively small and does not exhibit large rates. Thus after integrating over the hadronic momenta, the rates will yield positive results and no unphysical effects remain.

In the same figure we also indicated different kinematical cuts. We see that we can include most of the events by employing a cut on the hadronic momentum $P_+ \leq \Delta_P$ with the ideal cut $\Delta_P = m_D^2/m_B \approx 0.66\,\text{GeV}$. Note that cuts on P_+ in general probe the same hadronic phase space as cuts on the lepton energy E_ℓ, however with a much better efficiency, as was shown in [20]. In addition such cuts also get rid of the slightly negative patch, which would be included with cuts on the hadronic invariant mass m_X, which is in general unwanted. Combining this with a loose cut on q^2 removes the region, where both P_+ and P_- are small. In this part of phase space weak annihilation contributions are expected to play an important role, which cannot be described with our framework [20, 21]. With the software package, we developed with this thesis [12] it is possible to apply restrictions on all of the above observables at the same time, allowing for the most efficient extraction of phase space.

6.3.2 Error analysis of the partial rates

We account for several sources of theoretical uncertainties in the determination of the partial rates. First, there are uncertainties on the parameter inputs we use. We depict all numerical values for the HQE parameters and their uncertainty in table 6.1. We vary the mass m_b as well as the HQE parameters μ_π^2 and ρ_D^3 in the range of their uncertainties. Since we determine $\bar{\Lambda}$ in terms of these parameters, we account for its uncertainty indirectly by their variation. In addition we determine the uncertainty from unknown higher order perturbative corrections by varying the hard and intermediate scale μ_h and μ_i between their default values via $\mu_h^{\text{def}}/\sqrt{2} \leq \mu_h \leq \sqrt{2}\mu_h^{\text{def}}$ and $\mu_0^{\text{def}} \leq \mu_i \leq \sqrt{2}\mu_i^{\text{def}}$ respectively. The lower limit on the μ_i variation is chosen such that we do not enter any non–perturbative regimes. Finally we include uncertainties from the choice of the model for the leading shape function, by taking the mean of the spread of the five models introduced in chapter 6.1. To estimate the uncertainty caused by the model choice of the subleading shape functions, we vary the parameter k_0 between $1.0\,\text{GeV} \leq k_0 \leq 1.8\,\text{GeV}$, where the range is determined by varying the next unknown moment in the subleading shape functions and fixing k_0 with it. Finally we take the

mean of the deviation from the central partial rates as the symmetrical uncertainty. All error sources are finally added in quadrature to obtain the final uncertainty on the partial rate.

To study the impact of the different sources of uncertainty, we show the partial rate for three examplary kinematical cuts, where we display the various contributions to the uncertainty explicitly. For the standard cut on the hadronic momentum $P_+ \leq 0.66\,\text{GeV}$ we find in units of $|V_{ub}|^2\,\text{ps}^{-1}$

$$\begin{aligned}\Gamma_u &= 43.49\ {}^{+1.73}_{-2.02}\big|_{\mu_h}\ {}^{-0.38}_{-1.01}\big|_{\mu_i}\ {}^{+1.02}_{-1.10}\big|_{m_b}\ {}^{-0.24}_{-0.73}\big|_{\mu_\pi^2}\ {}^{+0.13}_{-0.01}\big|_{\rho_D^3}\ {}^{+0.97}_{-0.97}\big|_{\text{SF}}\ {}^{+3.54}_{-3.54}\big|_{\text{SSF}} \\ &= 43.49\ {}^{+4.22}_{-4.51}\,,\end{aligned} \tag{6.31}$$

where SF and SSF denote the uncertainties caused by the leading and subleading shape functions respectively. For a cut on the hadronic invariant mass $m_X \leq 1.7\,\text{GeV}$ the uncertainties read

$$\begin{aligned}\Gamma_u &= 42.52\ {}^{+1.08}_{-2.02}\big|_{\mu_h}\ {}^{+0.38}_{-0.68}\big|_{\mu_i}\ {}^{+0.95}_{-0.97}\big|_{m_b}\ {}^{-0.22}_{-0.08}\big|_{\mu_\pi^2}\ {}^{+0.09}_{-0.02}\big|_{\rho_D^3}\ {}^{+0.78}_{-0.78}\big|_{\text{SF}}\ {}^{+3.24}_{-3.24}\big|_{\text{SSF}} \\ &= 42.52\ {}^{+3.66}_{-4.07}\,,\end{aligned} \tag{6.32}$$

and finally for a cut on the lepton energy $E_\ell \geq 2.31\,\text{GeV}$ we find

$$\begin{aligned}\Gamma_u &= 5.07\ {}^{+0.53}_{-0.52}\big|_{\mu_h}\ {}^{+0.21}_{-0.65}\big|_{\mu_i}\ {}^{+0.34}_{-0.34}\big|_{m_b}\ {}^{-0.18}_{-0.19}\big|_{\mu_\pi^2}\ {}^{+0.05}_{-0.06}\big|_{\rho_D^3}\ {}^{+0.12}_{-0.12}\big|_{\text{SF}}\ {}^{+0.93}_{-0.93}\big|_{\text{SSF}} \\ &= 5.07\ {}^{+1.16}_{-1.31}\,.\end{aligned} \tag{6.33}$$

Overall we see that the uncertainties give about the same contribution for the different kinematical cuts. If cuts are chosen more restrictive, as in the case of the lepton energy E_ℓ, the proportion of the model uncertainty is larger. This is expected, as for an integration over the full phase space, only the moments of shape function contribute and thus all model dependence vanishes. In turn a more restrictive cut can potentially enhance the dependence on the model.

As expected, the uncertainty caused by the model dependence from the (sub)leading shape functions is the dominant source of uncertainty. In particular the subleading shape functions, about which less information is available, cause a larger uncertainty than the leading ones. We emphasize that different ways of varying the model parameters may yield slightly smaller or larger model uncertainties. Since we probe a large space of different models with our variation, the lack of knowledge about the model should be well incorporated in our uncertainty estimate.

We observe that a large part of the uncertainty is due to the variation of the hard

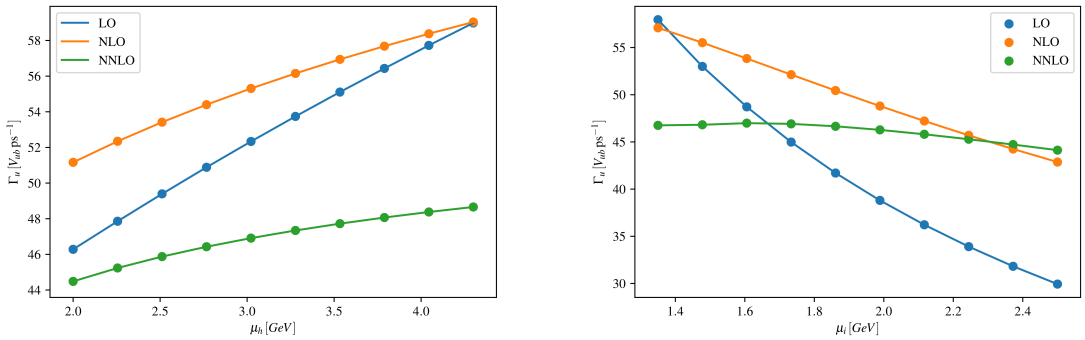

Figure 6.5: Dependence of the partial rates Γ_u on the hard and intermediate scale μ_h and μ_i.

and intermediate scale μ_h and μ_i, respectively. In figure 6.5 we depict the dependence of the partial rate on μ_h and μ_i at LO, NLO and NNLO. The dependence on the scale attenuates for growing orders in α_s, which shows the importance of the NNLO results for a precise determination. In turn, including these contributions reduces the uncertainty caused by the scale variation.

Finally there is a relatively strong dependence on the quark mass m_b. Its uncertainty is strongly enhanced by the appearance in $\bar{\Lambda}$, since it is absent as a phase space factor for our choice of hadronic variables and otherwise m_b solely emerges in logarithms of the perturbative corrections in the hard functions. We note that the error caused by the variation of μ_π^2 and ρ_D^3 is relatively small. In addition ρ_D^3 is not present in $\bar{\Lambda}$ to the order we are working at, which further reduces the dependence on it.

6.3.3 Partial rates with kinematical cuts

The partial rates are obtained by further integrating eq.(A.14) over the hadronic variable P_+. In appendix A.4 we show the algorithm that is used to employ cuts on various observables, like the hadronic invariant mass m_X, the lepton energy E_ℓ, the lepton invariant mass q^2 and the hadronic jet momentum P_+ or combinations thereof. Experimentally cuts on certain variables are favoured, on the one hand due to the reduction of the charm background and on the other due to the restrictions of the detector.

In table 6.2 we show the resulting partial rates, with the different contributions for several cut combinations. Overall we observe the importance of the kinematical and subleading power corrections, which pose a contribution to the total rate of well about 10 %. In addition we can nicely see the convergence of the OPE as the residual hadronic

Cut [GeV]	LO	NLO	NNLO	Kin.	Subl. SF	Res. Had.	Total
$P_+ \leq 0.66$	55.28	3.02	-8.36	5.64	-7.89	-0.83	$46.88^{+4.22}_{-4.51}$
$m_X \leq 1.7$	60.90	-2.78	-10.91	7.80	-9.00	-0.99	$45.03^{+3.66}_{-4.07}$
$E_\ell \geq 2.31$	5.22	1.93	0.30	0.60	-1.13	-0.68	$6.24^{+1.16}_{-1.31}$
$q^2 \geq 8$	30.56	-4.85	-5.69	6.21	-5.19	-0.64	$20.36^{+2.04}_{-2.23}$
$P_+ \leq 0.66, E_\ell \geq 1$	49.44	3.26	-7.33	5.11	-7.33	-0.87	$42.28^{+3.54}_{-4.07}$
$m_X \leq 1.7, E_\ell \geq 1$	55.78	-2.82	-10.18	7.34	-8.46	-1.04	$40.62^{+3.21}_{-3.87}$
$m_X \leq 1.7, q^2 \geq 8$	29.34	-2.48	- 5.92	4.89	-5.65	-0.60	$19.47^{+1.98}_{-2.31}$
$m_X \leq 1.7, E_\ell \geq 1, q^2 \geq 8$	29.19	-2.48	-5.91	4.88	-5.65	-0.62	$19.42^{+1.68}_{-2.17}$

Table 6.2: Partial rates for various (combined) kinematical cuts given in units of $|V_{ub}|^2\,\mathrm{ps}^{-1}$ and resolved for their different contributions. In order they are listed as leading order, NLO and NNLO corrections for the perturbative– and kinematical, subleading and residual hadronic contributions for the power corrections.

corrections $\sim 1/m_b^2$ are about a magnitude smaller than the subleading contributions. It is also noteworthy that the NNLO contributions play a very important role for the partial rates and denote a larger addition than the NLO ones. For some cuts they reduce the leading order value by almost 15 %. All of these contributions are included in our software package [12], which greatly simplifies the comparison of experimental results with these predictions.

Traditionally the most common variable to discriminate against the charm background is the lepton energy E_ℓ. By requiring the lepton energy to be larger than $(m_B^2 - m_D^2)/2m_B \approx 2.31\,\mathrm{GeV}$, the invariant mass of the hadronic final state is restricted to be smaller than m_D. Thus, employing this ideal cut yields a complete reduction of the charm background. The downside of using it lies in its restrictiveness. Not only is the full charm background reduced, but in turn a large amount of other events are also cut out. It was shown in [20, 21] that the efficiency of cuts on E_ℓ is much worse than on the hadronic variables. This can also be seen in table 6.2, where the overall value of the partial rate with the above–mentioned E_ℓ cut is much smaller than for example the equivalent cut on the hadronic momentum. We also see that for this particular value, the contributions from the subleading shape functions are very strong, which has also increased the uncertainty as we saw in the previous chapter.

In contrast we may also employ a comparable cut on the hadronic variable P_+, which samples the same phase space than a cut on E_ℓ. The ideal separator for this case is $P_+ \leq m_D^2/m_B^2 = 0.66\,\mathrm{GeV}$. We already saw in the differential rate depicted in

figure 6.4 that this cut samples almost all events in the spectrum; this can also be seen in the resulting partial rate. It is much larger than the rate with a lepton energy cut and thus a better discriminator against the charm background. Compared to the cut on the hadronic invariant mass $m_X \leq 1.7\,\mathrm{GeV}$, the rate for the P_+ cut is even larger in its central value. This seems counterintuitive at first glance, but can be understood by considering the effects of especially the NLO contribution. They quench the spectrum in such a way that most of the events lie in a narrow patch at low P_+. This happens by a strong positive enhancement at very low P_+ and a negative contributions directly above. The cut on m_X samples the negative contributions more strongly, causing a sign change that we observe in table 6.2. Thus the central value for this cut is smaller than the more restrictive P_+ cut, however they are fully consistent in the range of their uncertainties.

In order to enhance the precision, it is interesting to determine partial rates with combinations of different cuts. To that end, we give some samples of different cut combinations in table 6.2 as well. This serves to show that the software package developed for this chapter [12] can produce values for various phase space restrictions which can be compared directly with experimental predictions.

Finally, we use the partial rate for the combined cut on the hadronic invariant mass and lepton energy, $m_X \leq 1.7\,\mathrm{GeV}$ and $E_\ell \geq 1\,\mathrm{GeV}$, from table 6.2 to determine a preliminary value of $|V_{ub}|$. In [143] the most recent value for the branching fraction $\mathcal{B}(B \to X_u \ell \nu)$ was measured by the Belle collaboration. For the aforementioned kinematical cuts, it was determined to be $\mathcal{B}(B \to X_u \ell \nu) = (1.09 \pm 0.05 \pm 0.08) \cdot 10^{-3}$, where the uncertainties denote the statistical and systematical uncertainties, respectively. A value for $|V_{ub}|$ can be determined with our partial rates by

$$|V_{ub}| = \sqrt{\frac{\mathcal{B}(B \to X_u \ell \nu)}{\tau_B \cdot \Gamma_u(B \to X_u \ell \nu)}}\,, \tag{6.34}$$

where $\tau_B = (1.579 \pm 0.004)$ ps [26] is the B meson life time. Using the value for the partial rate $\Gamma_u = 40.62^{+3.21}_{-3.87}\,\mathrm{ps}^{-1}$, we obtain

$$|V_{ub}| = \left(4.12 \pm 0.09\big|_{\text{stat.}} \pm 0.15\big|_{\text{sys.}}\, {}^{+0.16}_{-0.19}\big|_{\text{theo.}}\right) \cdot 10^{-3} = \left(4.12\, {}^{+0.24}_{-0.26}\right) \cdot 10^{-3}\,, \tag{6.35}$$

where the uncertainties denote the statistical, systematical and theory uncertainty respectively and the total was obtained by adding the individual errors in quadrature. We note that the central value in eq.(6.35) is slightly larger than the ones found in [143] for this specific cut, but is fully consistent in the range of its error and with

the value averaged over all kinematical cuts. The enhancement compared with their previous value of BLNP [143], $|V_{ub}|_{\mathrm{BLNP}} = (3.90 \pm 0.21) \cdot 10^{-3}$, is most probably due to the inclusion of NNLO corrections, which were not included previously. It was already found in [58] that these corrections reduce the partial rates significantly, which in turn enhances the value for $|V_{ub}|$. In addition, this reduces the uncertainty from the variation of the scales μ_h and μ_i such that the final theory error is also slightly smaller than the previous one. Finally our value eq.(6.35) is significantly lower than the inclusive world average from eq.(6.1) and thus reduces tension with the exclusive determination.

Conclusion

The study of semi– and non–leptonic decays of B mesons offers a broad spectrum for testing the CKM sector of the standard model. With the newly acquired experimental data from the B factories, pushing the precision of B physics from the theoretical side has become one of the prime objectives in current particle physics research. Clearly, the provision of the theoretical predictions to the experimental collaborations in a usable and implementable manner, is one of the paramount issues in reaching the maximum precision. In this thesis, we have built this bridge between theory and experiment for three decay channels of the B meson; the inclusive semileptonic $B \to X_c \ell \bar{\nu}$ and $B \to X_u \ell \bar{\nu}$ as well as the non–leptonic decay $B \to \pi\pi\pi$.

In the first three chapters of the thesis, we laid the foundations for the applications to the specific decays. In this, we gave a short introduction into the flavour sector of the standard model and the concept of CP violation, which was followed by an overview over Effective Field Theories – in particular the Weak Effective Theory and Heavy Quark Effective Theory. Furthermore we introduced the theoretical basis for the treatment of inclusive semileptonic decays. This involved the disentanglement of perturbative and non–perturbative physics with an Operator Product Expansion and a discussion about the respective occurring matrix elements. We showed that the local matrix elements in the case $B \to X_c \ell \bar{\nu}$ can be connected in between orders by exploiting the invariance under reparameterization. In contrast we discussed the non–local matrix elements in the decay $B \to X_u \ell \bar{\nu}$ and how a factorization theorem, derived in the Soft Collinear Effective Theory, separates contributions at different energy scales. Finally we motivated the use of different mass schemes to enable a more controlled convergence of the perturbative results. Alongside we introduced the kinetic mass scheme, which enhanced the precision of our predictions even further.

The first application of these methods, was the study of CP violation in the non–

leptonic three body decay $B \to \pi\pi\pi$. Since currently all amplitude analyses are performed in variables that are unrelated to the underlying physical process, we encouraged to perform future fits with amplitudes that are directly related to the operators of the quarks involved. Moreover, the strong phase, which drives the CP violation in this process, is solely generated with resonance contributions, usually modelled in the Breit–Wigner form. We pointed out how such a parameterization is not sufficient to describe the experimental findings in the CP landscape and therefore introduced a new parameterization of charm–loop effects. We showed that this parameterization is able to generate large structures in the CP plane, while at the same time being simple to implement in existing amplitude models. Furthermore it is not limited to the process at hand, but can be easily extended for general non–leptonic three body decays, for example into three kaons or a combination of kaons and pions.

Secondly, we investigated the inclusive semileptonic decay $B \to X_c \ell \bar{\nu}$. Exploiting the invariance under reparameterization enabled us to reduce the number of independent local matrix elements that need to be fixed with experimental data from thirteen down to only eight up to $\mathcal{O}(1/m_b^4)$ in the Heavy Quark Expansion. Since an analysis of this reduced set of parameters can only be attempted with experimental observables that share the aforementioned invariance, we used to newest data of the Belle and Belle II collaboration to analyze the moments of the leptonic invariant mass q^2 for the first time. To that end we developed a software package [11], which includes all state–of–the–art corrections to the theoretical prediction of the total rate and the q^2 moments, while only depending on the reduced set of HQE parameters. By employing a novel fit, we determined V_{cb} fully data–driven to $\mathcal{O}(1/m_b^4)$ for the first time as

$$|V_{cb}| = \left(41.69 \pm 0.59\big|_{\text{fit}} \pm 0.23\big|_{\text{h.o.}}\right) \cdot 10^{-3} = (41.69 \pm 0.63) \cdot 10^{-3}\,. \tag{6.36}$$

This value is fully consistent with the former value of $|V_{cb}| = (42.16 \pm 0.51) \cdot 10^{-3}$, which was found using hadronic invariant mass and lepton energy moments [112]. Alongside this main result, we also studied the correlation of the different HQE parameters and determined the ones our fit was sensitive to: ρ_D^3, r_E^4 and r_G^4.

Future improvements of our analysis include higher perturbative corrections to the q^2 moments, since the NNLO corrections to the partonic and NLO corrections to the HQE parameters are currently not implemented. It would also be interesting to use the full range of available spectra, i.e. the lepton energy, hadronic invariant mass and leptonic invariant mass moments for a full investigation of V_{cb} even though it is not possible to use the RPI reduced set of parameters then.

Finally we studied the inclusive semileptonic decay $B \to X_u \ell \bar{\nu}$. In contrast to the inclusive $b \to c$ decays, it is necessary to apply strong kinematical cuts here, as otherwise the CKM favoured $B \to X_c \ell \bar{\nu}$ decays overshadow the experimental signal. In the region of interest in phase space, the OPE features non–local matrix elements – the shape functions – which are not accessible with current theoretical methods. Therefore we developed a novel approach to model them, while taking into account all available information on their moments and perturbative behaviour. In addition we included all known information on the (non–local) power corrections up to $\sim 1/m_b^2$, as well as the perturbative pieces up to NNLO in the software package we developed for this purpose [12]. Several of the results we employed have been available for some time already, but were never used in experimental investigations. We numerically evaluated the resulting partial rates for various kinematical cuts and performed an elaborate error analysis of the values to subsequently determine a preliminary value for V_{ub}, which reads

$$|V_{ub}| = \left(4.12 \pm 0.09\big|_{\text{stat.}} \pm 0.15\big|_{\text{sys.}}{}^{+0.16}_{-0.19}\big|_{\text{theo.}}\right) \cdot 10^{-3} = \left(4.12\,{}^{+0.24}_{-0.26}\right) \cdot 10^{-3}\,. \qquad (6.37)$$

This value coincides well with the overall average, that was obtained in [143], which reads $|V_{ub}| = (4.10 \pm 0.28) \cdot 10^{-3}$.

We emphasize that the value presented here is preliminary and a full analysis including the experimental results for various kinematical cuts is necessary for a full determination of V_{ub}. We also observed that the uncertainty on the theoretical error is dominated by the contribution of subleading shape functions. Thus it is desirable to enhance the precision on these objects further in the future, either by including more moments in their determination or by gathering more information on them with novel methods.

The investigation of precision phenomena in the flavour sector denotes one of the most fruitful branches of the current particle physics research and with ever–increasing amounts of data, more sophisticated and precise predictions will remain a major part of research in probing the limits of the Standard Model.

Appendix

We give all perturbative quantities in this appendix in terms of the SU(N) colour factors where we follow the convention

$$\frac{d_A^{abcd}d_A^{abcd}}{N_A} = \frac{N^2(N^2+36)}{24}\,, \quad \frac{d_F^{abcd}d_A^{abcd}}{N_A} = \frac{N(N^2+6)}{48}\,, \quad \frac{d_F^{abcd}d_F^{abcd}}{N_A} = \frac{N^4-6N^2+18}{96N^2}\,,$$
$$T_F = \frac{1}{2}\,, \quad C_A = N\,, \quad C_F = \frac{N^2-1}{2N}\,, \quad N_A = N^2-1\,, \quad N_F = N\,. \tag{A.1}$$

Here N is the number of colours (in this thesis $N = 3$), N_F and N_A are the dimensions of the fundamental and adjoint representation respectively and n_f is the number of active quark flavours (if not denoted otherwise we use $n_f = 4$).

A.1 The hard, jet and soft functions

We give the perturbative expansions for the hard, jet and soft–partonic functions. The hard functions are extremely lengthy and thus we refer to [67] for the NNLO contributions. In terms of the quantities $H_{ij} = C_iC_j$, the H_{ui} read

$$H_{u1} = H_{11}, \qquad H_{u2} = 0, \qquad H_{u3} = \frac{2H_{13}+H_{33}}{y} + H_{12} + H_{23} + \frac{y}{4}H_{22}\,. \tag{A.2}$$

Up to NLO they read explicitly

$$\begin{aligned} H_{u1}(y) &= 1+\frac{C_F\alpha_s(\mu_h)}{4\pi}\bigg(-4\ln^2\frac{ym_b}{\mu_h}+10\ln\frac{ym_b}{\mu_h}-4\ln y \\ &\qquad -\frac{2\ln y}{1-y}-4\mathrm{L}_2(1-y)-\frac{\pi^2}{6}-12\bigg)\,, \\ H_{u3}(y) &= \frac{C_F\alpha_s(\mu_h)}{4\pi}\,\frac{2\ln y}{1-y}\,. \end{aligned} \tag{A.3}$$

The jet functions are less lengthy. We give their Laplace transform up to NNLO [70]

$$\begin{aligned} \widetilde{j}(L,\mu) &= 1+\frac{C_F\alpha_s}{4\pi}\left(2L^2-3L+7-\frac{2\pi^2}{3}\right) \\ &\quad +C_F\left(\frac{\alpha_s}{4\pi}\right)^2\left(C_FJ_F+C_AJ_A+T_Fn_fJ_f\right)\,, \end{aligned} \tag{A.4}$$

where

$$\begin{aligned} J_F &= 2L^4-6L^3+\left(\frac{37}{2}-\frac{4\pi^2}{3}\right)L^2+\left(-\frac{45}{2}+4\pi^2-24\zeta_3\right)L \\ &\quad +\frac{205}{8}-\frac{97\pi^2}{12}+\frac{61\pi^4}{90}-6\zeta_3\,, \\ J_A &= -\frac{22}{9}\,L^3+\left(\frac{367}{18}-\frac{2\pi^2}{3}\right)L^2+\left(-\frac{3155}{54}+\frac{11\pi^2}{9}+40\zeta_3\right)L \\ &\quad +\frac{53129}{648}-\frac{155\pi^2}{36}-\frac{37\pi^4}{180}-18\zeta_3\,, \\ J_f &= \frac{8}{9}\,L^3-\frac{58}{9}\,L^2+\left(\frac{494}{27}-\frac{4\pi^2}{9}\right)L-\frac{4057}{162}+\frac{13\pi^2}{9}\,. \end{aligned} \tag{A.5}$$

Finally the soft function receives a perturbative correction, that generates its radiative tail. Up to NNLO its Laplace transform is given by [72]

$$\begin{aligned} \widetilde{s}(L,\mu) &= 1+\frac{C_F\alpha_s(\mu_h)}{4\pi}\left(-4L^2+-4L-\frac{5\pi^2}{6}\right) \\ &\quad +C_F\left(\frac{\alpha_s}{4\pi}\right)^2\left(C_FS_F+C_AS_A+T_Fn_fS_f\right)\,, \end{aligned} \tag{A.6}$$

where

$$
\begin{aligned}
S_F &= 8L^4 + 16L^3 + \frac{10\pi^2 L^2}{3} + 8L^2 + \frac{10\pi^2 L}{3} + \frac{25\pi^4}{72}\,, \\
S_A &= \frac{88}{9}L^3 + \left(\frac{4\pi^2}{3} - \frac{136}{9}\right)L^2 + \left(\frac{56\pi^2}{9} + \frac{220}{27} - 36\zeta_3\right)L \\
&\quad - \frac{283\zeta_3}{9} + \frac{107\pi^4}{180} - \frac{233\pi^2}{36} - \frac{326}{81}\,, \\
S_f &= -\frac{32}{9}L^3 + \frac{32}{9}L^2 - \frac{20\pi^2}{9}L + \frac{7\pi^2}{9} - \frac{8}{81} + \frac{44}{9}\zeta_3\,.
\end{aligned}
\tag{A.7}
$$

A.2 RG factors and anomalous dimensions

In this appendix we list all perturbative quantities, related to the RG running up to the highest known order. We define the respective expansion coefficients as in eq.(2.16). In terms of these coefficients the Sudakov and anomalous dimension exponent from eq.(3.52) read [77]

$$\begin{aligned} a_\Gamma(\nu,\mu) &= \frac{\Gamma_0}{2\beta_0}\left\{\ln\frac{\alpha_s(\mu)}{\alpha_s(\nu)} + \left(\frac{\Gamma_1}{\Gamma_0}-\frac{\beta_1}{\beta_0}\right)\frac{\alpha_s(\mu)-\alpha_s(\nu)}{4\pi}\right. \\ &\quad \left. + \left[\frac{\Gamma_2}{\Gamma_0}-\frac{\beta_2}{\beta_0}-\frac{\beta_1}{\beta_0}\left(\frac{\Gamma_1}{\Gamma_0}-\frac{\beta_1}{\beta_0}\right)\right]\frac{\alpha_s^2(\mu)-\alpha_s^2(\nu)}{32\pi^2}+\dots\right\}, \end{aligned} \tag{A.8}$$

as well as

$$\begin{aligned} \mathcal{S}(\nu,\mu) &= \frac{\Gamma_0}{4\beta_0^2}\left\{\frac{4\pi}{\alpha_s(\nu)}\left(1-\frac{1}{r}-\ln r\right)+\left(\frac{\Gamma_1}{\Gamma_0}-\frac{\beta_1}{\beta_0}\right)(1-r+\ln r)+\frac{\beta_1}{2\beta_0}\ln^2 r\right. \\ &\quad + \frac{\alpha_s(\nu)}{4\pi}\left[\left(\frac{\beta_1\Gamma_1}{\beta_0\Gamma_0}-\frac{\beta_2}{\beta_0}\right)(1-r+r\ln r)+\left(\frac{\beta_1^2}{\beta_0^2}-\frac{\beta_2}{\beta_0}\right)(1-r)\ln r\right. \\ &\quad\quad \left.-\left(\frac{\beta_1^2}{\beta_0^2}-\frac{\beta_2}{\beta_0}-\frac{\beta_1\Gamma_1}{\beta_0\Gamma_0}+\frac{\Gamma_2}{\Gamma_0}\right)\frac{(1-r)^2}{2}\right] \\ &\quad + \left(\frac{\alpha_s(\nu)}{4\pi}\right)^2\left[\left(\frac{\beta_1\beta_2}{\beta_0^2}-\frac{\beta_1^3}{2\beta_0^3}-\frac{\beta_3}{2\beta_0}+\frac{\beta_1}{\beta_0}\left(\frac{\Gamma_2}{\Gamma_0}-\frac{\beta_2}{\beta_0}+\frac{\beta_1^2}{\beta_0^2}-\frac{\beta_1\Gamma_1}{\beta_0\Gamma_0}\right)\frac{r^2}{2}\right)\ln r\right. \\ &\quad\quad + \left(\frac{\Gamma_3}{\Gamma_0}-\frac{\beta_3}{\beta_0}+\frac{2\beta_1\beta_2}{\beta_0^2}+\frac{\beta_1^2}{\beta_0^2}\left(\frac{\Gamma_1}{\Gamma_0}-\frac{\beta_1}{\beta_0}\right)-\frac{\beta_2\Gamma_1}{\beta_0\Gamma_0}-\frac{\beta_1\Gamma_2}{\beta_0\Gamma_0}\right)\frac{(1-r)^3}{3} \\ &\quad\quad + \left(\frac{3\beta_3}{4\beta_0}-\frac{\Gamma_3}{2\Gamma_0}+\frac{\beta_1^3}{\beta_0^3}-\frac{3\beta_1^2\Gamma_1}{4\beta_0^2\Gamma_0}+\frac{\beta_2\Gamma_1}{\beta_0\Gamma_0}+\frac{\beta_1\Gamma_2}{4\beta_0\Gamma_0}-\frac{7\beta_1\beta_2}{4\beta_0^2}\right)(1-r)^2 \\ &\quad\quad \left.\left.+\left(\frac{\beta_1\beta_2}{\beta_0^2}-\frac{\beta_3}{\beta_0}-\frac{\beta_1^2\Gamma_1}{\beta_0^2\Gamma_0}+\frac{\beta_1\Gamma_2}{\beta_0\Gamma_0}\right)\frac{1-r}{2}\right]+\dots\right\}, \end{aligned} \tag{A.9}$$

where $r = \alpha_s(\mu)/\alpha_s(\nu)$. Note that knowledge about the three–loop results for the anomalous dimensions is necessary in order to consistently apply the results up to NNLO, which is now possible without any approximations. In addition the β–function and cusp–anomalous dimension are needed up to four–loops.

We list all the expressions for the β–function and anomalous dimensions in the $\overline{\text{MS}}$ scheme. The QCD β–function is currently known to five loops [161], however we list

only the first four orders, as required by the above equations

$$
\begin{aligned}
\beta_0 &= \frac{11}{3}C_A - \frac{4}{3}T_F n_f\,,\\
\beta_1 &= \frac{34}{3}C_A^2 - 4C_F T_F n_f - \frac{20}{3}C_A T_F n_f\,,\\
\beta_2 &= \frac{2857}{54}C_A^3 + 2C_F^2 T_F n_f - \frac{205}{9}C_F C_A T_F n_f\\
&\quad -\frac{1415}{27}C_A^2 T_F n_f + \frac{44}{9}C_F T_F^2 n_f^2 + \frac{158}{27}C_A T_F^2 n_f^2\,,\\
\beta_3 &= C_A^4\left(\frac{150653}{486} - \frac{44}{9}\zeta_3\right) + C_A^3 T_F n_f\left(-\frac{39143}{81} + \frac{136}{3}\zeta_3\right)\\
&\quad + C_A^2 C_F T_F n_f\left(\frac{7073}{243} - \frac{656}{9}\zeta_3\right) + C_A C_F^2 T_F n_f\left(-\frac{4204}{27} + \frac{352}{9}\zeta_3\right)\\
&\quad + 46 C_F^3 T_F n_f + C_A^2 T_F^2 n_f^2\left(\frac{7930}{81} + \frac{224}{9}\zeta_3\right) + C_F^2 T_F^2 n_f^2\left(\frac{1352}{27} - \frac{704}{9}\zeta_3\right)\\
&\quad + C_A C_F T_F^2 n_f^2\left(\frac{17152}{243} + \frac{448}{9}\zeta_3\right) + \frac{424}{243}C_A T_F^3 n_f^3 + \frac{1232}{243}C_F T_F^3 n_f^3\\
&\quad + \frac{d_A^{abcd} d_A^{abcd}}{N_A}\left(-\frac{80}{9} + \frac{704}{3}\zeta_3\right) + n_f\frac{d_F^{abcd} d_A^{abcd}}{N_A}\left(\frac{512}{9} - \frac{1664}{3}\zeta_3\right)\\
&\quad + n_f^2\frac{d_F^{abcd} d_F^{abcd}}{N_A}\left(-\frac{704}{9} + \frac{512}{3}\zeta_3\right)\,.
\end{aligned}
\tag{A.10}
$$

The cusp–anomalous dimension is currently known to four–loop accuracy [79] and reads

$$
\begin{aligned}
\Gamma_0 &= 4C_F\,,\\
\Gamma_1 &= 4C_F\left[\left(\frac{67}{9} - \frac{\pi^2}{3}\right)C_A - \frac{20}{9}T_F n_f\right]\,,\\
\Gamma_2 &= 4C_F\left[C_A^2\left(\frac{245}{6} - \frac{134\pi^2}{27} + \frac{11\pi^4}{45} + \frac{22}{3}\zeta_3\right) + C_A T_F n_f\left(-\frac{418}{27} + \frac{40\pi^2}{27} - \frac{56}{3}\zeta_3\right)\right.\\
&\quad \left. + C_F T_F n_f\left(-\frac{55}{3} + 16\zeta_3\right) - \frac{16}{27}T_F^2 n_f^2\right]\,,
\end{aligned}
\tag{A.11}
$$

$$
\begin{aligned}
\Gamma_3 &= C_F\Bigg[C_A^3\left(\frac{1309\zeta_3}{432}-\frac{11\pi^2\zeta_3}{144}-\frac{\zeta_3^2}{16}-\frac{451\zeta_5}{288}+\frac{42139}{10368}-\frac{5525\pi^2}{7776}+\frac{451\pi^4}{5760}-\frac{313\pi^6}{90720}\right)\\
&\quad+n_fT_FC_A^2\left(-\frac{361\zeta_3}{54}+\frac{7\pi^2\zeta_3}{36}+\frac{131\zeta_5}{72}-\frac{24137}{10368}+\frac{635\pi^2}{1944}-\frac{11\pi^4}{2160}\right)\\
&\quad+n_fT_FC_FC_A\left(\frac{29\zeta_3}{9}-\frac{\pi^2\zeta_3}{6}+\frac{5\zeta_5}{4}-\frac{17033}{5184}+\frac{55\pi^2}{288}-\frac{11\pi^4}{720}\right)\\
&\quad+n_fT_FC_F^2\left(\frac{37\zeta_3}{24}-\frac{5\zeta_5}{2}+\frac{143}{288}\right)+(n_fT_F)^2C_A\left(\frac{35\zeta_3}{27}-\frac{7\pi^4}{1080}-\frac{19\pi^2}{972}+\frac{923}{5184}\right)\\
&\quad+(n_fT_F)^2C_F\left(-\frac{10\zeta_3}{9}+\frac{\pi^4}{180}+\frac{299}{648}\right)+(n_fT_F)^3\left(-\frac{1}{81}+\frac{2\zeta_3}{27}\right)\Bigg]\\
&\quad+\frac{d_F^{abcd}d_A^{abcd}}{N_F}\left(\frac{\zeta_3}{6}-\frac{3\zeta_3^2}{2}+\frac{55\zeta_5}{12}-\frac{\pi^2}{12}-\frac{31\pi^6}{7560}\right)+n_f\frac{d_F^{abcd}d_F^{abcd}}{N_F}\left(\frac{\pi^2}{6}-\frac{\zeta_3}{3}-\frac{5\zeta_5}{3}\right).
\end{aligned}
$$

The anomalous dimensions γ_J and γ' are both known to three–loop order. The jet anomalous dimension coefficients are given by [77]

$$
\begin{aligned}
\gamma_0^J &= -3C_F\,,\\
\gamma_1^J &= C_F^2\left(-\frac{3}{2}+2\pi^2-24\zeta_3\right)+C_FC_A\left(-\frac{1769}{54}-\frac{11\pi^2}{9}+40\zeta_3\right)+C_FT_Fn_f\left(\frac{242}{27}+\frac{4\pi^2}{9}\right),\\
\gamma_2^J &= C_F^3\left(-\frac{29}{2}-3\pi^2-\frac{8\pi^4}{5}-68\zeta_3+\frac{16\pi^2}{3}\,\zeta_3+240\zeta_5\right)\\
&\quad+C_F^2C_A\left(-\frac{151}{4}+\frac{205\pi^2}{9}+\frac{247\pi^4}{135}-\frac{844}{3}\,\zeta_3-\frac{8\pi^2}{3}\,\zeta_3-120\zeta_5\right)\\
&\quad+C_FC_A^2\left(-\frac{412907}{2916}-\frac{419\pi^2}{243}-\frac{19\pi^4}{10}+\frac{5500}{9}\,\zeta_3-\frac{88\pi^2}{9}\,\zeta_3-232\zeta_5\right)\\
&\quad+C_F^2T_Fn_f\left(\frac{4664}{27}-\frac{32\pi^2}{9}-\frac{164\pi^4}{135}+\frac{208}{9}\,\zeta_3\right)\\
&\quad+C_FC_AT_Fn_f\left(-\frac{5476}{729}+\frac{1180\pi^2}{243}+\frac{46\pi^4}{45}-\frac{2656}{27}\,\zeta_3\right)\\
&\quad+C_FT_F^2n_f^2\left(\frac{13828}{729}-\frac{80\pi^2}{81}-\frac{256}{27}\,\zeta_3\right)
\end{aligned}
\tag{A.12}
$$

and the ones for γ' are [81]

$$
\begin{aligned}
\gamma'_0 &= -5C_F\,, \\
\gamma'_1 &= -8C_F\left[\left(\frac{3}{16}-\frac{\pi^2}{4}+3\zeta_3\right)C_F+\left(\frac{1549}{432}+\frac{7\pi^2}{48}-\frac{11}{4}\,\zeta_3\right)C_A-\left(\frac{125}{216}+\frac{\pi^2}{24}\right)n_f\right], \\
\gamma'_2 &= C_F\Bigg[C_A^2\left(\frac{2786}{9}\zeta_3-\frac{56\pi^2}{9}\zeta_3-100\zeta_5-\frac{250477}{2916}+\frac{1691\pi^2}{486}-\frac{127\pi^4}{90}\right) \\
&\quad +C_AC_F\left(-\frac{844}{3}\zeta_3-\frac{8\pi^2}{3}\zeta_3-120\zeta_5-\frac{151}{4}+\frac{205\pi^2}{9}+\frac{247\pi^4}{135}\right) \\
&\quad +C_F^2\left(-68\zeta_3+\frac{16\pi^2}{3}\zeta_3+240\zeta_5-\frac{29}{2}-3\pi^2-\frac{8\pi^4}{5}\right) \\
&\quad +C_An_fT_F\left(-\frac{440}{27}\zeta_3-\frac{7706}{729}+\frac{1874\pi^2}{243}+\frac{22\pi^4}{45}\right) \\
&\quad +C_Fn_fT_F\left(\frac{224}{9}\zeta_3+\frac{3943}{27}-\frac{26\pi^2}{9}-\frac{28\pi^4}{27}\right) \\
&\quad +(n_fT_F)^2\left(-\frac{32}{27}\zeta_3+\frac{10532}{729}-\frac{40\pi^2}{27}\right)\Bigg].
\end{aligned}
\tag{A.13}
$$

A.3 Conversions to the kinetic scheme

We give the explicit formulas for the conversion from the OS to the kinetic scheme for the mass and the HQE parameters up to order α_s^2 [86, 154]. The expressions to order α_s^3 are also available, however extremely lengthy and hence we refer to [86] for their explicit form. The conversions read

$$\begin{aligned}
\frac{m^{\mathrm{OS}}}{m^{\mathrm{kin}}} =& 1 + \frac{\alpha_s^{(n_f)}(\mu)}{\pi} C_F \left(\frac{4}{3} \frac{\mu}{m^{\mathrm{kin}}} + \frac{1}{2} \frac{\mu^2}{(m^{\mathrm{kin}})^2} \right) \\
& - \left(\frac{\alpha_s^{(n_f)}(\mu)}{\pi} \right)^2 C_F \left\{ \frac{\mu}{m^{\mathrm{kin}}} \left[C_A \left(-\frac{215}{27} + \frac{2\pi^2}{9} + \frac{22}{9} l_\mu \right) + n_f T_F \left(\frac{64}{27} - \frac{8}{9} l_\mu \right) \right] \right. \\
& \left. + \frac{\mu^2}{(m^{\mathrm{kin}})^2} \left[C_A \left(-\frac{91}{36} + \frac{\pi^2}{12} + \frac{11}{12} l_\mu \right) + n_f T_F \left(\frac{13}{18} - \frac{1}{3} l_\mu \right) \right] \right\}, \\
\left[\bar{\Lambda}(\mu) \right]_{\mathrm{pert}} =& \frac{\alpha_s^{(n_f)}(\mu)}{\pi} C_F \, \mu \left(\frac{4}{3} + \frac{\alpha_s^{(n_f)}(\mu)}{\pi} \left(\frac{1}{27} C_A \big(215 - 6\pi^2 - 66 l_\mu \big) - \frac{8}{27} n_f T_F \big(8 - 3 l_\mu \big) \right) \right), \\
\left[\mu_\pi^2(\mu) \right]_{\mathrm{pert}} =& \frac{\alpha_s^{(n_f)}(\mu)}{\pi} C_F \, \mu^2 \left(1 + \frac{\alpha_s^{(n_f)}(\mu)}{\pi} \left(\frac{1}{18} C_A \big(91 - 3\pi^2 - 33 l_\mu \big) - \frac{1}{9} n_f T_F \big(13 - 6 l_\mu \big) \right) \right),
\end{aligned}$$

where the shorthand notation $l_\mu = \ln(\mu^2/m_b^2)$ was used.

A.4 Differential P_+ spectrum with kinematical cuts

The differential P_+ spectrum is obtained by integrating the triple differential rate eq.(3.39) over P_ℓ and P_-

$$\frac{\mathrm{d}\Gamma_u(y_{\max}, y_0)}{\mathrm{d}P_+} = \begin{cases} \Gamma_u^A(y_{\max}) & , \quad y_{\max} \le y_0 \\ \Gamma_u^A(y_0) + \Gamma_u^B & , \quad y_{\max} > y_0 \end{cases} , \tag{A.14}$$

where

$$\begin{aligned} \Gamma_u^A(y_i) &= \frac{G_F^2 |V_{ub}|^2}{96\pi^3} (m_B - P_+)^5 \int_0^{y_i} \mathrm{d}y\, y^2 \left[(3-2y)\, f_1 + 6(1-y)\, f_2 + y\, f_3\right], \\ \Gamma_u^B &= \frac{G_F^2 |V_{ub}|^2}{96\pi^3} (m_B - P_+)^5 \int_{y_0}^{y_{\max}} \mathrm{d}y\, y_0 \\ &\quad \times \left[\big(6y(1+y_0) - 6y^2 - y_0(3+2y_0)\big)\, f_1 + 6y(1-y)\, f_2 + y_0(3y - 2y_0)\, f_3\right] \end{aligned} \tag{A.15}$$

and y_0 and $y_{\max}$ are the limits of the y integration. Whenever there is a cut on the lepton energy $E_\ell \ge E_{\mathrm{cut}}$, the lower limit of the y integration reads

$$y_0 = \frac{P_l^{\max} - P_+}{m_B - P_+} = 1 - \frac{2E_{\mathrm{cut}}}{m_B - P_+}\,, \tag{A.16}$$

while the lower limit on the final P_+ integration is always $P_+^{\min} = 0$.

Apart from the lepton energy cut, there are often cuts on the hadronic and leptonic invariant masses m_X and q^2. If we constrain the former by $m_X \le m_{\mathrm{cut}}$, the upper limits of the y and P_+ integration read respectively

$$y_{\max} = \frac{\min(m_B, m_{\mathrm{cut}}^2/P_+) - P_+}{m_B - P_+}, \qquad P_+^{\max} = \min(m_{\mathrm{cut}}, m_B - 2E_{\mathrm{cut}})\,. \tag{A.17}$$

When constraining the lepton invariant mass with $q^2 \ge q_{\mathrm{cut}}^2$ the upper limits read

$$y_{\max} = 1 - \frac{q_{\mathrm{cut}}^2}{(m_B - P_+)^2}, \qquad P_+^{\max} = \min(m_B - q_{\mathrm{cut}}, m_B - 2E_{\mathrm{cut}})\,. \tag{A.18}$$

We can also apply cuts on all formerly mentioned variables, in which case the minimum of the limits above marks the upper y and P_+ integration.

A.5 Additional material to the V_{cb} fit

In this appendix we give several additional fit results for the determinations in chapter 5. In figure A.10 we show the different 1D χ^2 profile scans for several fit parameters and the correlation parameters ρ_{mom} and ρ_{cut}. As mentioned in the main chapter, we observe a non–parabolic behaviour for the correlation parameters and thus their uncertainty is determined with an ensemble of pseudo–experiments. The other χ^2 profiles show a parabolic form, so the assumption of Gaussian constraints is well justified.

In figures A.6, A.7, A.8 and A.9 we show the results of our fits for fixed pairs of the correlation parameters. We depict the Belle and Belle II data separately and for the combined data set. It can nicely be seen, that the results for V_{cb} and the HQE parameters do not strongly depend on the choice of the correlation parameters.

In table A.3 we show the result of our default fit, with all $1/m_b^4$ parameters set to zero.

	$\lvert V_{\text{cb}}\rvert \times 10^3$	m_b^{kin}	$\overline{m}_c$	μ_G^2	μ_π^2	ρ_D^3	ρ_{cut}	ρ_{mom}
Value	41.76	4.56	1.10	0.38	0.43	0.03	0.05	0.14
Uncertainty	0.57	0.02	0.01	0.07	0.24	0.02	-	-

Table A.3: Results of our default fit using both Belle and Belle II data for $|V_{cb}|$, m_b^{kin}, $\overline{m}_c$, ρ_D^3, and the correlation parameters ρ_{cut} and ρ_{mom}. The $\mathcal{O}(1/m_b^4)$ terms are set to zero. All parameters are expressed in GeV at the appropriate power.

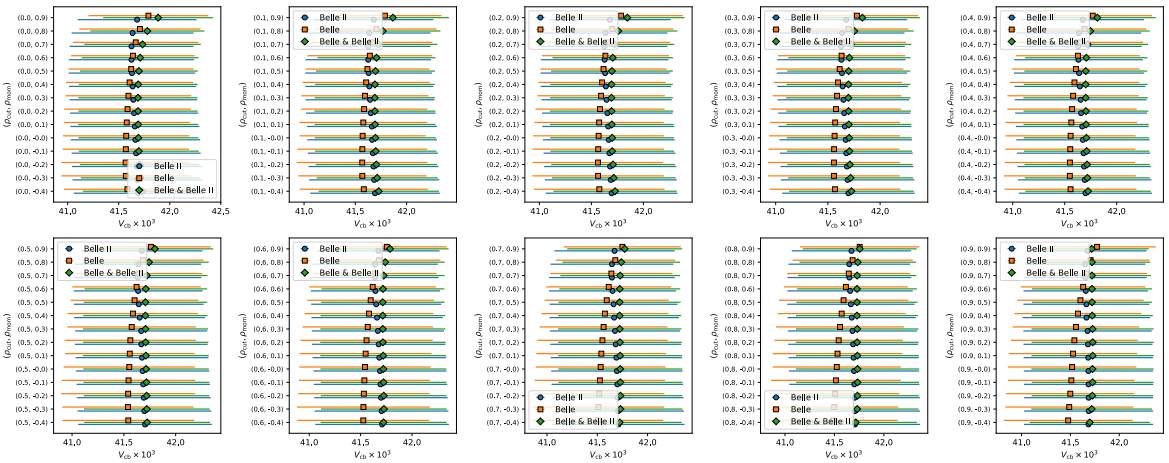

Figure A.6: Fit results for $|V_{cb}|$ for different combinations of correlation parameter values.

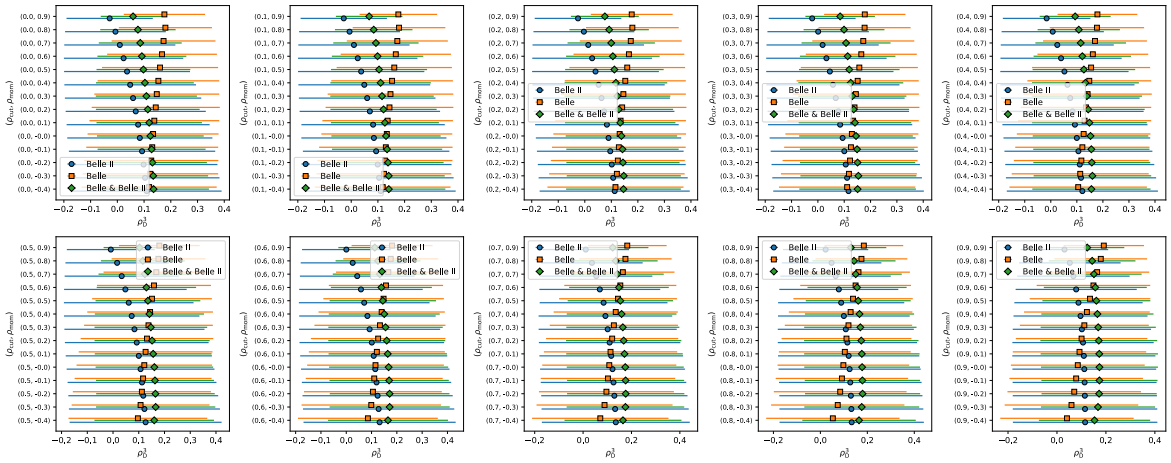

Figure A.7: Fit results forρ_D^3 for different combinations of correlation parameter values.

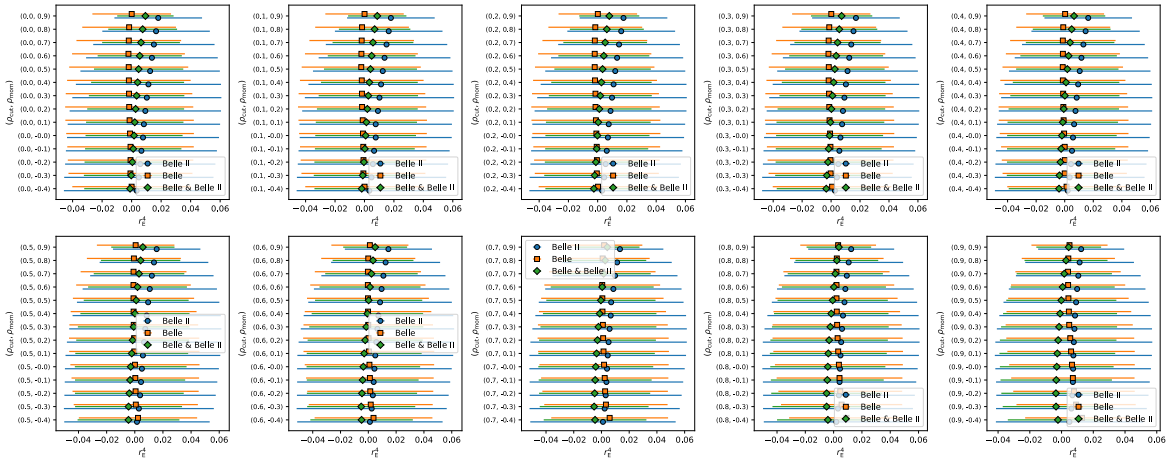

Figure A.8: Fit results for r_E^4 for different combinations of correlation parameter values.

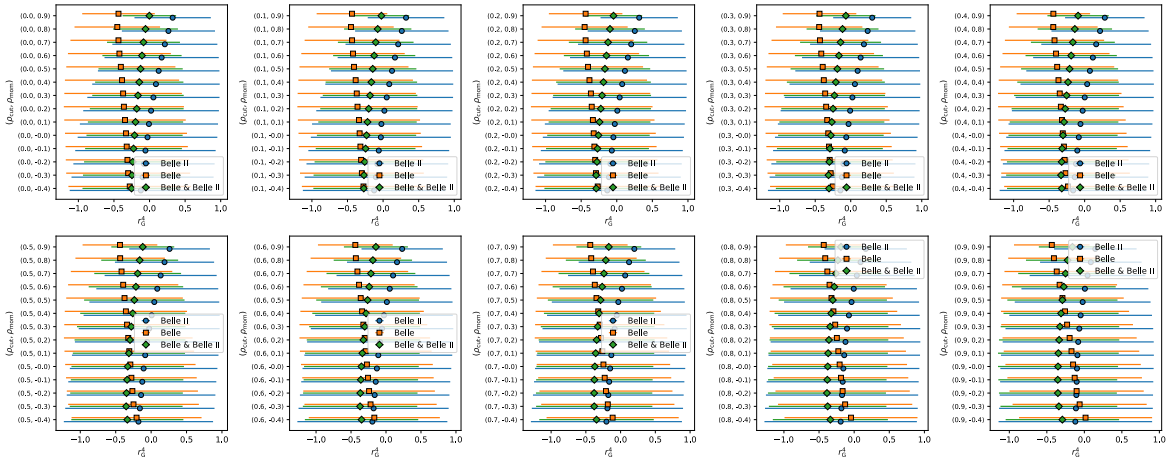

Figure A.9: Fit results for r_G^4 for different combinations of correlation parameter values.

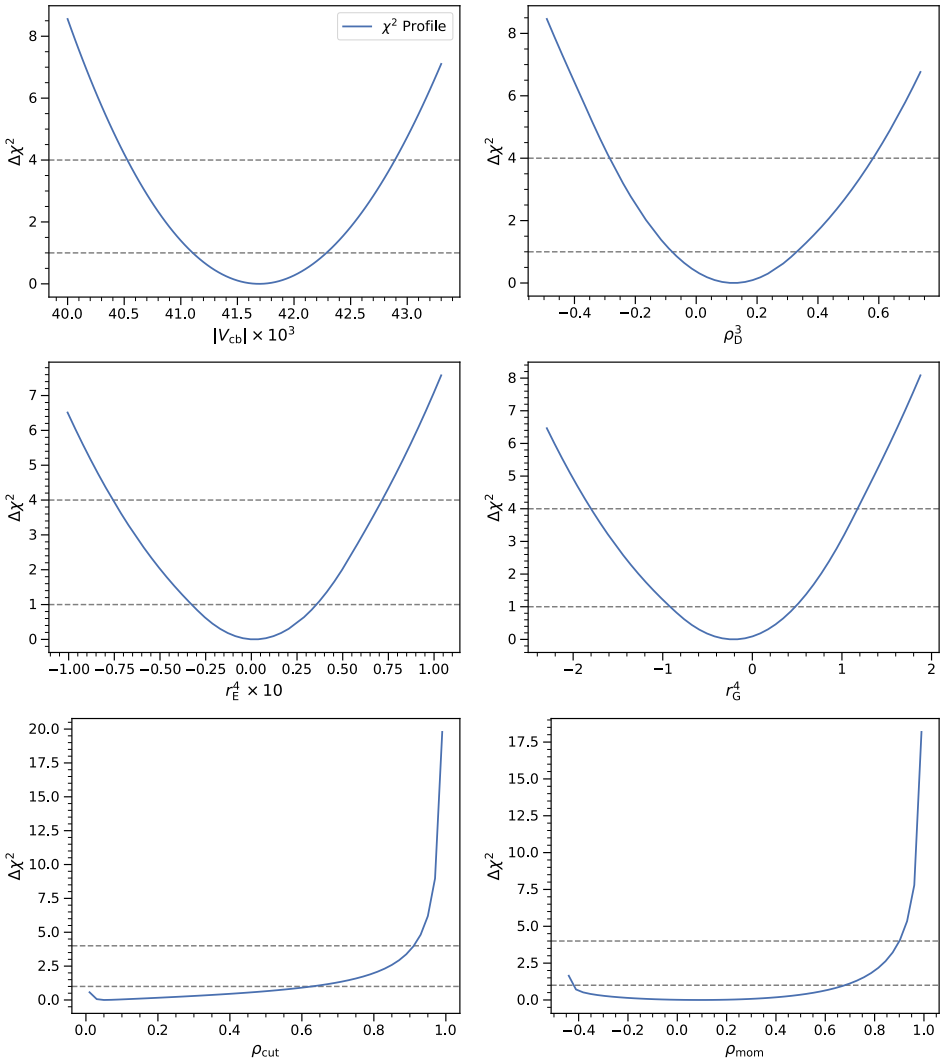

Figure A.10: 1D χ^2 profile scans for $|V_{cb}| \times 10^3$, ρ_D^3, $r_E^4 \times 10$, and r_G^4. The minimum χ^2_{min} is subtracted from the χ^2 function.

Bibliography

[1] S. L. Glashow. *Partial Symmetries of Weak Interactions*. Nucl. Phys. 22 (1961).

[2] A. Salam. *Weak and Electromagnetic Interactions*. Conf. Proc. C 680519 (1968).

[3] S. Weinberg. *A Model of Leptons*. Phys. Rev. Lett. 19 (1967).

[4] V. C. Rubin and W. K. Ford Jr. *Rotation of the Andromeda Nebula from a Spectroscopic Survey of Emission Regions*. Astrophys. J. 159 (1970).

[5] V. C. Rubin, N. Thonnard, and W. K. Ford Jr. *Rotational properties of 21 SC galaxies with a large range of luminosities and radii, from NGC 4605 /R = 4kpc/ to UGC 2885 /R = 122 kpc/*. Astrophys. J. 238 (1980).

[6] L. Canetti, M. Drewes, and M. Shaposhnikov. *Matter and Antimatter in the Universe*. New J. Phys. 14 (2012). arXiv: `1204.4186 [hep-ph]`.

[7] A. D. Sakharov. *Violation of CP Invariance, C asymmetry, and baryon asymmetry of the universe*. Pisma Zh. Eksp. Teor. Fiz. 5 (1967).

[8] D. J. Gross and F. Wilczek. *Ultraviolet Behavior of Nonabelian Gauge Theories*. Phys. Rev. Lett. 30 (1973).

[9] N. Cabibbo. *Unitary Symmetry and Leptonic Decays*. Phys. Rev. Lett. 10 (1963).

[10] M. Kobayashi and T. Maskawa. *CP Violation in the Renormalizable Theory of Weak Interaction*. Prog. Theor. Phys. 49 (1973).

[11] K. Olschewsky. *InclusiveVcb*. Version 0.1.0. Source: `https://github.com/kolschew/InclusiveVcb`.

[12] K. Olschewsky. *InclusiveRatesVub*. Version 0.1.0. Source: `https://github.com/kolschew/InclusiveRatesVub`.

[13] T. Mannel, K. Olschewsky, and K. K. Vos. *CP violation in three-body B decays: a model ansatz*. Journal of High Energy Physics 2020.6 (2020). arXiv: 2003.12053 [hep-ph].

[14] R. Aaij et. al. [LHCb Collaboration]. *Amplitude analysis of the $B^+ \to \pi^+\pi^+\pi^-$ decay*. Phys. Rev. D 101.1 (2020). arXiv: 1909.05212 [hep-ex].

[15] R. Aaij et. al. [LHCb Collaboration]. *Observation of Several Sources of CP Violation in $B^+ \to \pi^+\pi^+\pi^-$ Decays*. Phys. Rev. Lett. 124.3 (2020). arXiv: 1909.05211 [hep-ex].

[16] R. Aaij et. al. [LHCb Collaboration]. *Measurements of CP violation in the three-body phase space of charmless $B^\pm$ decays*. Phys. Rev. D 90.11 (2014). arXiv: 1408.5373 [hep-ex].

[17] R. van Tonder et. al. [Belle Collaboration]. *Measurements of q^2 Moments of Inclusive $B \to X_c\ell^+\nu_\ell$ Decays with Hadronic Tagging*. Phys. Rev. D 104.11 (2021). arXiv: 2109.01685 [hep-ex].

[18] [Belle II collaboration]. *Measurement of Lepton Mass Squared Moments in $B \to X_c\ell\bar{\nu}_\ell$ Decays with the Belle II Experiment* (2022). arXiv: 2205.06372 [hep-ex].

[19] F. Bernlochner et al. *First extraction of inclusive V_{cb} from q^2 moments* (2022). arXiv: 2205.10274 [hep-ph].

[20] S. W. Bosch et al. *Factorization and shape function effects in inclusive B meson decays*. Nucl. Phys. B 699 (2004). arXiv: hep-ph/0402094.

[21] B. O. Lange, M. Neubert, and G. Paz. *Theory of charmless inclusive B decays and the extraction of V_{ub}*. Phys. Rev. D 72 (2005). arXiv: hep-ph/0504071.

[22] T. Cheng et al. *Gauge Theory of Elementary Particle Physics*. Clarendon Press, (1984).

[23] M. Robinson. *Symmetry and the Standard Model: Mathematics and Particle Physics*. Springer New York, (2014).

[24] M. Schwartz. *Quantum Field Theory and the Standard Model*. Cambridge University Press, (2014).

[25] T. Asaka, S. Blanchet, and M. Shaposhnikov. *The νMSM, dark matter and neutrino masses*. Phys. Lett. B 631 (2005). arXiv: hep-ph/0503065.

[26] P. A. Zyla et. al. [Particle Data Group]. *Review of Particle Physics*. PTEP 2020.8 (2020).

[27] L. Wolfenstein. *Parametrization of the Kobayashi-Maskawa Matrix*. Phys. Rev. Lett. 51 (1983).

[28] J. Charles et al. *Current status of the standard model CKM fit and constraints on $\Delta F = 2$ new physics*. Physical Review D 91.7 (2015). arXiv: `hep-ph/1501.05013`.

[29] U. Van Kolck, L. J. Abu-Raddad, and D. M. Cardamone. *Introduction to effective field theories in QCD*. AIP Conf. Proc. 631.1 (2002). arXiv: `nucl-th/0205058`.

[30] S. Weinberg. *The Quantum Theory of Fields, Volume 2: Modern Applications*. Cambridge University Press, (1995).

[31] G. Buchalla, A. J. Buras, and M. E. Lautenbacher. *Weak decays beyond leading logarithms*. Rev. Mod. Phys. 68 (1996). arXiv: `hep-ph/9512380`.

[32] A. J. Buras. *Weak Hamiltonian, CP violation and rare decays*. Les Houches Lect.Notes 68, (1998). arXiv: `hep-ph/9806471`.

[33] T. Mannel, W. Roberts, and Z. Ryzak. *A Derivation of the heavy quark effective Lagrangian from QCD*. Nucl. Phys. B 368 (1992).

[34] T. Mannel. *Effective Field Theories in Flavour Physics*. Springer Berlin Heidelberg, (2004).

[35] T. Mannel. *Effective Field Theories for Heavy Quarks: Heavy Quark Effective Theory and Heavy Quark Expansion*. Les Houches Lect.Notes 108, (2020).

[36] L. Edelhäuser and A. K. Knochel. *Tutorium Quantenfeldtheorie*. Springer Spektrum, (2016).

[37] B. M. Dassinger, T. Mannel, and S. Turczyk. *Inclusive semi-leptonic B decays to order $1/m_b^4$*. JHEP 03 (2007). arXiv: `hep-ph/0611168`.

[38] T. Mannel, S. Turczyk, and N. Uraltsev. *Higher Order Power Corrections in Inclusive B Decays*. JHEP 11 (2010). arXiv: `1009.4622 [hep-ph]`.

[39] M. E. Luke. *Effects of subleading operators in the heavy quark effective theory*. Physics Letters B 252.3 (1990).

[40] P. Gambino, K. J. Healey, and S. Turczyk. *Taming the higher power corrections in semileptonic B decays*. Phys. Lett. B 763 (2016). arXiv: `1606.06174 [hep-ph]`.

[41] M. Fael, T. Mannel, and K. Keri Vos. *V_{cb} determination from inclusive $b \to c$ decays: an alternative method*. JHEP 02 (2019). arXiv: 1812.07472 [hep-ph].

[42] A. V. Manohar and M. B. Wise. *Heavy Quark Physics*. Cambridge University Press, (2000).

[43] M. J. Dugan, M. Golden, and B. Grinstein. *On the Hilbert space of the heavy quark effective theory*. Physics Letters B 282.1 (1992).

[44] Y.-Q. Chen. *On the reparameterization invariance in heavy quark effective theory*. Physics Letters B 317.3 (1993).

[45] J. Heinonen, R. J. Hill, and M. P. Solon. *Lorentz invariance in heavy particle effective theories*. Phys. Rev. D 86 (2012). arXiv: 1208.0601 [hep-ph].

[46] A. V. Manohar. *Reparametrization Invariance Constraints on Inclusive Decay Spectra and Masses*. Phys. Rev. D 82 (2010). arXiv: 1005.1952 [hep-ph].

[47] M. E. Luke and A. V. Manohar. *Reparametrization invariance constraints on heavy particle effective field theories*. Phys. Lett. B 286 (1992). arXiv: hep-ph/9205228.

[48] T. Mannel and K. K. Vos. *Reparametrization Invariance and Partial Re-Summations of the Heavy Quark Expansion*. JHEP 06 (2018). arXiv: 1802.09409 [hep-ph].

[49] T. Mannel, A. V. Rusov, and F. Shahriaran. *Inclusive semitauonic B decays to order $\mathcal{O}(\Lambda_{QCD}^3/m_b^3)$*. Nucl. Phys. B 921 (2017). arXiv: 1702.01089 [hep-ph].

[50] M. Neubert. *Analysis of the photon spectrum in inclusive $B \to X_s\gamma$ decays*. Phys. Rev. D 49 (1994). arXiv: hep-ph/9312311.

[51] T. Mannel and M. Neubert. *Resummation of nonperturbative corrections to the lepton spectrum in inclusive $B \to X\ell\bar{\nu}$ decays*. Phys. Rev. D 50 (1994). arXiv: hep-ph/9402288.

[52] I. I. Y. Bigi et al. *On the motion of heavy quarks inside hadrons: Universal distributions and inclusive decays*. Int. J. Mod. Phys. A 9 (1994). arXiv: hep-ph/9312359.

[53] C. W. Bauer, M. E. Luke, and T. Mannel. *Light cone distribution functions for B decays at subleading order in $1/m_b$*. Phys. Rev. D 68 (2003). arXiv: hep-ph/0102089.

[54] C. W. Bauer, M. Luke, and T. Mannel. *Subleading shape functions in $B \to X_u\ell\bar{\nu}$ and the determination of $|V_{ub}|$*. Phys. Lett. B 543 (2002). arXiv: hep-ph/0205150.

[55] A. K. Leibovich, Z. Ligeti, and M. B. Wise. *Enhanced Subleading Structure Functions in Semileptonic B Decay*. Phys. Lett. B 539 (2002). arXiv: hep-ph/0205148.

[56] S. W. Bosch, M. Neubert, and G. Paz. *Subleading shape functions in inclusive B decays*. JHEP 11 (2004). arXiv: hep-ph/0409115.

[57] T. Mannel and M. Neubert. *Resummation of nonperturbative corrections to the lepton spectrum in inclusive $B \to X$ lepton anti-neutrino decays*. Phys. Rev. D 50 (1994). arXiv: hep-ph/9402288.

[58] C. Greub, M. Neubert, and B. D. Pecjak. *NNLO corrections to $B \to X_u l\nu$ and the determination of $|V_{ub}|$*. Eur. Phys. J. C 65 (2010). arXiv: 0909.1609 [hep-ph].

[59] M. Neubert. *Effective field theory and heavy quark physics* (2005). arXiv: hep-ph/0512222.

[60] M. Neubert. *QCD based interpretation of the lepton spectrum in inclusive $\bar{B} \to X_u \ell\bar{\nu}$ decays*. Phys. Rev. D 49 (1994). arXiv: hep-ph/9311325.

[61] B. O. Lange. *Soft-Collinear Factorization and Sudakov Resummation of Heavy Meson Decay Amplitudes with Effective Field Theories*. 2004. arXiv: hep-ph/0409277 [hep-ph].

[62] C. W. Bauer et al. *An Effective field theory for collinear and soft gluons: Heavy to light decays*. Phys. Rev. D 63 (2001). arXiv: hep-ph/0011336.

[63] C. W. Bauer, D. Pirjol, and I. W. Stewart. *Soft collinear factorization in effective field theory*. Phys. Rev. D 65 (2002). arXiv: hep-ph/0109045.

[64] M. Beneke et al. *Soft collinear effective theory and heavy to light currents beyond leading power*. Nucl. Phys. B 643 (2002). arXiv: hep-ph/0206152.

[65] T. Becher, A. Broggio, and A. Ferroglia. *Introduction to Soft-Collinear Effective Theory*. Vol. 896. Springer, (2015). arXiv: 1410.1892 [hep-ph].

[66] T. Becher. *Soft-Collinear Effective Theory*. Les Houches Lect.Notes 108 (2020). arXiv: 1803.04310 [hep-ph].

[67] G. Bell et al. *Heavy-to-light currents at NNLO in SCET and semi-inclusive $\bar{B} \to X_s l^+ l^-$ decay*. Nucl. Phys. B 843 (2011). arXiv: 1007.3758 [hep-ph].

[68] M. Beneke, T. Huber, and X. Q. Li. *Two-loop QCD correction to differential semi-leptonic $b \to u$ decays in the shape-function region*. Nucl. Phys. B 811 (2009). arXiv: 0810.1230 [hep-ph].

[69] H. M. Asatrian, C. Greub, and B. D. Pecjak. *NNLO corrections to $B \to X_u \ell \nu$ in the shape-function region*. Phys. Rev. D 78 (2008). arXiv: 0810.0987 [hep-ph].

[70] T. Becher and M. Neubert. *Toward a NNLO calculation of the $B \to X_s \gamma$ decay rate with a cut on photon energy. II. Two-loop result for the jet function*. Phys. Lett. B 637 (2006). arXiv: hep-ph/0603140.

[71] M. Neubert. *Advanced predictions for moments of the $B \to X_s \gamma$ spectrum*. Physical Review D 72.7 (2005).

[72] T. Becher and M. Neubert. *Toward a NNLO calculation of the $B \to X_s \gamma$ decay rate with a cut on photon energy: I. Two-loop result for the soft function*. Phys. Lett. B 633 (2006). arXiv: hep-ph/0512208.

[73] G. P. Korchemsky and G. Marchesini. *Structure function for large x and renormalization of Wilson loop*. Nucl. Phys. B 406 (1993). arXiv: hep-ph/9210281.

[74] M. Neubert. *Renormalization-group improved calculation of the $B \to X_s \gamma$ branching ratio*. Eur. Phys. J. C 40 (2005). arXiv: hep-ph/0408179.

[75] C. W. Bauer and A. V. Manohar. *Shape function effects in $B \to X_s \gamma$ and $B \to X_u \ell \nu$ decays*. Phys. Rev. D 70 (2004). arXiv: hep-ph/0312109.

[76] B. O. Lange and M. Neubert. *Renormalization group evolution of the B meson light cone distribution amplitude*. Phys. Rev. Lett. 91 (2003). arXiv: hep-ph/0303082.

[77] T. Becher, M. Neubert, and B. D. Pecjak. *Factorization and Momentum-Space Resummation in Deep-Inelastic Scattering*. JHEP 01 (2007). arXiv: hep-ph/0607228.

[78] S. Moch, J. A. M. Vermaseren, and A. Vogt. *The Three loop splitting functions in QCD: The Nonsinglet case*. Nucl. Phys. B 688 (2004). arXiv: hep-ph/0403192.

[79] J. M. Henn, G. P. Korchemsky, and B. Mistlberger. *The full four-loop cusp anomalous dimension in $\mathcal{N} = 4$ super Yang-Mills and QCD*. JHEP 04 (2020). arXiv: 1911.10174 [hep-th].

[80] G. Bell. *NNLO corrections to inclusive semileptonic B decays in the shape-function region*. Nucl. Phys. B 812 (2009). arXiv: 0810.5695 [hep-ph].

[81] R. Brüser, Z. L. Liu, and M. Stahlhofen. *Three-loop soft function for heavy-to-light quark decays*. JHEP 03 (2020). arXiv: 1911.04494 [hep-ph].

[82] I. I. Y. Bigi et al. *The Pole mass of the heavy quark. Perturbation theory and beyond*. Phys. Rev. D 50 (1994). arXiv: hep-ph/9402360.

[83] M. Beneke and V. M. Braun. *Heavy quark effective theory beyond perturbation theory: Renormalons, the pole mass and the residual mass term*. Nucl. Phys. B 426 (1994). arXiv: hep-ph/9402364.

[84] M. Beneke. *Renormalons*. Phys. Rept. 317 (1999). arXiv: hep-ph/9807443.

[85] M. Beneke. *More on ambiguities in the pole mass*. Phys. Lett. B 344 (1995). arXiv: hep-ph/9408380.

[86] M. Fael, K. Schönwald, and M. Steinhauser. *Relation between the* $\overline{\text{MS}}$ *and the kinetic mass of heavy quarks*. Phys. Rev. D 103.1 (2021). arXiv: 2011.11655 [hep-ph].

[87] S. Biswas and K. Melnikov. *Second order QCD corrections to inclusive semileptonic* $b \to c\ell\bar{\nu}$ *decays with massless and massive lepton*. JHEP 02 (2010). arXiv: 0911.4142 [hep-ph].

[88] I. I. Y. Bigi et al. *Sum rules for heavy flavor transitions in the SV limit*. Phys. Rev. D 52 (1995). arXiv: hep-ph/9405410.

[89] I. I. Y. Bigi et al. *High power n of* m_b *in beauty widths and* $n = 5 \to \infty$ *limit*. Phys. Rev. D 56 (1997). arXiv: hep-ph/9704245.

[90] A. Czarnecki, K. Melnikov, and N. Uraltsev. *Non Abelian dipole radiation and the heavy quark expansion*. Phys. Rev. Lett. 80 (1998). arXiv: hep-ph/9708372.

[91] M. Beneke et al. *QCD factorization for exclusive non-leptonic -meson decays: general arguments and the case of heavy–light final states*. Nuclear Physics B 591.1–2 (2000).

[92] M. Beneke et al. *QCD Factorization for* $B \to \pi\pi$ *Decays: Strong Phases and CP Violation in the Heavy Quark Limit*. Phys. Rev. Lett. 83 (1999). arXiv: hep-ph/9905312.

[93] M. Beneke et al. *QCD factorization in* $B \to \pi K, \pi\pi$ *decays and extraction of Wolfenstein parameters*. Nucl. Phys. B 606 (2001). arXiv: hep-ph/0104110.

[94] M. Beneke and M. Neubert. *QCD factorization for* $B \to PP$ *and* $B \to PV$ *decays*. Nucl. Phys. B 675 (2003). arXiv: hep-ph/0308039.

[95] S. Kränkl, T. Mannel, and J. Virto. *Three-body non-leptonic B decays and QCD factorization*. Nucl. Phys. B 899 (2015). arXiv: 1505.04111 [hep-ph].

[96] R. Klein et al. *CP Violation in Multibody B Decays from QCD Factorization.* JHEP 10 (2017). arXiv: 1708.02047 [hep-ph].

[97] H.-Y. Cheng, C.-K. Chua, and A. Soni. *Charmless three-body decays of B mesons.* Phys. Rev. D 76 (2007). arXiv: 0704.1049 [hep-ph].

[98] I. Bediaga et al. *On a CP anisotropy measurement in the Dalitz plot.* Phys. Rev. D 80 (2009). arXiv: 0905.4233 [hep-ph].

[99] J. H. Alvarenga Nogueira et al. *CP violation: Dalitz interference, CPT, and final state interactions.* Phys. Rev. D 92.5 (2015). arXiv: 1506.08332 [hep-ph].

[100] H.-Y. Cheng, C.-K. Chua, and Z.-Q. Zhang. *Direct CP Violation in Charmless Three-body Decays of B Mesons.* Phys. Rev. D 94.9 (2016). arXiv: 1607.08313 [hep-ph].

[101] B. Bhattacharya, M. Gronau, and J. L. Rosner. *CP asymmetries in three-body $B^{\pm}$ decays to charged pions and kaons.* Phys. Lett. B 726 (2013). arXiv: 1306.2625 [hep-ph].

[102] D. Boito et al. *Parametrizations of three-body hadronic B- and D-decay amplitudes in terms of analytic and unitary meson-meson form factors.* Phys. Rev. D 96.11 (2017). arXiv: 1709.09739 [hep-ph].

[103] I. Bediaga, T. Frederico, and P. C. Magalhães. *Charm Penguin in $B^{\pm} \to K^{\pm}K^{+}K^{-}$: partonic and hadronic loops.* Phys. Lett. B 780 (2018). arXiv: 1712.01230 [hep-ph].

[104] I. Bediaga, T. Frederico, and P. C. Magalhaes. *CP asymmetry from hadronic charm rescattering in $B^{\pm} \to \pi^{-}\pi^{+}\pi^{\pm}$ decays at the high mass region.* Phys. Lett. B 806 (2020). arXiv: 2003.10019 [hep-ph].

[105] J. H. Blatt, V. F. Weisskopf, and A. C. Claus. *Theoretical Nuclear Physics.* Applied Optics (1952).

[106] S. U. Chung et al. *Partial wave analysis in K-matrix formalism.* Annalen der Physik 507.5 (1995).

[107] P. Gambino, M. Jung, and S. Schacht. *The V_{cb} puzzle: An update.* Phys. Lett. B 795 (2019). arXiv: 1905.08209 [hep-ph].

[108] M. Bordone, M. Jung, and D. van Dyk. *Theory determination of $\bar{B} \to D^{(*)}\ell^{-}\bar{\nu}$ form factors at $\mathcal{O}(1/m_c^2)$.* Eur. Phys. J. C 80.2 (2020). arXiv: 1908.09398 [hep-ph].

[109] T. Huber et al. *Phenomenology of inclusive $\bar{B} \to X_s \ell^+ \ell^-$ for the Belle II era.* JHEP 10 (2020). arXiv: 2007.04191 [hep-ph].

[110] T. Huber et al. *Long distance effects in inclusive rare B decays and phenomenology of $\bar{B} \to X_d \ell^+ \ell^-$.* JHEP 10 (2019). arXiv: 1908.07507 [hep-ph].

[111] P. Gambino et al. *Challenges in semileptonic B decays.* Eur. Phys. J. C 80.10 (2020). arXiv: 2006.07287 [hep-ph].

[112] M. Bordone, B. Capdevila, and P. Gambino. *Three loop calculations and inclusive V_{cb}.* Phys. Lett. B 822 (2021). arXiv: 2107.00604 [hep-ph].

[113] A. Alberti et al. *Precision Determination of the Cabibbo-Kobayashi-Maskawa Element V_{cb}.* Phys. Rev. Lett. 114.6 (2015). arXiv: 1411.6560 [hep-ph].

[114] P. Gambino and C. Schwanda. *Inclusive semileptonic fits, heavy quark masses, and V_{cb}.* Phys. Rev. D 89.1 (2014). arXiv: 1307.4551 [hep-ph].

[115] M. Fael, K. Schönwald, and M. Steinhauser. *Third order corrections to the semileptonic $b \to c$ and the muon decays.* Phys. Rev. D 104.1 (2021). arXiv: 2011.13654 [hep-ph].

[116] A. Kobach and S. Pal. *Reparameterization Invariant Operator Basis for NRQED and HQET.* JHEP 11 (2019). arXiv: 1810.02356 [hep-ph].

[117] J. Heinonen and T. Mannel. *Improved Estimates for the Parameters of the Heavy Quark Expansion.* Nucl. Phys. B 889 (2014). arXiv: 1407.4384 [hep-ph].

[118] Y. Hayashi, Y. Sumino, and H. Takaura. *Determination of $|V_{cb}|$ using N^3LO perturbative corrections to $\Gamma(B \to X_c \ell \nu)$ and 1S masses* (2022). arXiv: 2202.01434 [hep-ph].

[119] A. Sirlin. *Current Algebra Formulation of Radiative Corrections in Gauge Theories and the Universality of the Weak Interactions.* Rev. Mod. Phys. 50 (1978). [Erratum: Rev.Mod.Phys. 50, 905 (1978)].

[120] M. Jezabek and J. Kühn. *QCD corrections to semileptonic decays of heavy quarks.* Nuclear Physics B 314.1 (1989).

[121] V. Aquila et al. *Perturbative corrections to semileptonic b decay distributions.* Nucl. Phys. B 719 (2005). arXiv: hep-ph/0503083.

[122] M. Trott. *Improving extractions of $|V_{cb}|$ and m_b from the hadronic invariant mass moments of semileptonic inclusive B decay.* Phys. Rev. D 70 (2004). arXiv: hep-ph/0402120.

[123] K. Melnikov. *$O(\alpha_s^2)$ corrections to semileptonic decay $b \to c\ell\bar{\nu}$*. Phys. Lett. B 666 (2008). arXiv: 0803.0951 [hep-ph].

[124] P. Gambino. *B semileptonic moments at NNLO*. JHEP 09 (2011). arXiv: 1107.3100 [hep-ph].

[125] T. Becher, H. Boos, and E. Lunghi. *Kinetic corrections to $B \to X_c\ell\bar{\nu}$ at one loop*. JHEP 12 (2007). arXiv: 0708.0855 [hep-ph].

[126] A. Alberti et al. *Kinetic operator effects in $\bar{B} \to X_c\ell\nu$ at $O(\alpha_s)$*. Nucl. Phys. B 870 (2013). arXiv: 1212.5082 [hep-ph].

[127] A. Alberti, P. Gambino, and S. Nandi. *Perturbative corrections to power suppressed effects in semileptonic B decays*. JHEP 01 (2014). arXiv: 1311.7381 [hep-ph].

[128] T. Mannel, D. Moreno, and A. A. Pivovarov. *NLO QCD Corrections to Inclusive $b \to c\ell\bar{\nu}$ Decay Spectra up to $1/m_Q^3$* (2021). arXiv: 2112.03875 [hep-ph].

[129] Y. Nir. *The Mass Ratio m_c/m_b in Semileptonic B Decays*. Phys. Lett. B 221 (1989).

[130] A. Pak and A. Czarnecki. *Mass effects in muon and semileptonic $b \to c$ decays*. Phys. Rev. Lett. 100 (2008). arXiv: 0803.0960 [hep-ph].

[131] A. Pak and A. Czarnecki. *Heavy-to-heavy quark decays at NNLO*. Phys. Rev. D 78 (2008). arXiv: 0808.3509 [hep-ph].

[132] M. Dowling, J. H. Piclum, and A. Czarnecki. *Semileptonic decays in the limit of a heavy daughter quark*. Phys. Rev. D 78 (2008). arXiv: 0810.0543 [hep-ph].

[133] M. Czakon, A. Czarnecki, and M. Dowling. *Three-loop corrections to the muon and heavy quark decay rates*. Phys. Rev. D 103 (2021). arXiv: 2104.05804 [hep-ph].

[134] T. Mannel, A. A. Pivovarov, and D. Rosenthal. *Inclusive semileptonic B decays from QCD with NLO accuracy for power suppressed terms*. Phys. Lett. B 741 (2015). arXiv: 1405.5072 [hep-ph].

[135] T. Mannel and A. A. Pivovarov. *QCD corrections to inclusive heavy hadron weak decays at $\Lambda_{\mathrm{QCD}}^3/m_Q^3$*. Phys. Rev. D 100.9 (2019). arXiv: 1907.09187 [hep-ph].

[136] S. Aoki et. al. [FLAG Collaboration]. *FLAG Review 2019: Flavour Lattice Averaging Group (FLAG)*. Eur. Phys. J. C 80.2 (2020). arXiv: 1902.08191 [hep-lat].

[137] K. G. Chetyrkin et al. *Charm and Bottom Quark Masses: An Update*. Phys. Rev. D 80 (2009). arXiv: 0907.2110 [hep-ph].

[138] K. G. Chetyrkin et al. *Addendum to "Charm and bottom quark masses: An update"* (2017). [Addendum: Phys.Rev.D 96, 116007 (2017)]. arXiv: 1710.04249 [hep-ph].

[139] P. Gambino and S. Hashimoto. *Inclusive Semileptonic Decays from Lattice QCD*. Phys. Rev. Lett. 125.3 (2020). arXiv: 2005.13730 [hep-lat].

[140] P. Gambino, A. Melis, and S. Simula. *Extraction of heavy-quark-expansion parameters from unquenched lattice data on pseudoscalar and vector heavy-light meson masses*. Phys. Rev. D 96.1 (2017). arXiv: 1704.06105 [hep-lat].

[141] K. G. Chetyrkin, J. H. Kuhn, and M. Steinhauser. *RunDec: A Mathematica package for running and decoupling of the strong coupling and quark masses*. Comput. Phys. Commun. 133 (2000). arXiv: hep-ph/0004189.

[142] F. Herren and M. Steinhauser. *Version 3 of RunDec and CRunDec*. Comput. Phys. Commun. 224 (2018). arXiv: 1703.03751 [hep-ph].

[143] L. Cao et. al. [Belle Collaboration]. *Measurements of Partial Branching Fractions of Inclusive $B \to X_u \ell^+ \nu_\ell$ Decays with Hadronic Tagging*. Phys. Rev. D 104.1 (2021). arXiv: 2102.00020 [hep-ex].

[144] J. P. Lees et. al. [BaBar Collaboration]. *Measurement of the inclusive electron spectrum from B meson decays and determination of $|V_{ub}|$*. Phys. Rev. D 95.7 (2017). arXiv: 1611.05624 [hep-ex].

[145] P. Urquijo et. al. [Belle Collaboration]. *Moments of the electron energy spectrum and partial branching fraction of $B \to X_c e \nu$ decays at Belle*. Phys. Rev. D 75 (2007). arXiv: hep-ex/0610012.

[146] B. Aubert et. al. [BaBar Collaboration]. *Measurement and interpretation of moments in inclusive semileptonic decays $\overline{B} \to X_c \ell \bar{\nu}_\ell$*. Phys. Rev. D 81 (2010). arXiv: 0908.0415 [hep-ex].

[147] A. H. Mahmood et. al. [CLEO Collaboration]. *Measurement of the B-meson inclusive semileptonic branching fraction and electron energy moments*. Phys. Rev. D 70 (2004). arXiv: hep-ex/0403053.

[148] J. P. Lees et. al. [BaBar Collaboration]. *Measurement of the inclusive electron spectrum from B meson decays and determination of $|V_{ub}|$*. Phys. Rev. D 95.7 (2017). arXiv: 1611.05624 [hep-ex].

[149] J. Dingfelder and T. Mannel. *Leptonic and semileptonic decays of B mesons.* Rev. Mod. Phys. 88 (2016).

[150] Y. S. Amhis et. al. [HFLAV Collaboration]. *Averages of b-hadron, c-hadron, and τ-lepton properties as of 2018.* Eur. Phys. J. C 81.3 (2021). arXiv: 1909.12524 [hep-ex].

[151] P. Gambino, K. J. Healey, and C. Mondino. *Neural network approach to $B \to X_u \ell \nu$.* Phys. Rev. D 94.1 (2016). arXiv: 1604.07598 [hep-ph].

[152] Z. Ligeti, I. W. Stewart and F. J. Tackmann [SIMBA Collaboration]. *Treating the b quark distribution function with reliable uncertainties.* Phys. Rev. D 78 (2008). arXiv: 0807.1926 [hep-ph].

[153] F. U. Bernlochner et. al. [SIMBA Collaboration]. *Precision Global Determination of the $B \to X_s \gamma$ Decay Rate.* Phys. Rev. Lett. 127.10 (2021). arXiv: 2007.04320 [hep-ph].

[154] P. Gambino et al. *Inclusive semileptonic B decays and the determination of $|V_{ub}|$.* JHEP 10 (2007). arXiv: 0707.2493 [hep-ph].

[155] J. R. Andersen and E. Gardi. *Inclusive spectra in charmless semileptonic B decays by dressed gluon exponentiation.* JHEP 01 (2006). arXiv: hep-ph/0509360.

[156] F. De Fazio and M. Neubert. *$B \to X_u \ell \bar{\nu}$ lepton decay distributions to order α_s.* JHEP 06 (1999). arXiv: hep-ph/9905351.

[157] C. N. Burrell, M. E. Luke, and A. R. Williamson. *Subleading shape function contributions to the hadronic invariant mass spectrum in $\bar{B} \to X_u \ell \bar{\nu}$ decay.* Phys. Rev. D 69 (2004). arXiv: hep-ph/0312366.

[158] M. Beneke et al. *Power corrections to $B \to X_u \ell \nu (X_s \gamma)$ decay spectra in the 'shape-function' region.* JHEP 06 (2005). arXiv: hep-ph/0411395.

[159] K. S. M. Lee and I. W. Stewart. *Factorization for power corrections to $B \to X_s \gamma$ and $B \to X_u \ell \bar{\nu}$.* Nucl. Phys. B 721 (2005). arXiv: hep-ph/0409045.

[160] B. Blok et al. *Differential distributions in semileptonic decays of the heavy flavors in QCD.* Phys. Rev. D 49 (1994). [Erratum: Phys.Rev.D 50, 3572 (1994)]. arXiv: hep-ph/9307247.

[161] F. Herzog et al. *The five-loop beta function of Yang-Mills theory with fermions.* JHEP 02 (2017). arXiv: 1701.01404 [hep-ph].

Danksagung

Allen voran bedanke ich mich herzlich bei meinem Doktorvater Herrn Prof. Dr. Thomas Mannel, ohne den diese Arbeit niemals zustande gekommen wäre. Er hatte stets ein offenes Ohr für alle physikalischen Fragen, die mich während meiner Promotion umtrieben und hat mir auch über die wissenschaftlichen Fragen hinaus jederzeit mit seinem Rat zur Seite gestanden. Für die Chance diese Doktorarbeit zu verfassen und die großartige Unterstützung, auch für meinen zukünftige Werdegang, bin ich ihm tief verbunden. Herrn Prof. Dr. Alexander Lenz danke ich für die Bereitschaft als zweiter Gutachter diese Arbeit zu bewerten.

Ein besonderer Dank gilt allen Kollaborateuren mit denen ich an den Projekten dieser Arbeit zusammen gearbeitet habe. Ganz besonders danke ich Prof. Dr. K. Keri Vos, die in mühevoller Kleinarbeit meine Ergebnisse überprüfte und, wo nötig, für den nötigen Antrieb in unseren Projekten sorgte. Ohne ihre Unterstützung wären viele Ergebnisse dieser Arbeit womöglich nicht zustande gekommen. Weiterhin danke ich Dr. Björn Lange für die vielen detailierten Erklärungen und die anregenden Diskussionen. Ich danke dem V_{cb} - Team, ganz besonders Prof. Dr. Florian Bernlochner, Dr. Matteo Fael und Maximilian Welsch für die erfolgreiche Zusammenarbeit.

Es war mir stets eine große Freude Teil der Arbeitsgruppe am TP1 in Siegen gewesen zu sein und ich werde die vielen Gespräche in der Mensa und beim Kaffee, ganz besonders aber auch die gemeinsamen Brettspielabende sehr vermissen. Ich möchte mich bei allen bedanken, die zu der besonderen Atmosphäre an diesem Institut beigetragen haben.

Zuletzt danke ich meiner Familie und meiner Freundin Conny für die ununterbrochene Unterstützung und die Geduld in den schweren Zeiten dieser Arbeit.